Project Acronym	CORMORAN
Document Title	D2.4 Statistical and Deterministic Abstraction of the Dynamic Channel Variations
Contractual Date of Delivery to ANR	M24 (31/12/2013)
Actual Date of Delivery	M27 (13/03/2014)
Editor	Raffaele D'Errico (CEA)
Authors	Oudomsack Pierre Pasquero, Raffaele D'Errico (CEA), Bernard Uguen, Stéphane Avrillon, Meriem Mhedhbi, Nicolas Amiot (UR1), Paul Ferrand, Arturo Mauricio, Claire Goursaud, Jean-Marie Gorce, Jimenez Guizar (INSA)
Participants	CEA, UR1, INSA
Related Task(s)	T2
Related Sub-Task(s)	ST2.2, ST2.3, ST2.4
Security	Public
Nature	Technical Report
Version Number	1.1
Total Number of Pages	112

CONTACTS & CORRESPONDENCE

Raffaele D'Errico (CEA)
- Address: CEA-Leti Minatec, 17 rue des Martyrs, Bât. 51D, p. D423, 38054 GRENOBLE, cedex 9, France
- Email: raffaele.derrico@cea.fr
- Tel: (+33) (0)4 38 78 56 47

Bernard Uguen (UR1)
- Adresss : Campus de Beaulieu Bat 11D 35043 Rennes Cédex
- Email : bernard.uguen@univ-rennes1.fr
- Tel (+33) (0)2 23 23 60 33

TABLE OF CONTENT

ABSTRACT

This document presents the results of channel modeling activities carried out in the scope of task T2 of the CORMORAN project.

Preliminary antenna/channel measurements and models have been presented in previous deliverables of CORMORAN and not fully reported here for the sake of briefness. Reminds of the main results and detailed references are given to the reader.

The aim of this deliverable is to extend the statistical models focusing on the space-time correlation properties and the angular characteristics of the channel. These results are then employed for the assessment of deterministic ray-tracing tools capabilities to reproduce the main channel features in Wireless Body Area Networks. These two complementary approaches will be further exploited for the Physical simulator of CORMORAN.

1. INTRODUCTION

A good understanding of channel characteristics is of fundamental importance in order to design operative and reliable communication systems. Physical (PHY), Medium Access Control (MAC) and Upper Layers protocols are strictly connected to the knowledge of propagation mechanisms and channel models.

One of the tasks of the CORMORAN project is the modeling of Wireless Body Area Networks (WBAN) channels in order to provide a physical simulator for the design of communication and localization systems.

The channel models classification can be organized according to the antennas location around the body:

- *On-Body channel:* in this case both end points of the communication link are placed on the human subject. The propagation takes place along or around the body by diffraction (creeping waves), by Line-of-Sight (LOS) path in specific scenarios such as a link between the waist and the wrist, and hybrid mechanisms (e.g. diffraction off of arms). The shadowing effect of the body could affect significantly the system performance.

- *Body-to-Body* or *Off-Body channel:* we refer to *body-to-body* channels when the communication takes place between at least two human subjects, wearing different BAN, free to move relatively to each other in the environment, whereas *off-body* channels occur when one of the end point of the communication link is represented by an external fixed device e.g. a gateway or a router. In these cases a free-space propagation component has also to be considered.

In WBAN the channel is strongly dependent on antenna characteristics on the body. The partners of CORMORAN project have characterized and modeled the antenna-body interaction in the deliverable D2.1 [1]. An extensive State-of-the-Art of WBAN channel models, including those previously developed by CORMORAN partners has been presented in D2.2 [2].

In the scope of CORMORAN specific channel measurements have been carried out [3], aiming at modeling the correlation between different WBAN links, and investigating angular characteristics of the channel, which are needed for validating deterministic channel tools to be further exploited in the Physical simulator of the project.

This deliverable presents the results of channel modeling activities in CORMORAN in the scope of T2. The deliverable is organized as follows:
- Section 2 presents the results of correlation modeling in the on-body channel, starting from real time measurements at 2.4 GHz and 4.2 GHz ;

- Section 3 presents the results of Ultra Wideband (UWB) off-body channel modeling including the angular characteristics of the channel in presence of the body;
- Section 4 compares the results of statistical off-body channel modeling, with those obtained by means of the deterministic tool *Pylayers*, including antenna patterns on the body;
- Section 5 focuses on the Body-to-Body channel modeling and presents the results of correlation modeling where different WBAN links (on-body, off-body and body-to-body) are considered;
- Section 6 gives a view of a possible exploitation of channel models in the CORMORAN simulator, focusing in particular on UWB architectures;
- Finally conclusions on channel modeling activities in CORMORAN are given.

2. ON-BODY CHANNEL MODELS

2.1. REMIND OF ON-BODY STATISTICAL CHANNEL MODELS

In the deliverable D2.2 [2] channel models are presented for different communication and mobility scenarios which are exploitable for the design of WBAN systems and the evaluation of their performances. These models mainly describe the mean channel gain, the shadowing effects and the fast fading characteristics in function of the nodes positions on the body, the body orientation and location [4][5], and the antenna characteristics for narrow band signals around 2.45GHz [6]. Space-time correlation properties between different radio links for on-body communication scenarios are also described [4]. Values of the means channel gains and their variances obtained from previous measurements campaigns are summarized for different mobility scenarios in §2.3 of [2]. In addition a UWB channel model describing the channel impulse response characteristics such as the delay dispersion is also presented for on-body communication scenarios [7].

The full model of §4.1.3 in [2] are not reported here for the sake of briefness. An extension of these channel models starting from new measurements performed in the framework of CORMORAN [3] are here presented, focusing on the space-time correlation analysis.

2.2. SPACE-TIME CORRELATION ANALYSIS

In this sub-section, we analyze On-Body measurements in walking scenarios in order to characterize space-time correlation properties and to propose a model. Two measurement campaigns are exploited. The first one corresponds to previous CEA measurements already presented and analyzed in D2.3 [3]. The second one corresponds to measurements provided by UCL in the context of COST IC1004 [4]. For both measurement campaigns, we focus on the signal measured at 4.2 GHz, which is the center frequency of the UWB lower band.

2.2.1 CHANNEL MEASUREMENT CAMPAIGNS

- *CEA measurements*

The CEA measurement test bed was mainly composed by a pulse step generator and a power amplifier at the Tx side, whereas low-noise amplifiers were connected to a wideband real-time digital oscilloscope at the Rxs side, in a sort of SIMO configuration, as illustrated in Figure 1. The idea was to collect simultaneously up to four channel impulse responses (CIRs), each one corresponding to a different on-body location. RF cables and antennas were obviously part of the test-bed.
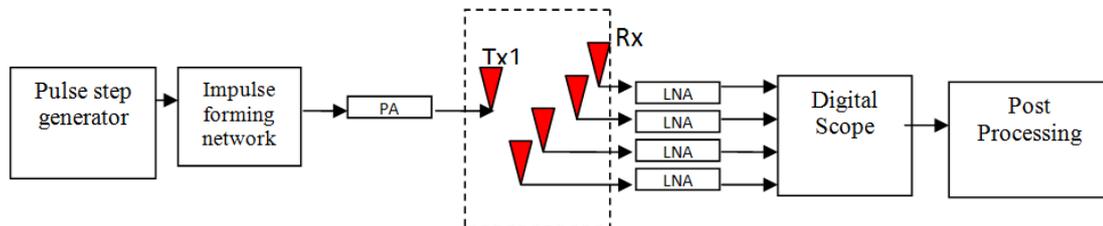
Figure 1 : Time domain channel measurement test-bed

The nodes emplacement considered for the measurement campaign performed is presented in Figure 2. Three human subjects have been involved in this measurement campaign for different mobility scenarios. Here, we will focus in the walking scenarios only. Each subject walked in a regular way on a straight line of 3 meters in one direction then the opposite one. Finally, two walk cycles and so, two measurement acquisitions of 3 s have been performed by subject.
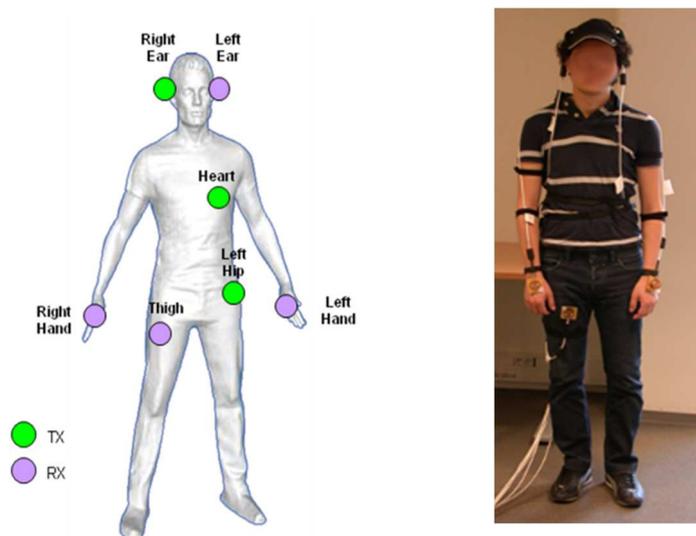
Figure 2 : Node emplacement for CEA On-Body measurements

- *UCL measurements*

The UCL measurement campaign was performed by means of a channel sounder, the WBAN consisting of 12 nodes located over the whole body as shown in Figure 3. The measurements were taken successively on two male subjects (subject 4: 1.87 m ; 85 kg and subject 5: 1.83 m ; 78 kg) in a quasi-empty room of approximately 5 by 10 m. In these conditions, the main reflections were from the walls, as well as from the channel sounder used for the measurements (3 metallic boxes of size 1 x 0.5 x 0.5 m). During the measurements, each subject walked freely around the room without any predefined path. The nodes were terminated by SMT-3TO10M-A SkyCross antennas, which are characterized by a return loss of around -10 dB in the considered bandwidth and an omni-

directional radiation pattern in the azimuth plane. Two polarizations were measured, respectively vertically and normally to the body (see in Figure 4).

A MIMO 8 x 8 Elektrobit channel sounder, whose transmit and receive units shared a common clock to avoid phase drifts, was used to measure the wireless channel. The measurements were performed with 1 (or 2) node(s) transmitting and 7 (or 6) nodes receiving simultaneously, the positions of the transmitting and receiving nodes being changed between measurements to get a statistical characterization of almost all of the 12 x 12 channels. The parameters of the sounder are given in Table 1. Each node was connected to the channel sounder with a 6 m SMA cable. A pre-measurement calibration showed that the cables did not influence the channel measurements. Note that the center frequency of 4.2 GHz is due to the channel sounder center frequency. The channel burst sample rate is about 20 Hz. Each burst consists of 4 successive measurements that are averaged to increase the measurement SNR. Finally, the sample period was equal to 23.6 ms. For each measurement run, 3000 channel measurements were recorded (representing almost 18 s for each dataset). More details can be found in [8].
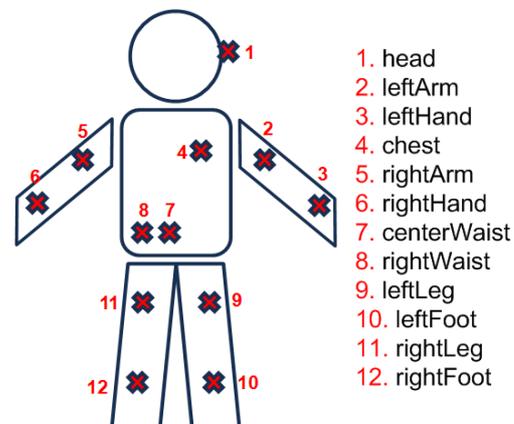
Figure 3 : UCL nodes emplacement on the body [4].

1. head
2. leftArm
3. leftHand
4. chest
5. rightArm
6. rightHand
7. centerWaist
8. rightWaist
9. leftLeg
10. leftFoot
11. rightLeg
12. rightFoot
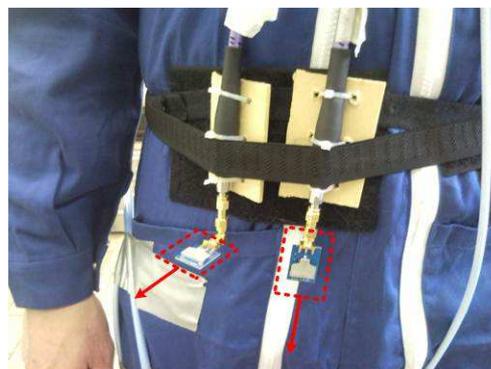
Figure 4 : Normally (left) and vertically (right) polarized antennas [4].

Parameter	1. Value
2. Center frequency	4.2 GHz
Bandwidth	100 MHz
Transmit power	6 dBm
Channel sample rate	169.708 Hz
Channel samples/burst	4
Burst rate	20 Hz

Table 1 : Channel sounder parameters [4].

2.2.2 MEASUREMENT ANALYSIS

According to the application scenarios and needs defined in D1.1, four pairs of On-Body links have been chosen for space-time correlation analysis. The On-Body sensor locations so-chosen are mostly well suited to LSIMC applications. They are summarized in Table 2.

	3. Tx location	4. 1st Rx location	5. 2nd Rx location
6. Scenario 1	Heart	Left Hand	Right Hand
Scenario 2	Right Hip	Left Hand	Right Hand
Scenario 3	Hip center	Left Foot	Right Foot
Scenario 4	Left Ear	Left Hand	Right Hand

Table 2 : Selected On-Body nodes location

In D2.2 and in [4], some space-time correlation properties between the extracted slow fading components of different On-Body links had been characterized at 2.45 GHz in walking scenarios. Here, we verify if these correlation properties still valid at 4.2 GHz, the center frequency of the UWB lower band. As performed in D2.2, the slow fading component of the measured signals is extracted by applying a low pass filter. The filtering is practically realized by averaging the time-dependent power transfer function on a sliding time window which duration Δt is equal to 320 ms for the CEA measurements and 330.40 ms for the UCL ones. The window widths difference is due to the different sample period used for each measurement campaign. The low pass filtering process is mathematically described by the following equation:

$$S(t) = \frac{1}{\Delta t} \int_{t-\Delta t/2}^{t+\Delta t/2} \frac{P(t)}{G_0}$$

(1)

where G_0 represents the mean channel gain, $P(t)$ the power transfer function and $S(t)$ the extracted slow fading component. The evaluation of $S(t)$ allows the description of the large-term variation of the power transfer function, and is here performed at 4.2 GHz. The following considerations on

shadowing correlation can be extended to the whole UWB band. The evolution of Power Delay Profile in on-body channels is addressed in [7].
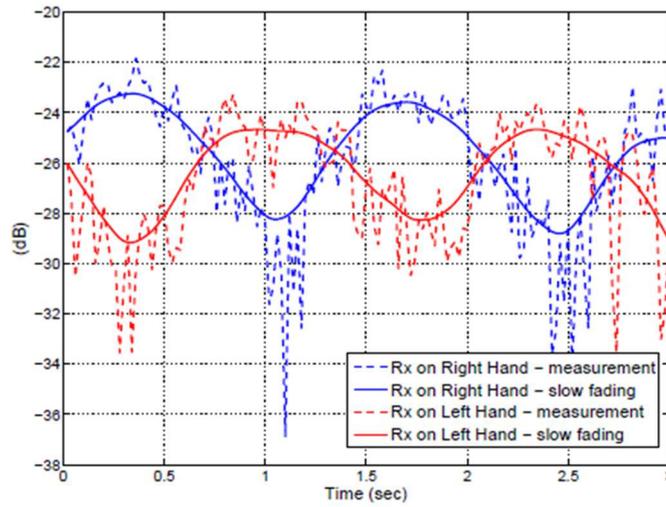
Figure 5 : CEA – scenario 1 (Tx on Heart) – subject 1 – slow fading components - Δt = 320 ms

Figure 5 shows slow fading curves obtained by performing this operation. Hence, we define the correlation metric as:

$$
\rho_{i,j}\left(t\,;T_{\mathrm{obs}}\right)= \frac{\mathbb{E}\left[\left(S_{\mathrm{TX},i}-\mathbb{E}\left[S_{\mathrm{TX},i}\right]\right)\left(S_{\mathrm{TX},j}-\mathbb{E}\left[S_{\mathrm{TX},j}\right]\right)\right]}{\sqrt{\mathbb{E}\left[S_{\mathrm{TX},i}^{2}-\mathbb{E}^{2}\left[S_{\mathrm{TX},i}\right]\right]\mathbb{E}\left[S_{\mathrm{TX},j}^{2}-\mathbb{E}^{2}\left[S_{\mathrm{TX},j}\right]\right]}}
$$

(2)

where E[.] represents the expectation operator and $S_{\mathrm{TX},i}$ the slow fading component in dB of the radio link associated to the TX transmitting antenna position and the i-th receiving antenna position measured during the interval time [$t - T_{\mathrm{obs}}/2$; $t + T_{\mathrm{obs}}/2$]. Finally, $\rho_{i,j}$ represents the correlation value measured between two radio links on a time window which width is equal to T_{obs}.
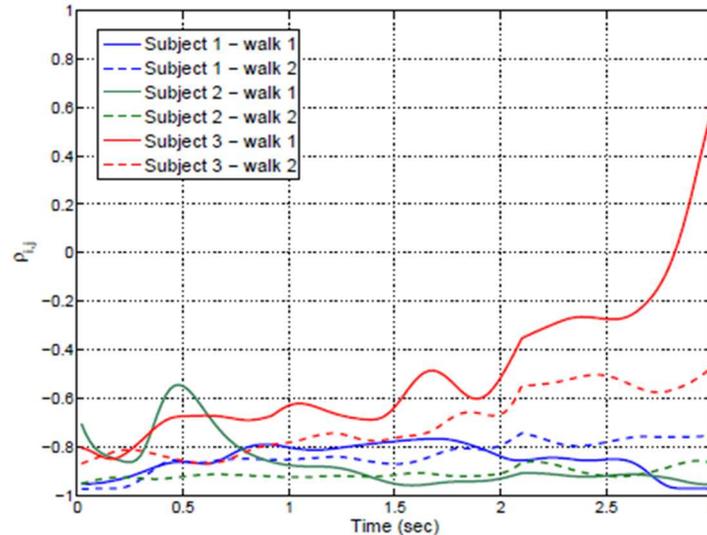
Figure 6 : CEA - scenario 1 - $\rho_{i,j}$ measured for the three human subjects for both walk cycles - T_{obs} = 1.8 s

In D2.3, we analyzed the CEA measurements corresponding to scenario 1. Figure 6 gives the space-time correlation values computed. We concluded that due to the body symmetry and the swing of the arms in walking scenarios, the radio links corresponding to scenario 1 were highly anti-correlated. This conclusion is identical to that made at a frequency equal to 2.45 GHz in D2.2 and in[4]. For subject 3, the increase of the correlation value during the last second was explained by the fact that the subject prematurely finished his walk.

Since the edition of D2.3, we analyzed UCL measurements for the same scenario. Let us note that for the correlation values computation, the observation time window width T_{obs} used has been optimized. Thus, we set T_{obs} equal to 1.8 s.
Surprisingly, the results obtained are different to those observed with the CEA measurements. As we can see in Figure 7, the computed correlation value strongly varies in time. In other words, contrary to CEA measurements, the correlation properties are not stationary in time. It is confirmed by comparing the slow fading curves in Figure 8. This characteristic can be explained by the fact that the UCL subjects walked randomly. In the CEA measurement campaign, the human subjects walked like a soldier on a straight line, causing a regular swing of their arms. This can explain why the correlation properties are not the same between CEA and UCL measurements. In conclusion, the way the subject walks has a strong impact on the space-time correlation properties.
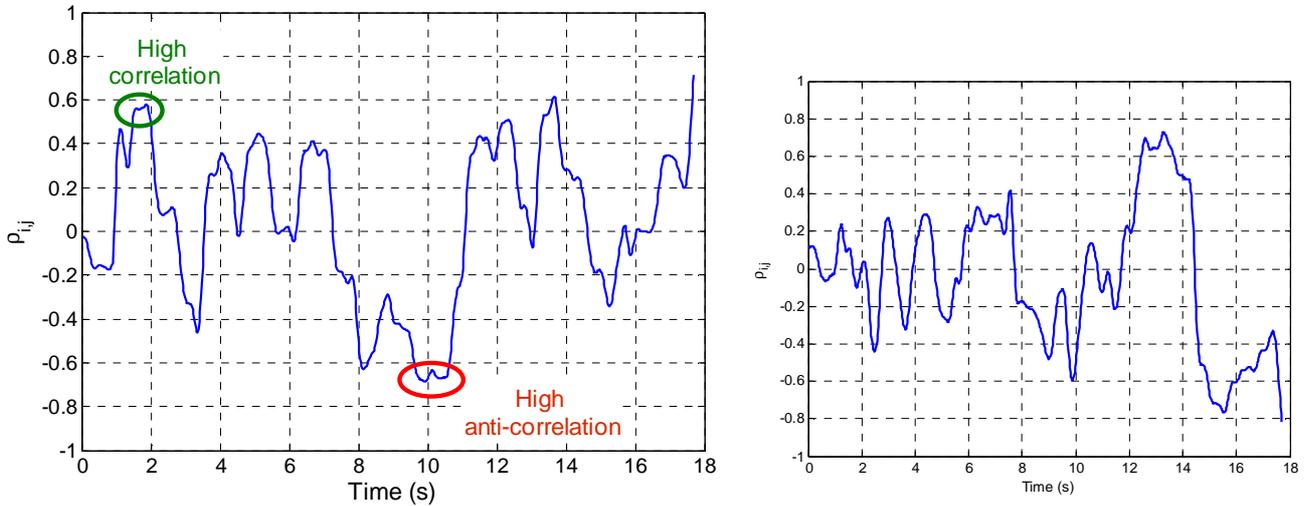
Figure 7 : UCL – scenario 1 - $\rho_{i,j}$ measured for subject 1 (left) and subject 2 (right) - T_{obs} = 1.8s
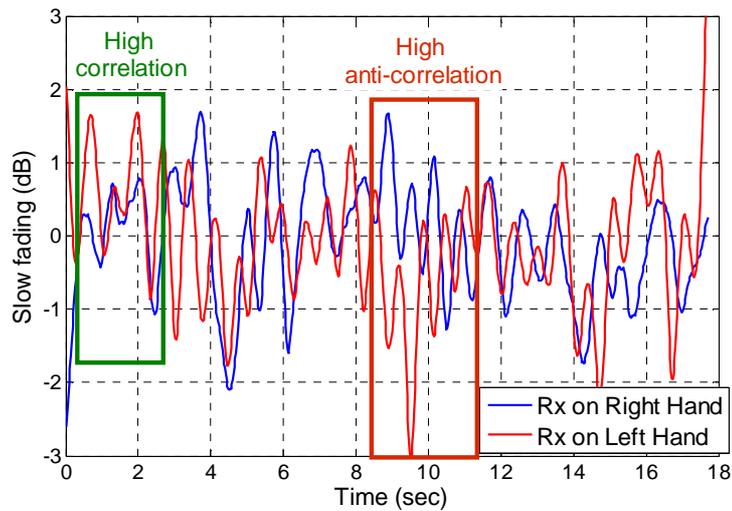
Figure 8 : UCL - scenario 1 - subject 1 - slow fading components

We give in Figure 9, Figure 10 and Figure 11, the correlation values measured for the other scenarios. The same conclusion than that made for scenario 1 can be carried out whatever are the nodes locations: the space-time correlation properties are not stationary in time. The final objective of this section is to model statistically the time variation of the space-time correlation for the four scenarios.
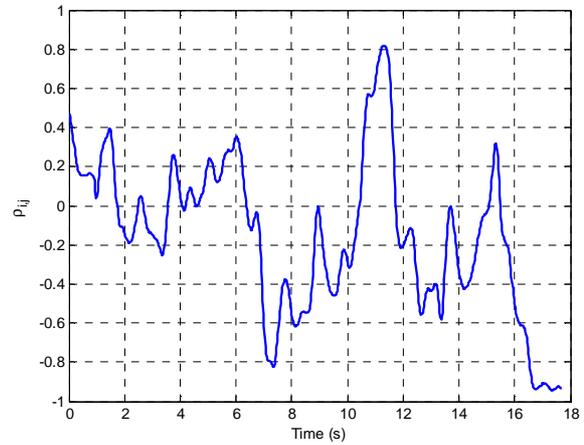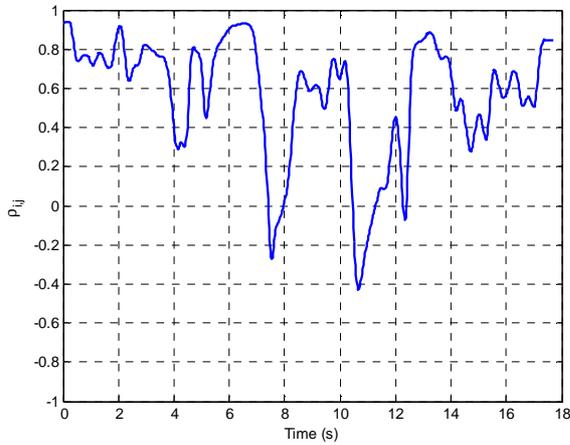
Figure 9 : UCL - scenario 2 - $\rho_{i,j}$ measured for subject 1 (left) and subject 2 (right) - T_{obs} = 1.8 s
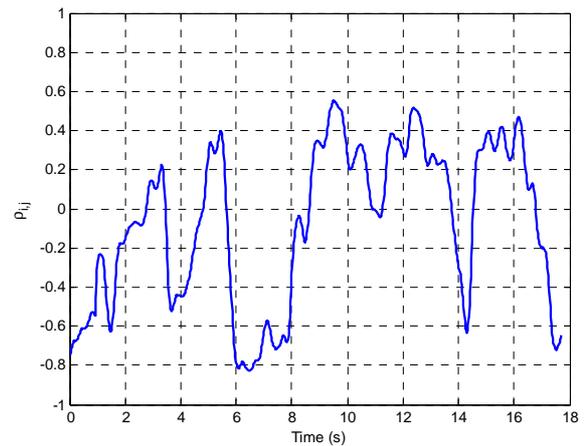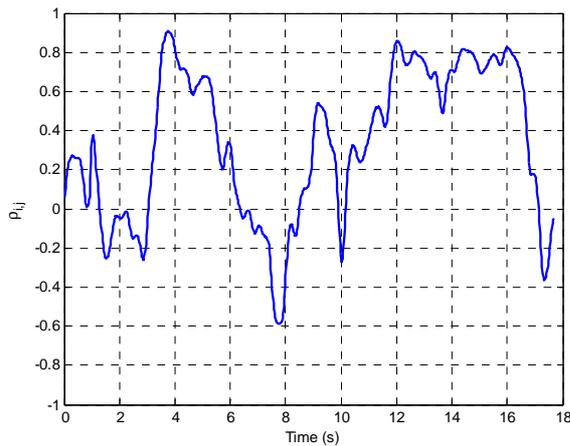
Figure 10 : UCL - scenario 3 - $\rho_{i,j}$ measured for subject 1 (left) and subject 2 (right) - T_{obs} = 1.8 s
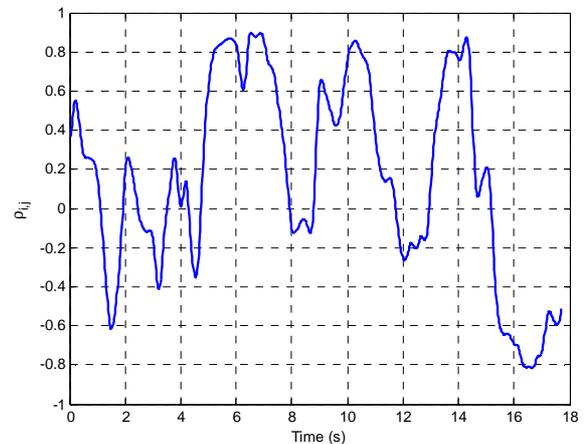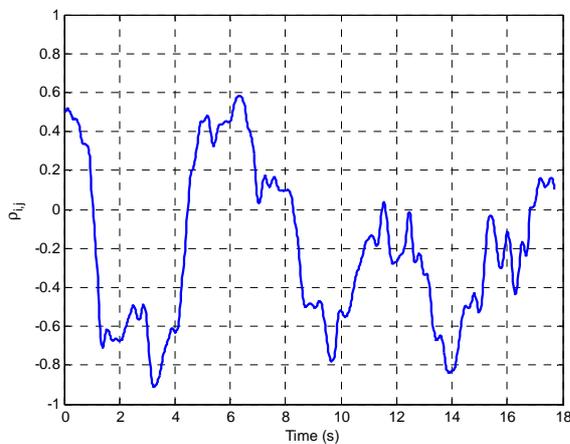
Figure 11 : UCL - scenario 4 - $\rho_{i,j}$ measured for subject 1 (left) and subject 2 (right) - T_{obs} = 1.8 s

To complete this set of measurements, channel acquisitions were performed at INSA and reported in [3] and [31] , focused on two cases: the link symmetry and the shadowing correlation under walking scenarios [9] and using industrial sensors with a physical layer IEEE 802.15.4 compliant in the 2.4GHz ISM band [10]. The first experiment showed strong periodical variations in the link qualities that may be generated by the body movements and the sensor hardware. However, the impact of the passages on the symmetry of the links is negligible compared the sensor hardware and the link influences.

In a second study case, locations with a low amount of interference both indoor and outdoor were considered. The outdoor scenario was conducted on the same running track as the link symmetry study, and the indoor scenario was conducted in a corridor located in a basement, which is interference-free and narrow, thus highly prone to multipath reflections. The application of a Butterworth low-pass filter on the frequency analysis of the links allowed extracting the shadowing effect caused by the body motion, on the outdoor scenario, for which this effect is dominant in the low frequencies. For the indoor scenario, as the links are more prone to multipath fading, the shadowing effect does not clearly appear and thus cannot be extracted reliably. Using statistical tests on correlation matrices from [11] and [12], INSA results showed that the mean correlation matrix for repeated passages in the same environment differs greatly from the instantaneous correlation matrices.

As a consequence repetitive and regular movements imply that correlation matrices do not vary significantly over time, opening up the possibility for realistic protocols with relaying strategies, that are being addressed in T3. On the other hand random and/or not consecutive movements could yield to a variation of the correlation along time, which is modeled in the following section.

2.3. PROPOSED MODEL

To model the space-time correlation properties, we propose to use a Markov chain in which we define 5 correlation states:

- very anti-correlated (VA): $\rho_{i,j} < -0.5$
- anti-correlated (A): $-0.5 < \rho_{i,j} < -0.3$
- decorrelated (D): $-0.3 < \rho_{i,j} < 0.3$
- correlated (C): $0.3 < \rho_{i,j} < 0.5$
- very correlated (VC): $0.5 < \rho_{i,j}$

And we propose to affect the following correlation values for each correlation state:

- VA: $\rho_{i,j} = -0.6$
- A: $\rho_{i,j} = -0.4$
- D: $\rho_{i,j} = 0$
- C: $\rho_{i,j} = 0.4$
- VC: $\rho_{i,j} = 0.6$

PROGRAMME
INFRASTRUCTURES MATERIELLES
ET LOGICIELLES POUR LA SOCIETE
NUMERIQUE – ED. 2011

ANR

CORMORAN
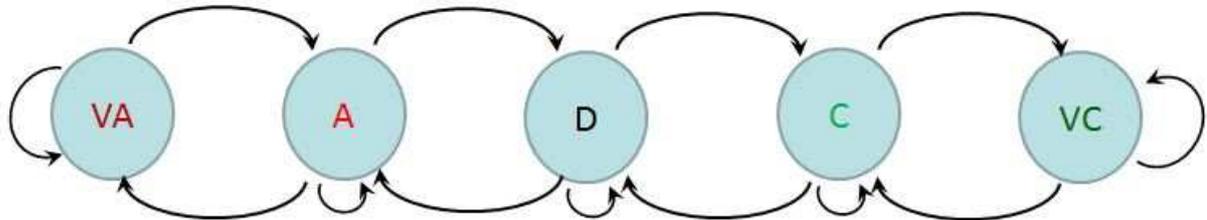
Figure 12 : Principle of the proposed On-Body channel space-time correlation modeling

From the UCL correlation values measured at each time sample, we compute the probabilities to stay in each state and those to move from a state to another one. Let us remind that, for the UCL measurements, the sampling period Δt is equal to 23.6 ms. We intuitively understand that these probabilities are strongly dependent to the sampling period. Indeed, the greater the sampling period Δt, the higher the probability the correlation state changes. And on the contrary, the smaller the sampling period, the higher the probability the correlation state does not change. In our case, we remarked that the sampling period was small enough to not allow any brutal correlation value variation. In other words, between two consecutive time samples, there is not any transition from a correlation state to another one which is very different. For instance, there is not any direct transition from the state VA to the state D.

	7. Subject 1	8. Subject 2	9. Average
10. P(VA -> VA)	0.97	0.98	0.975
P(VA -> A)	0.03	0.02	0.025
P(A -> VA)	0.03	0.03	0.03
P(A -> A)	0.92	0.92	0.92
P(A -> D)	0.05	0.05	0.05
P(D ->A)	0.01	0.01	0.01
P(D -> D)	0.97	0.98	0.975
P(D -> C)	0.02	0.01	0.015
P(C -> D)	0.05	0.07	0.06
P(C -> C)	0.93	0.91	0.92
P(C -> VC)	0.02	0.02	0.02
P(VC -> C)	0.06	0.02	0.04
P(VC -> VC)	0.94	0.98	0.96

Table 3 : UCL – scenario 1 – Probabilities of the transitions between the correlation states

	11. Subject 1	12. Subject 2	13. Average
14. P(VA -> VA)		0.97	0.97
P(VA -> A)		0.03	0.03
P(A -> VA)	0.00	0.05	0.025
P(A -> A)	0.92	0.91	0.915

P(A -> D)	0.08	0.05	0.065
P(D ->A)	0.01	0.01	0.01
P(D -> D)	0.95	0.98	0.965
P(D -> C)	0.04	0.01	0.025
P(C -> D)	0.05	0.12	0.085
P(C -> C)	0.88	0.86	0.87
P(C -> VC)	0.07	0.02	0.045
P(VC -> C)	0.01	0.03	0.02
P(VC -> VC)	0.99	0.97	0.98

Table 4 : UCL – scenario 2 – Probabilities of the transitions between the correlation states

	15. Subject 1	16. Subject 2	17. Average
18. P(VA -> VA)	0.94	0.97	0.955
P(VA -> A)	0.06	0.03	0.045
P(A -> VA)	0.06	0.08	0.07
P(A -> A)	0.81	0.84	0.825
P(A -> D)	0.13	0.08	0.105
P(D ->A)	0.01	0.01	0.01
P(D -> D)	0.97	0.96	0.965
P(D -> C)	0.02	0.03	0.025
P(C -> D)	0.07	0.06	0.065
P(C -> C)	0.86	0.92	0.89
P(C -> VC)	0.06	0.01	0.035
P(VC -> C)	0.02	0.08	0.05
P(VC -> VC)	0.98	0.92	0.95

Table 5 : UCL – scenario 3 – Probabilities of the transitions between the correlation states

	19. Subject 1	20. Subject 2	21. Average
22. P(VA -> VA)	0.96	0.99	0.975
P(VA -> A)	0.04	0.01	0.025
P(A -> VA)	0.09	0.06	0.075
P(A -> A)	0.86	0.84	0.85
P(A -> D)	0.05	0.10	0.075
P(D ->A)	0.02	0.01	0.015
P(D -> D)	0.98	0.98	0.98
P(D -> C)	0.003	0.01	0.0065
P(C -> D)	0.02	0.07	0.045
P(C -> C)	0.96	0.85	0.895
P(C -> VC)	0.02	0.08	0.05

P(VC -> C)	0.07	0.02	0.045
P(VC -> VC)	0.93	0.98	0.955

Table 6 : UCL – scenario 4 – Probabilities of the transitions between the correlation states

We give in Table 3, Table 4, Table 5 and Table 6, the probabilities of the transitions between the correlation states corresponding to scenario 1, scenario 2, scenario 3 and scenario 4 respectively. It appears that the probability values are very similar between the two subjects. We propose to use the average values for the model.

Nevertheless, there is no information about the initial correlation state, which is necessary for the model implementation. For that purpose, by exploiting all the correlation values computed over all the measurement duration, we propose to simply compute the probability to be in each correlation state for each subject. These probabilities are given in **Table 7**. Contrary to the probabilities of the transitions between the correlation states, the probability values of the channel to be in each correlation state are not always similar between the two subjects. This can be explained by a different way of walking between the different subjects. Thus, we propose the model alternates between these two sets of probabilities to determine the initial correlation state.

	23. Subject 1	**24. Subject 2**
25. P(VA)	0.10	0.14
P(A)	0.10	0.12
P(D)	0.50	0.59
P(C)	0.24	0.06
P(VC)	0.07	0.09

Table 7 : UCL – scenario 1 – Probability of the channel to be in each correlation state

	26. Subject 1	**27. Subject 2**
28. P(VA)	0.00	0.19
P(A)	0.02	0.15
P(D)	0.15	0.55
P(C)	0.13	0.06
P(VC)	0.70	0.05

Table 8 : UCL – scenario 2 – Probability of the channel to be in each correlation state

	29. Subject 1	**30. Subject 2**
31. P(VA)	0.02	0.22
P(A)	0.02	0.09
P(D)	0.42	0.45
P(C)	0.11	0.21
P(VC)	0.42	0.03

Table 9 : UCL – scenario 3 – Probability of the channel to be in each correlation state

	32. Subject 1	33. Subject 2
34. P(VA)	0.31	0.15
P(A)	0.13	0.04
P(D)	0.40	0.42
P(C)	0.13	0.08
P(VC)	0.04	0.32

Table 10 : UCL – scenario 4 – Probability of the channel to be in each correlation state

Finally, by exploiting these tables, the proposed model gives an initial space-time correlation value for 4 pairs of On-Body links in walking scenarios. Then, the correlation values are updated every 23.6 ms using the probabilities of transition between the different correlation states.

3. OFF-BODY STATISTICAL CHANNEL MODELING

In this section, we first remind narrow band (NB) Off-Body channel models proposed in D2.2. Then, we analyze the UWB Off-Body measurements presented in D2.3. First of all, we briefly remind the scenarios of the channel measurement campaigns, described in details in D2.3. Let us remind that preliminary processing of these measurements had already been carried out using the *Space Alternating Generalized Expectation-maximization* (SAGE) algorithm developed. These processing had allowed observing influences of the body on the channel characteristics. Since the delivery of D2.3, a clustering algorithm has been developed. It allows processing the MPCs parameters estimated by SAGE algorithm. Thus, we analyze more in depth the UWB Off-Body channel characteristics and propose some models.

3.1. REMIND ON NB OFF-BODY STATISTICAL CHANNEL MODEL

Extensive channel measurement campaigns have been performed at CEA-LETI at 2.4 GHz. The results have been exploited to model the distance-dependent channel gain, muli-path fading and shadowing [16]. The results have been also exploited to extract the space-time correlation over walking movements [17]. The full models can be found in §4.1.2 of [2] and are not reported here for the sake of briefness.

3.2. REMIND OF THE UWB OFF-BODY MEASUREMENT CAMPAIGNS

3.2.1 SET-UP MEASUREMENTS

UWB Off-Body channel measurements had been performed at CEA-Leti for the delivery of D2.3. For that purpose, a CTIA/IEEE standardized phantom located on a (X, Y) positioner and a 4 ports VNA had been used. One antenna had been placed on a mast, thus representing the external access point (AP). And three antennas had been placed on the torso, the left shoulder and the back of the phantom. These on-body locations had been chosen according the application scenarios and needs presented in D1.1. More precisely, they represent the favorite on-body locations for the *Coordinated Group Navigation* (CGN) applications. Furthermore, in order to evaluate the body influences, benchmark measurements with an isolated antenna, i.e. without presence of the phantom, had also been performed. In this scenario, only one antenna had been used the Rx side. Its location was similar to that of the torso.
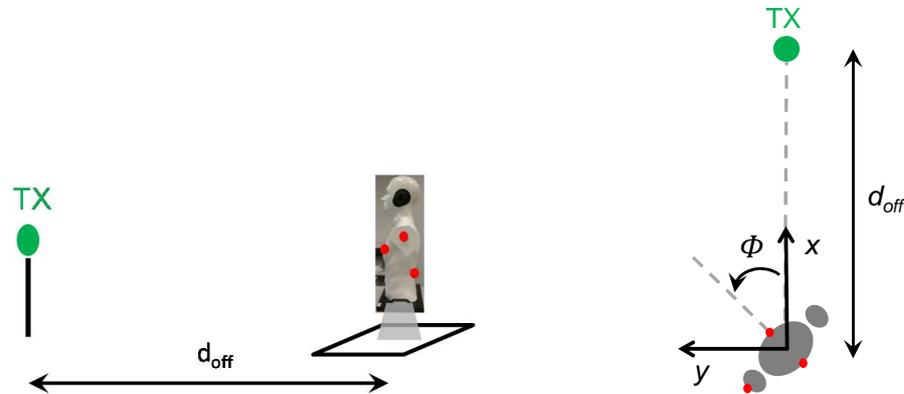
Figure 13 : Off-Body measurements illustration, side and top view

The measurements had been performed in two different rooms in the frequency range [3 – 10] GHz. The distance d_{off} separating the AP to the phantom varied from 1 to 8 m, with a step equal to 1 m. For each distance, measurements had been carried out for 5 phantom orientations Φ varying from 0° to 180°, with a step equal to 45°. Figure 13 illustrates the measurement campaigns.

3.2.2   ENVIRONMENT DESCRIPTION

We describe in this paragraph the geometry of the first environment where the measurements had been performed. We do not give that of the 2nd environment which is geometrically much more complicated to describe. This detailed description will allow to test the Off-Body deterministic channel model by setting an environment more similar to that where the measurements have been performed.
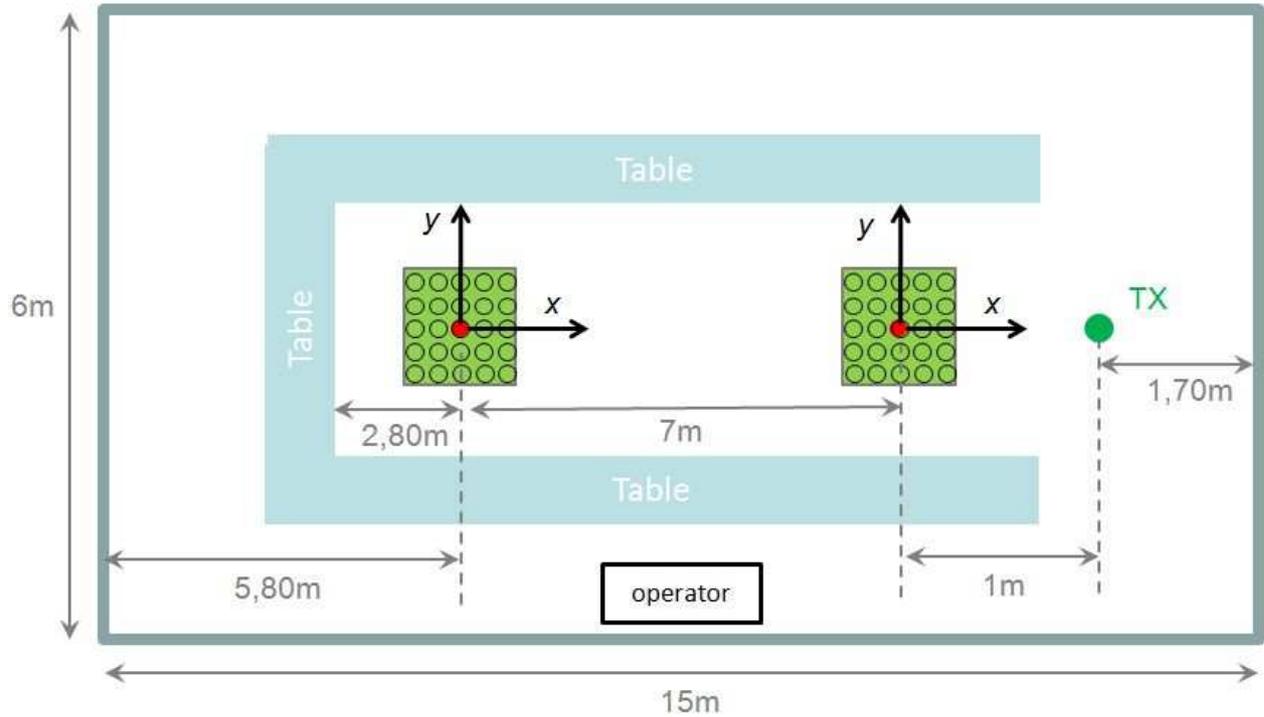
Figure 14 : Description of the 1st environment

The first environment has a rectangular shape as illustrated in Figure 14. The squares in green represent the virtual antenna array. Let us note its size is not in scale compared to that of the room. Some photographs are given in Figure 15. The distance between the floor and the plafond was 2.55 m on the left half side of the room, and 2.80 m on the right half side. The Tx height was 1.35 m. That of the Rx isolated antenna was 1.33 m. Those of the Rxs located on the torso, the shoulder and the back, were respectively 1.33 m, 1.40 m and 1.35 m. And the height of the phantom when placed on the positioner was 1.75 m.

Figure 15 : Photographs of environment 1

3.3. UWB PATH LOSS MODEL

From the measurements, we propose to model the path loss (PL) for UWB Off-Body radio links on the frequency band [3 – 10] GHz. Thus, we give in Figure 16, Figure 17 and Figure 18, the measured PL versus the distance for the two environments where the measurements have been performed, for the antenna located on the torso, the left shoulder and the back respectively. Each curve represents a body orientation. The black one represents the isolated antenna case.

Logically, the more the phantom hides the link between the Tx antenna and Rx one, i.e. the more the radio link is in NLOS condition, the more the PL absolute value. More precisely, the absolute PL value is the lowest when the phantom orientation Φ is equal to:
- 0° for Rx located on the torso
- 0° and/or 180° for Rx located on the left shoulder
- 180° for Rx located on the back.

And it is the highest when the phantom orientation Φ is equal to:
- 180° for Rx located on the torso
- 90° for Rx located on the left shoulder
- 0° for Rx located on the back.
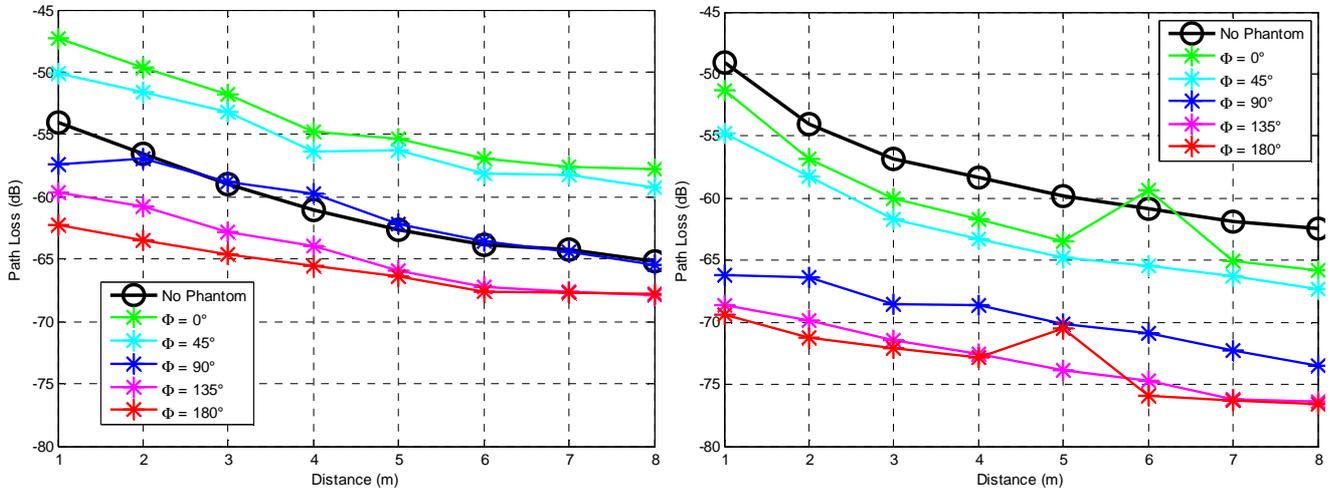
Figure 16 : Measured Path Loss versus distance – Rx on Torso, env 1 (left) and env 2 (right)
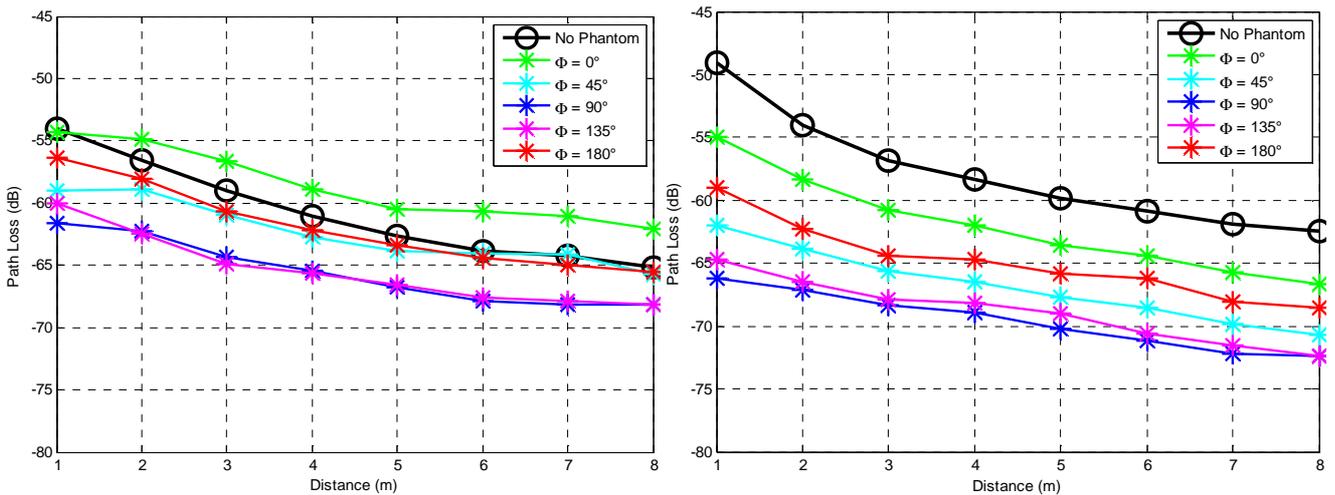
Figure 17 : Measured Path Loss versus distance – Rx on Shoulder, env 1 (left) and env 2 (right)
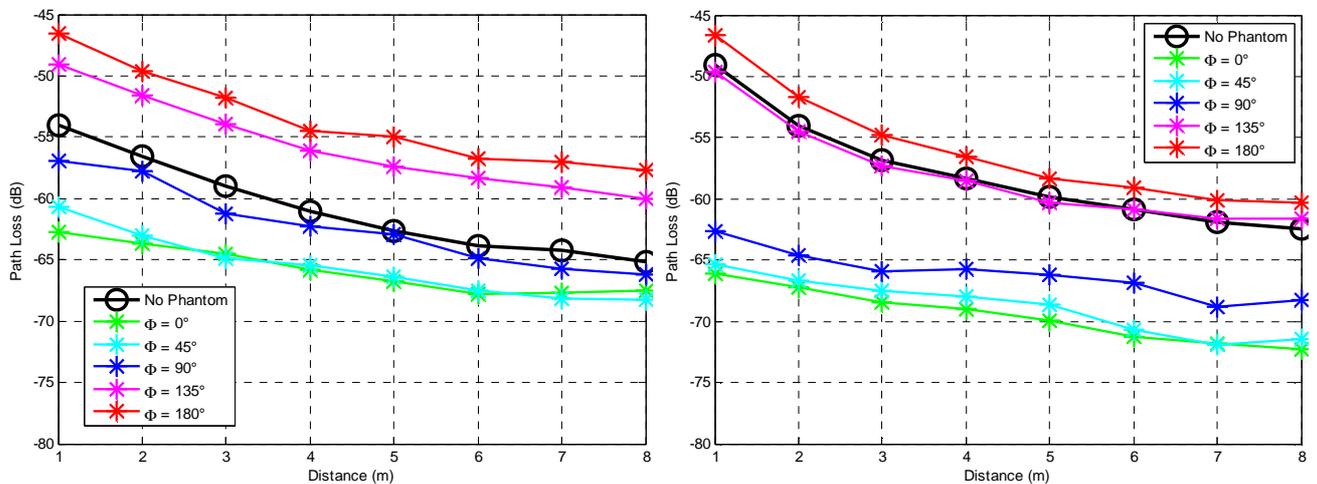
Figure 18 : Measured Path Loss versus distance – Rx on Back, env 1 (left) and env 2 (right)

In the literature, the PL is classically modeled by the following equation:

$$PL(d) = PL_0 + 10\, n_{\mathrm{d}}(\Phi)\, \log_{10}\left(\frac{d}{d_0}\right)$$

(3)

where d_0 represents the reference distance equal to 1 m, PL_0 the PL value at this reference distance, and $n_{\mathrm{d}}(\Phi)$ the distance decay coefficient. The latter evolves in function of the Rx location and the body orientation [13]. Thus, modeling the UWB Off-Body PL consists in estimating the values of the parameters PL_0 and $n_{\mathrm{d}}(\Phi)$ for all the scenarios. For that purpose, we apply a linear regression on all the PL curves. Thus, we obtain a distance decay coefficient $n_{\mathrm{d}}(\Phi)$ and a reference PL value PL_0 for all the Rx locations and all the body orientations Φ. The estimated distance decay values $n_{\mathrm{d}}(\Phi)$ are given for both environments in Figure 19, Figure 20 and Figure 21 for the Rx antenna located on the torso, the left shoulder and the back respectively. The isolated antenna case is also given as reference. Let us note that since in this case, the antenna is omnidirectional in azimuth, the distance decay coefficient does not vary with the orientation Φ.

The general trend of the curves shows that the more the phantom hides the link between the Tx antenna and the Rx one, the lower the absolute value of the distance decay coefficient. Or more precisely, the more the body orientation Φ is close to 180°, 90° or 0° for Rx antenna located on the torso, the left shoulder or the back respectively, the less the PL is function of the distance. On the contrary, the more the body orientation Φ is close to 0° for the torso case, to 0° or 180° for the shoulder case and to 180° for the back case, i.e. the more radio link is in LOS condition, the more the PL is function of the distance. These observations are identical to those made for narrow band channels centered at 2.45 GHz in [16]. Moreover, for a given environment, it appears that the distance decay coefficient value $n_{\mathrm{d}}(\Phi)$ is very similar between the torso case with Φ equal to 0°, the back case with Φ equal to 180° and the isolated antenna case. In conclusion, the more an Off-Body link is in LOS condition, the less the body have influences on the dependence of the PL to the distance.
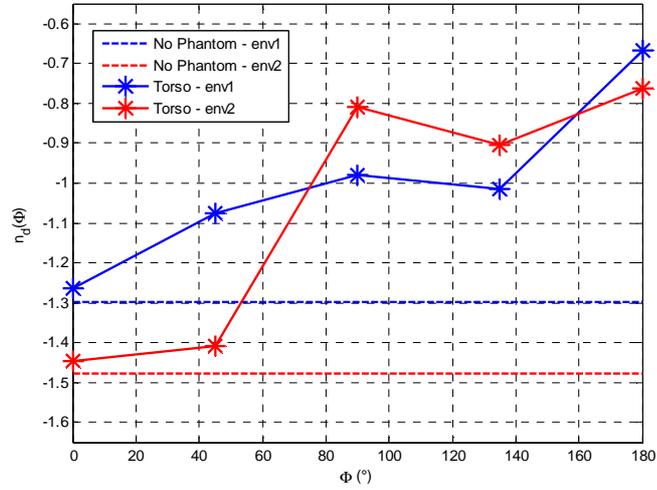
Figure 19 : Distance decay coefficient versus Body orientation – Rx on Torso
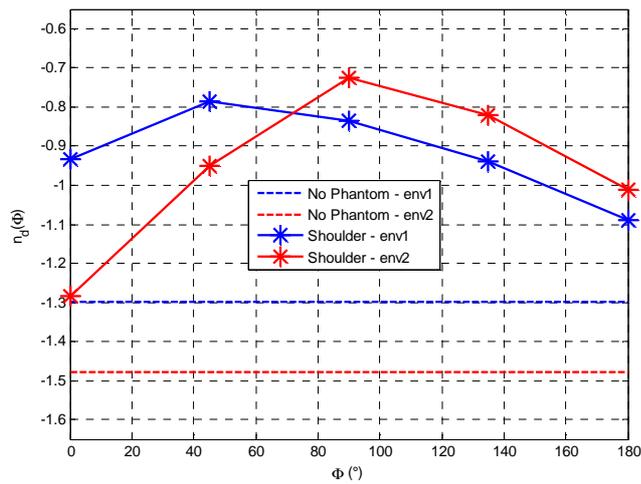
Figure 20 : Distance decay coefficient versus Body orientation – Rx on Shoulder
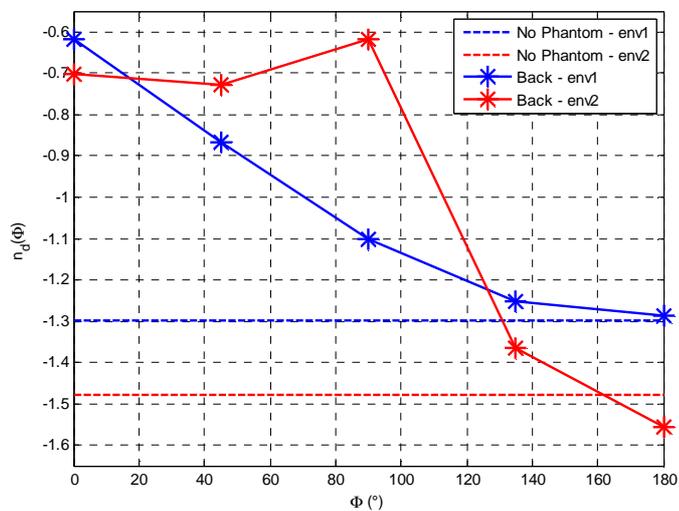
Figure 21 : Distance decay coefficient versus Body orientation – Rx on Back

We give in **Table 11** and **Table 12** the distance decay values for both environments. We also give the PL reference value in dB in **Table 13** and **Table 14**. These parameter values are useful for the UWB Off-Body PL model based on equation (3).

n	35. Isolated antenna	36. Torso	37. Left Shoulder	38. Back
Φ = 0°	-1.30	-1.26	-0.93	-0.62
Φ = 45°	-1.30	-1.08	-0.79	-0.87
Φ = 90°	-1.30	-0.98	-0.83	-1.10
Φ = 135°	-1.30	-1.02	-0.94	-1.25
Φ = 180°	-1.30	-0.67	-1.09	-1.29

Table 11 : Path loss exponent - environment 1

n	39. Isolated antenna	40. Torso	41. Left Shoulder	42. Back
Φ = 0°	-1.48	-1.45	-1.28	-0.70
Φ = 45°	-1.48	-1.41	-0.95	-0.73
Φ = 90°	-1.48	-0.81	-0.72	-0.62
Φ = 135°	-1.48	-0.90	-0.82	-1.37
Φ = 180°	-1.48	-0.76	-1.01	-1.56

Table 12: Path loss exponent - environment 2

PL_0	43. Isolated antenna	44. Torso	45. Left Shoulder	46. Back
Φ = 0°	-53.33 dB	-46.61 dB	-53.24 dB	-62.23 dB
Φ = 45°	-53.33 dB	-49.21 dB	-57.89 dB	-60.54 dB
Φ = 90°	-53.33 dB	-55.43 dB	-60.76 dB	-55.91 dB
Φ = 135°	-53.33 dB	-58.63 dB	-59.99 dB	-48.49 dB
Φ = 180°	-53.33 dB	-61.84 dB	-55.68 dB	-46.20 dB

Table 13 : Reference Path Loss (dB) for distance equal to 1 m - environment 1

PL_0	47. Isolated antenna	48. Torso	49. Left Shoulder	50. Back
Φ = 0°	-49.41 dB	-52.12 dB	-54.67 dB	-65.48 dB
Φ = 45°	-49.41 dB	-54.64 dB	-61.37 dB	-64.58 dB
Φ = 90°	-49.41 dB	-64.91 dB	-65.40 dB	-62.59 dB
Φ = 135°	-49.41 dB	-67.74 dB	-64.10 dB	-50.19 dB
Φ = 180°	-49.41 dB	-68.71 dB	-59.06 dB	-46.98 dB

Table 14 : Reference Path Loss (dB) for distance equal to 1 m - environment 2

3.4. MPC AND CLUSTER MODELING TOOLS

In this sub-section, we first briefly remind the principle of the implemented SAGE algorithm which has been exploited for the UWB Off-Body measurements process. More precisely, it has been used for the estimation of the number of MPCs, their complex amplitude, their delays and their angles-of-arrival (AoA). Let us remind that since a 2D positioner had been used for the measurements, the estimated AoA in elevation are not reliable. Therefore, we analyze the estimated AoA in the azimuth plan only. Since the delivery of D2.3, a clustering algorithm has been developed at CEA. It takes as inputs the SAGE estimates.

3.4.1   REMIND OF THE IMPLEMENTED SAGE ALGORITHM

- *Overview*

Based on the *Expectation Maximization* (EM) algorithm [19], SAGE algorithm has been proposed for the first time for channel parameters estimation by B. Fleury in [20]. In [21], Chong *et al.* proposed a frequency-domain version of SAGE for Single-Input Multiple-Output (SIMO) system, which has been extended by Matthaiou *et al*, to Multiple-Input Multiple-Output (MIMO) systems [22]. UWB and spherical wave features have been introduced by Haneda *et al.* in [23] and [24]. Finally, S. Van Roy *et al.* adapted the UWB SAGE algorithm for BAN scenarios in [25].

The SAGE algorithm allows the estimation of the parameters of the multipath components (MPCs). In our case, we will focus on the estimation of the number of paths, their amplitudes, delays and angles of arrival (AoAs). Let us remind that the AoA estimation necessitates the use of an antenna array at Rx side. In our measurements, we defined 5 x 5 uniform rectangular antenna array. The inter-space antenna was equal to the half of the wavelength of the highest frequency.

Similarly to the EM method, the SAGE algorithm is characterized by an Expectation step (E-step) and a Maximization step (M-step). The M-step is based on maximum likelihood (ML) detectors. It consists in testing all the possible values of the parameters of each path and retaining the most likely. The E-step is an interference cancellation function. It consists in cancelling the contributions of the interfering MPCs from the measured channel transfer function (CTF) allowing a better estimation of the considered MPC parameters in the M-step.

SAGE algorithm can be implemented in the time domain or in the frequency domain. We chose to implement it in the frequency domain which is mathematically more suitable for UWB signals.

- *Channel Transfer Function expression*

First of all, let us express the channel transfer function (CTF) measured on the m-th antenna at the n-th frequency point of the considered bandwidth. It is equal to the sum of all the MPCs contributions:

$$H(m,n) = \sum_{l=1}^{L} \alpha_l(n) \underbrace{\exp(-j2\pi f_n \tau_l)}_{\substack{\text{phase rotation} \\ \text{due to delay}}} \underbrace{\exp\left(-j2\pi \frac{\langle e(\phi_l,\theta_l), r_m \rangle}{\lambda_n}\right)}_{\substack{\text{phase rotation due to} \\ \text{antenna position and AoA}}} \underbrace{D(n,\phi_l,\theta_l)}_{\substack{=1 \\ \text{if isotropic} \\ \text{antenna}}} + W(m,n)$$

(4)

- l and L are the MPC index and the total number of MPCs respectively
- α_l is the amplitude
- τ_l is the delay
- ϕ_l and θ_l are the angles of arrival (AoA) in azimuth and in elevation respectively
- $e(\phi_l, \theta_l)$ is a unitary vector whose direction is that of the l-th path
- r_m is the coordinates vector of the m-th antenna
- λ_n is the wavelength for the frequency f_n
- $D(n, \phi_l, \theta_l)$ is the product of Tx and Rx complex antenna gains depending of the frequency f_n and the angles of arrival
- $W(m,n)$ is an additive white Gaussian noise sample.

- *E-step*

The E-step allows estimating the signal contribution of the *l*-th MPC by subtracting the other MPC contributions from the measured CTF as:

$$\widehat{X}_l = H - \sum_{\substack{l'=1 \\ l' \neq l}}^{L} \widehat{X}_{l'}(\widehat{\psi}_{l'})$$

(5)

where $\widehat{X}_l$ is the estimated contribution of the l-th MPC and $\widehat{\psi}_l$ represents the estimated parameters of the l-th MPC. This operation is performed by a parallel interference cancellation (PIC). However, it has been shown in [21] that in a rich multipath environment, a successive interference cancellation (SIC) has a better performance. In this scheme, the MPCs are ordered according to their received powers and the MPCs are estimated and cancelled successively from CTF. Thus, only the MPCs whose power is higher than that of the considered MPC are cancelled from the CTF.

$$\widehat{X}_l = H - \sum_{l'=1}^{l-1} \widehat{X}_{l'}(\widehat{\psi}_{l'})$$

- *M-step*

It is then possible to estimate the l-th MPC parameters using ML detectors, corresponding to the M-step. For this purpose, a correlation function is defined as:

$$z_l(\tau, \phi, \theta; \widehat{\boldsymbol{X}}_l) = \sum_{n=1}^{N} \sum_{m=1}^{M} \exp(+j2\pi f_n \tau) \, \exp\left(+j2\pi \frac{\langle e(\phi, \theta), r_m \rangle}{\lambda_n}\right) \times \hat{X}_l(m, n)$$

(6)

The M-step consists in testing all the possible τ, ϕ and θ values and retaining those which maximize the absolute value of the correlation function. In order to limit the complexity of this step, the parameters of each MPC are not estimated in parallel but successively. Classically, the first parameter to be estimated is the delay. For this purpose, the angles of arrival values estimated during the previous iteration are used in the correlation function as shown in equation (7)). Then, the angles of arrival are estimated taking into account the updated estimated delay.

$$\hat{\tau}_l^{(i)} = \arg\max_{\tau} \left| z_l(\tau, \hat{\phi}_l^{(i-1)}, \hat{\theta}_l^{(i-1)}; \widehat{\boldsymbol{X}}_l) \right|^2$$

$$\hat{\phi}_l^{(i)} = \arg\max_{\phi} \left| z_l(\hat{\tau}_l^{(i)}, \phi, \hat{\theta}_l^{(i-1)}; \widehat{\boldsymbol{X}}_l) \right|^2$$

$$\hat{\theta}_l^{(i)} = \arg\max_{\theta} \left| z_l(\hat{\tau}_l^{(i)}, \hat{\phi}_l^{(i)}, \theta; \widehat{\boldsymbol{X}}_l) \right|^2$$

(7)

Once the delay and the angles of arrival of a MPC are estimated, the amplitude is simply computed by the following equation:

$$\hat{\alpha}_l = \frac{1}{M} z_l(\hat{\tau}_l^{(i)}, \hat{\phi}_l^{(i)}, \hat{\theta}_l^{(i)}; \widehat{\boldsymbol{X}}_l)$$

(8)

Let us note that here, one average amplitude is estimated by MPC for all the bandwidth. In the case of an UWB channel, the amplitude can vary in the frequency domain. More particularly, the phase of the Tx and Rx antenna gains, which are included in this amplitude, can vary significantly. To limit this inconvenient, Haneda and Takada proposed in [23] to divide the considered frequency band in sub-bands. Hence, the M-step is performed in all the sub-bands in parallel. Thus, one estimated average amplitude is computed by sub-band by MPC. This method allows a better estimation of the MPC amplitude. However, it reduces the time resolution of the algorithm since it becomes function of the inverse of the sub-band width. In other words, the delay estimator performance decreases.

- *Initialization cycle*

At the start of the algorithm, no estimation of the MPC parameters is available. Therefore, no interference cancellation can be carried out for the estimation parameters of the first MPC and no estimated value of the angles of arrival is available for delay estimation of the MPCs. In [26], B. Fleury proposed an initialization cycle (i=0) in which a SIC is exploited for E-step and the correlation function is modified for M-step. More precisely, delay estimation is performed without taking into account the effects of the angles of arrival in the initialization cycle. The initialization allows providing not only initial estimations of the MPC parameters but also, an estimation of the total number of MPCs. For this purpose, SIC and M-step are performed successively until the estimated power of a MPC is not significant.

Different criterion can be used to determine if an estimated MPC is significant or not. It can be the comparison with the power of the strongest path or the noise power. A classical criterion used is the comparison of the regenerating CTF power (corresponding to the estimated interference in the E-step) with that of the measured CTF. For instance, if the regenerated CTF power is higher than 90% of the measured CTF power, it could be considered that the estimation of other MPCs parameters is not necessary. Unfortunately, it has been observed that the high-resolution algorithms do not completely capture all of the power from the measured impulse responses. The difference between the measured impulse responses and the reconstructed ones is usually referred to as the diffuse multipath components (DMC) [27] [28]. In the SAGE version we implemented, the criterion we use is the comparison between the measured noise power and the estimated path power. More precisely, we consider that a path is not significant if its estimated power is not at least 6 dB higher than the measured noise power. Figure 22 summarizes in a flow chart the initialization cycle principle of SAGE algorithm.

However, we observed that due to a non-reliable estimation of the delays and AoA, some MPCs power could be under-estimated at the initialization cycle. By not cancelling some of them, we observed that their powers could significantly increase with the iterations. Finally, some significant MPCs could be discarded in the initialization cycle. To overcome this problem, in the initialization cycle, to ensure no significant MPC will be discarded, the MPC power threshold is subtracted by 30dB. And at of SAGE processing, the MPC powers are compared to the correct threshold to select the final significant MPCs.
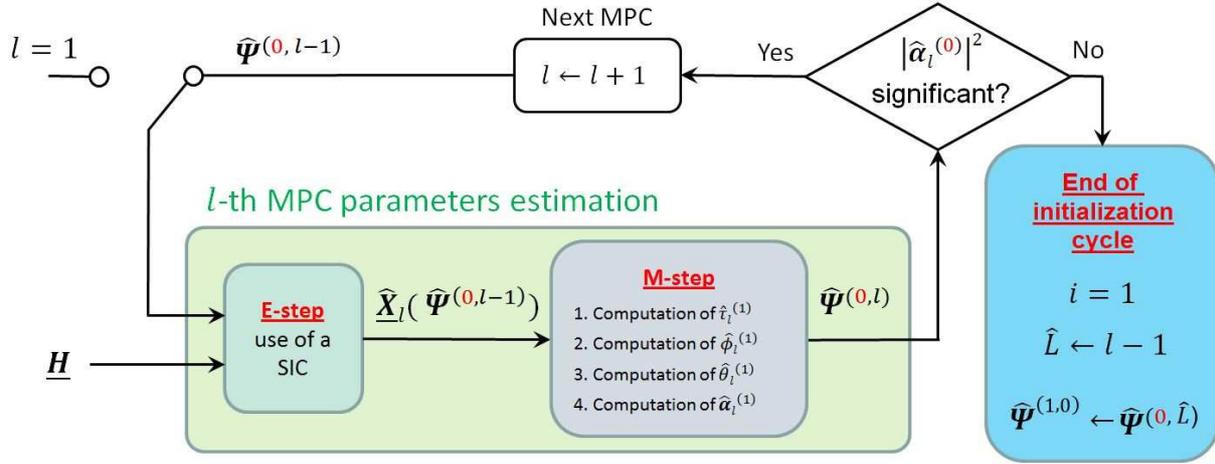
Figure 22: Flow chart of SAGE algorithm during the initialization cycle

3.4.2 CLUSTERING ALGORITHM

- *Distance metrics*

The clustering algorithms allow to gather MPCs with similar parameters in different clusters. The most famous clustering method used for channel modeling is the K-means algorithm [18]. It is based on the definition of distances between the MPCs and the centroid of the clusters. The latter corresponds to the center of the cluster taking into account the MPCs parameters. Similarly to the MPCs, it is defined by parameters such as the delay, the AoA, a power. We will see latter the exact definition of the centroids. A distance can be decomposed in the delay domain and the angular domain. The delay distance between a *l*-th MPC and a *k*-th centroid is given by:

$$d_{\tau,l,k} = \eta \times \frac{|\tau_l - \tau_k| \times \tau_{rms}}{\Delta\tau_{max}}$$

(9)

where $\Delta\tau_{max}$ represents the maximum delay difference between all the MPCs and the considered centroid, and η a coefficient which allows to give more or less importance to the delay distance compared with the angular one for the final distance computation. In the sequel, we will set the η value to 15. The angular distance writes:

$$d_{AoA,l,k} = \frac{1}{2}\left\{ \begin{pmatrix} \sin\theta_l \cos\phi_l \\ \sin\theta_l \sin\phi_l \\ \cos\theta_l \end{pmatrix} - \begin{pmatrix} \sin\theta_k \cos\phi_k \\ \sin\theta_k \sin\phi_k \\ \cos\theta_k \end{pmatrix} \right\}$$

(10)

Finally, the distance between a MPC and a centroid is defined by:

$$d_{l,k} = P_l \sqrt{\left\| d_{AoA,l,k} \right\|^2 + d_{\tau,l,k}}$$

(11)

- *K-means algorithm*

K-means algorithm is an iterative process. It does not estimate the number of clusters. Therefore, we have to set the number of clusters before launching this algorithm. The first step of this algorithm consists in choosing K MPCs as the centroids. The best MPCs to choose are the strongest ones in term of power. Then, the iterative process starts. One iteration is decomposed in 3 different steps:
    1. Computation of the distances between all the MPCs and all the centroids
    2. Affectation of each MPC to the closest centroid and so, to a cluster
    3. Re-computation of the centroids parameters according the updated clusters.

The centroid delay is given by:

$$\bar{\tau}_k = \frac{\sum_{l \in C_k}^{L_k} \tau_l \times P_l}{\sum_{l \in C_k}^{L_k} P_l}$$

(12)

where C_k corresponds to the set of MPCs belonging to the k-th cluster and L_k the number of MPCs in this cluster. The centroid AoA writes:

$$\bar{\phi}_k = \frac{\sum_{l \in C_k}^{L_k} \phi_l \times P_l}{\sum_{l \in C_k}^{L_k} P_l}$$

(13)

- *Estimation of the number of clusters*

To estimate the number of clusters, we first have to choose under which value, a cluster power is considered as insignificant [30]. In our case, we will set this threshold power value to 0.5% of the total SAGE regenerated channel power.

Logically, the greater the number of clusters, the smaller the number of MPCs by cluster and so, the lower the cluster powers. Therefore, a method to estimate the number of clusters is to launch the K-means algorithm with a very high number of clusters, to re-launch it with one less cluster if one of the cluster was not significant, and so on. Thus, the estimated number of clusters will correspond to the maximum number of clusters for which all the cluster powers are higher than the predefined threshold power.

In the sequel, SAGE and clustering results will be displayed in polar coordinates as in Figure 24 where the sub-figure on the left gives information on the MPC parameters estimated by SAGE, and that on the right gives clusters informations. In the sub-figure on the left, each MPC is represented by a point where the angle represents the estimated AoA in azimuth, the distance separating the points to the center of the circle represents the estimated time delays multiplied by the speed of the light in free space, and the color represents the MPC power. In the right sub-figures, each color represents a different cluster and the points which kernel is yellow represent the centroid of the clusters.
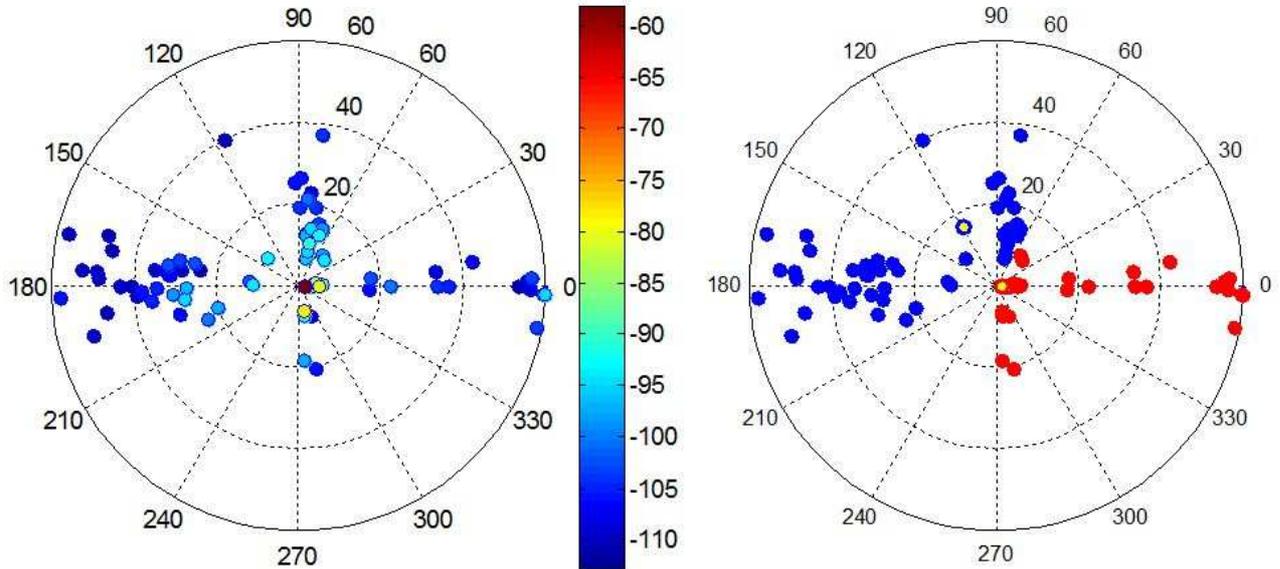
Figure 23 : SAGE (left) and Clustering (right) results – Isolated antenna – d_{off} = 1m – env 1
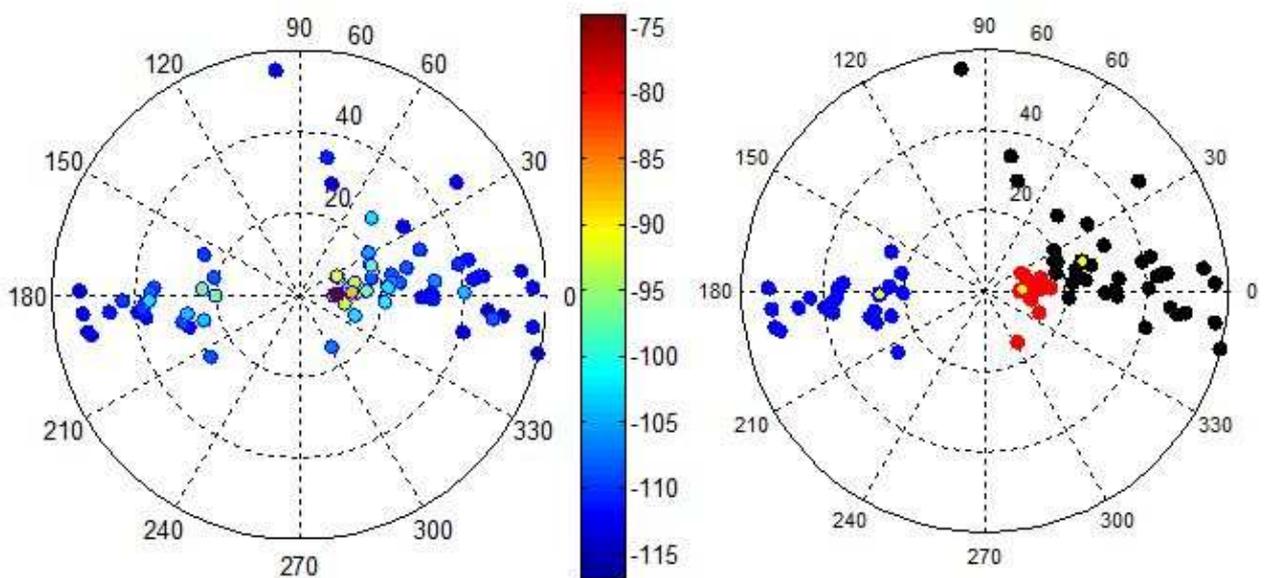
Figure 24 : SAGE (left) and Clustering (right) results – Isolated antenna – d_{off} = 8m – env 1

3.4.3   PARAMETER VALUES USED IN THE MODELING TOOLS

In Table 15, we summarize the SAGE and clustering parameter values used for the UWB Off-Body measurements processing. $\hat{P}_{AWGN,t}$ corresponds to the noise power estimated in time domain. Its estimation is based on the first samples of the measured CIRs. More precisely, the average power of the first samples of each CIRs (each one corresponding the CIR of one antenna) is computed.

Thus, M noise power estimations are obtained with M corresponding to the number of antennas. Another averaging on these M noise power estimations is carried out to obtain the final power noise estimation in time domain. The noise power in frequency domain $\hat{P}_{AWGN,f}$ is computed from the $\hat{P}_{AWGN,t}$ using a Fourier transform.

Number of SAGE iterations: I	51. 8
52. Minimum difference between two estimated delays by SAGE	1.5 x (1/sub-banwidth)
Time threshold power to clean the CIRs	$\hat{P}_{AWGN,t} + 6\,dB$
Power threshold for MPCs selection in the SAGE initialization cycle ($i = 0$)	$\hat{P}_{AWGN,f} - 30\,dB$
Power threshold for MPCs selection at the end of SAGE processing ($i = I$)	$\hat{P}_{AWGN,f} + 6\,dB$
Minimum cluster power	0.5% of the SAGE regenerated channel power
Delay weight for distance computation between centroids and MPCs: η	$\eta = 15$

Table 15 : SAGE and Clustering parameter values

3.5. CHANNEL TIME DISPERSION MODELING

In this paragraph, we propose to analyze the channel delay dispersion exploiting the delays and the powers of the MPCs estimated by SAGE algorithm. The expression of the channel delay dispersion is given by the following equation:

$$\tau_{rms} = \sqrt{\frac{\sum_{l=1}^{L} P_l \times (\tau_l - \tau_{mean})^2}{\sum_{l=1}^{L} P_l}}$$

(14)

where τ_{mean} represents the mean delay which expression is:

$$\tau_{mean} = \frac{\sum_{l=1}^{L} P_l \times \tau_l}{\sum_{l=1}^{L} P_l}$$

(15)

Figure 25, Figure 26 and Figure 27 (the left sub-figures) give the delay dispersion values for the Rx antenna located on the torso, the left shoulder and the back respectively. The isolated antenna case is also given as reference. More precisely, each measurement point given corresponds to the average value of the delay spreads estimated over all the distances, for a given body orientation, for a given environment, and for a Rx antenna location.

The general trend of the curves shows that the more the body hides the link between the AP and the Rx antenna, the higher the delay spread. Indeed, for the torso case, the delay spread value is minimum for Φ equal to 0° (LOS case), and maximum for Φ equal to 180° (NLOS case). For the shoulder case, the delay spread value is minimum for Φ equal to 0° (LOS case), and maximum for Φ equal to 90° (NLOS case). And for the back case, the delay spread value is minimum for Φ equal to 180° (LOS case), and maximum for Φ equal to 0° (NLOS case). These observations are identical to those made in [15] and in [7] for dynamic UWB On-Body communications scenarios.
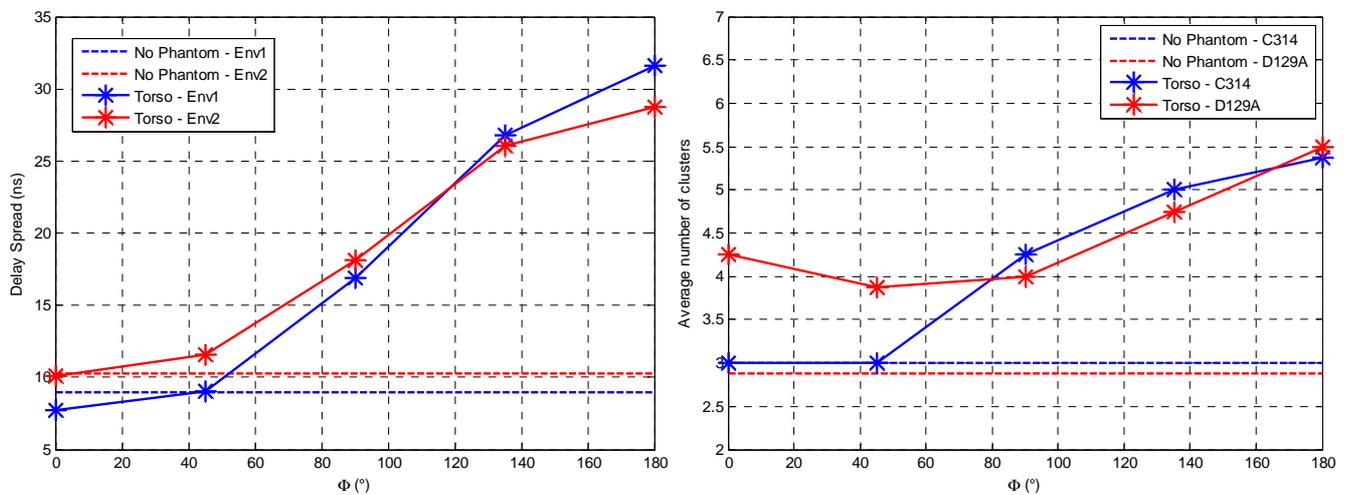
Figure 25 : Delay Spread (averaging over all the distances) versus Body orientation (left) – Estimated number of clusters (right) - Torso
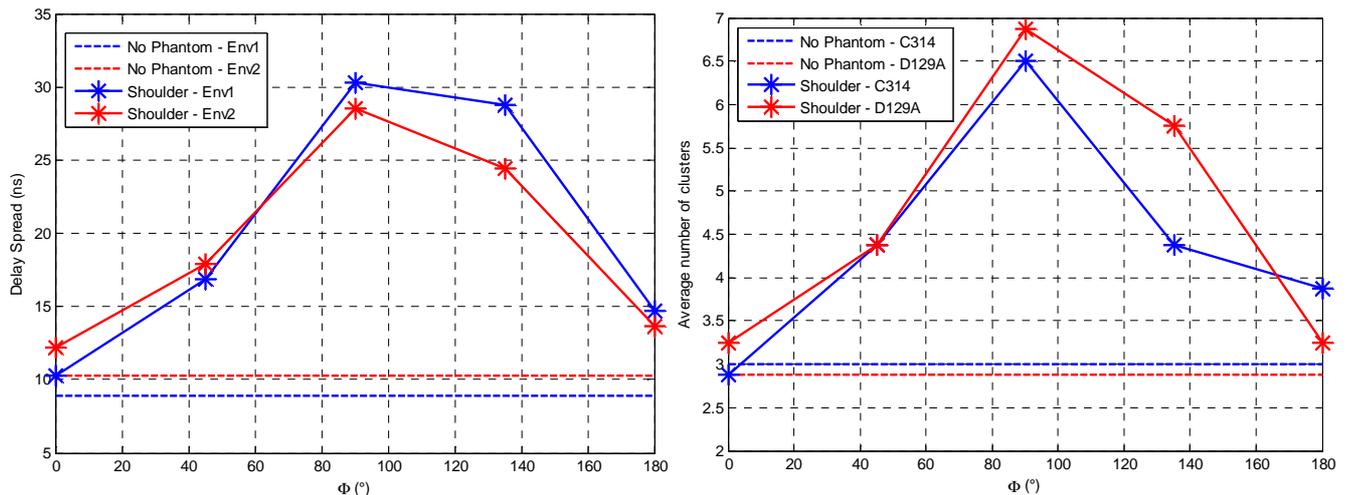
Figure 26: Delay Spread (averaging over all the distances) versus Body orientation (left) – Estimated number of clusters (right) - Shoulder
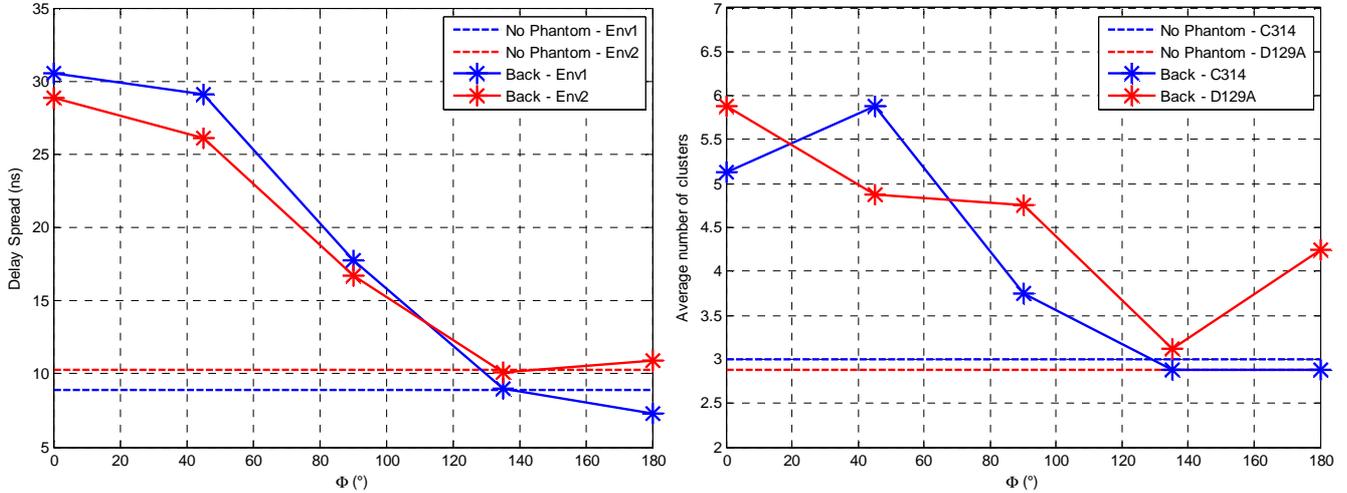
Figure 27: Delay Spread (averaging over all the distances) versus Body orientation (left) – Estimated number of clusters (right) – Back

Figure 25, Figure 26 and Figure 27 (the right sub-figures) also give the estimated number of clusters. Similarly to the given delay spread values, each point corresponds to the average number of cluster estimated over all the distances, for a given body orientation, a Rx antenna location and an environment.

By comparing, the left sub-figures (delay spread curves) with the right ones (estimated number of clusters), we remark that the general trend of the curves are very similar. The more the body hides the link between the AP and the Rx antenna, the greater the number of clusters. It could be partially explained by the fact that increasing the delay spread implies a greater number of clusters.

In **Table 16** and **Table 17**, we summarize the delay spread values to inject in the channel model. And we propose to use the closest integer values to set the number of clusters for each scenario to model the UWB Off-Body channel. These values are given in **Table 18** and **Table 19**.

	53. Isolated antenna	**54. Torso**	**55. Left Shoulder**	**56. Back**
$\Phi = 0°$	8.94 ns	7.70 ns	10.27 ns	30.52 ns
$\Phi = 45°$	8.94 ns	9.06 ns	16.87 ns	29.06 ns
$\Phi = 90°$	8.94 ns	16.87 ns	30.28 ns	17.79 ns
$\Phi = 135°$	8.94 ns	26.79 ns	28.79 ns	9.01 ns
$\Phi = 180°$	8.94 ns	31.59 ns	14.68 ns	7.30 ns

Table 16 : Delay spread versus Body orientation to use for the channel model – environment 1

	57. Isolated antenna	58. Torso	59. Left Shoulder	60. Back
Φ = 0°	10.23 ns	10.11 ns	12.17 ns	28.86 ns
Φ = 45°	10.23 ns	11.59 ns	17.88 ns	26.13 ns
Φ = 90°	10.23 ns	18.09 ns	28.56 ns	16.72 ns
Φ = 135°	10.23 ns	26.07 ns	24.44 ns	10.08 ns
Φ = 180°	10.23 ns	28.78 ns	13.68 ns	10.92 ns

Table 17 : Delay spread versus Body orientation to use for the channel model – environment 2

	61. Isolated antenna	62. Torso	63. Left Shoulder	64. Back
Φ = 0°	3	3	3	5
Φ = 45°	3	3	4	6
Φ = 90°	3	4	7	4
Φ = 135°	3	5	4	3
Φ = 180°	3	5	4	3

Table 18 : Number of clusters to use for the model - environment 1

	65. Isolated antenna	66. Torso	67. Left Shoulder	68. Back
Φ = 0°	3	4	3	6
Φ = 45°	3	4	4	5
Φ = 90°	3	4	7	5
Φ = 135°	3	5	6	3
Φ = 180°	3	5	3	4

Table 19 : Number of clusters to use for the model - environment 2

3.6. ANGULAR CHANNEL MODELING

The process of the measurements by SAGE algorithm also allowed an estimation of the azimuth angle-of-arrival (AoA) of the MPCs. Thus, we propose in this paragraph to analyze the body influences on the AoA probability density function (pdf) and to model its distribution for each scenario.

First of all, we remind the general body influences on the MPCs parameters. For that purpose, for each scenario, we display the MPCs parameters in polar coordinates. Figure 28, Figure 29, Figure 30 and Figure 31 correspond to the isolated antenna, the Rx located on the torso, the left shoulder and the back scenarios respectively, for a body orientation Φ equal to 0° and a distance equal to 8 m in the environment 1.

Logically, for the non-isolated antenna cases, we observe that the vast majority of the detected MPCs come from the side the antenna is located on the phantom. In the case the Rx antenna is

located on the back, we observe a couple of MPCs coming from the opposite side of the phantom with an estimated azimuthal AoA equal or close to 0°. They could correspond to creeping waves around the torso. Besides the estimated distances traveled by these MPCs are a little larger than d_{off}. This little difference of distance could correspond to the distance traveled by the waves around the torso of the phantom. More examples on SAGE and clustering results are given in the Annexes.
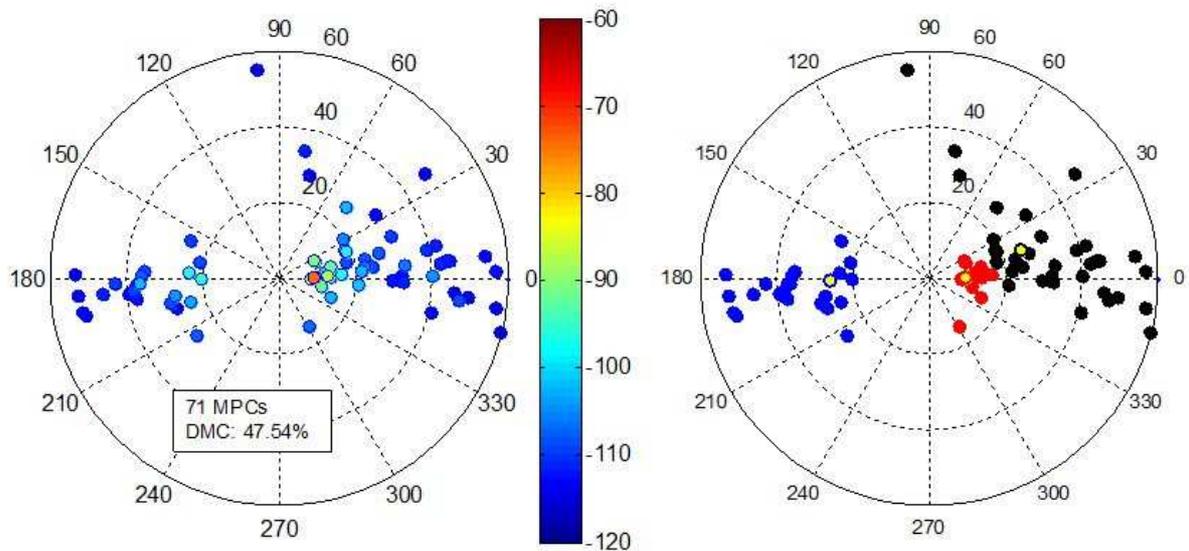
Figure 28 : Estimated MPCs and clusters – Isolated antenna - d_{off} = 8m – environment 1
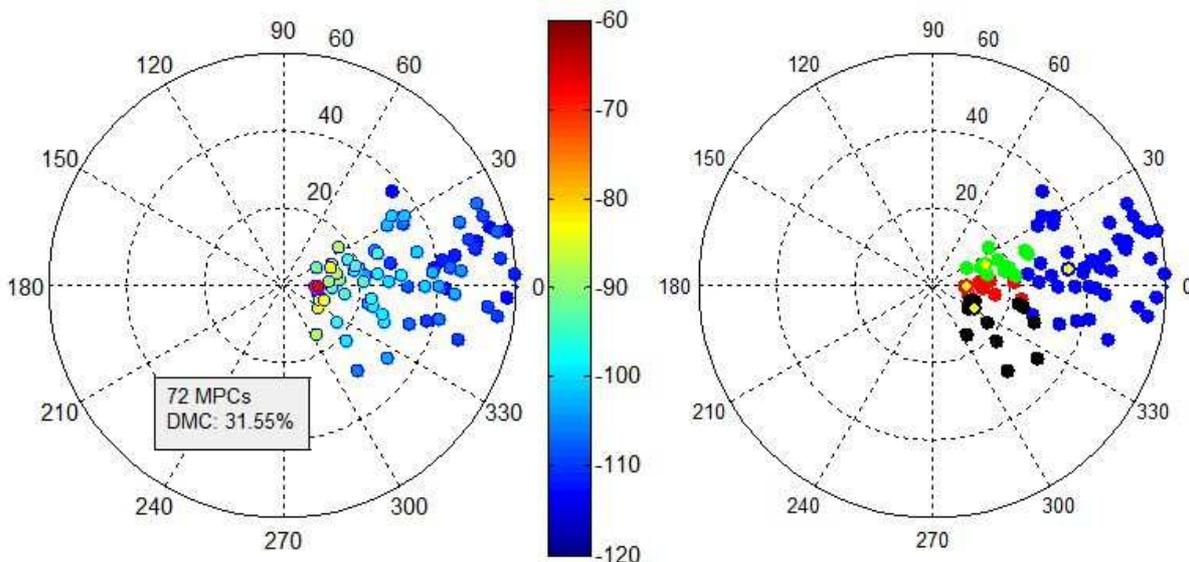
Figure 29 : Estimated MPCs and clusters – Torso - Φ = 0° - d_{off} = 8m – environment 1
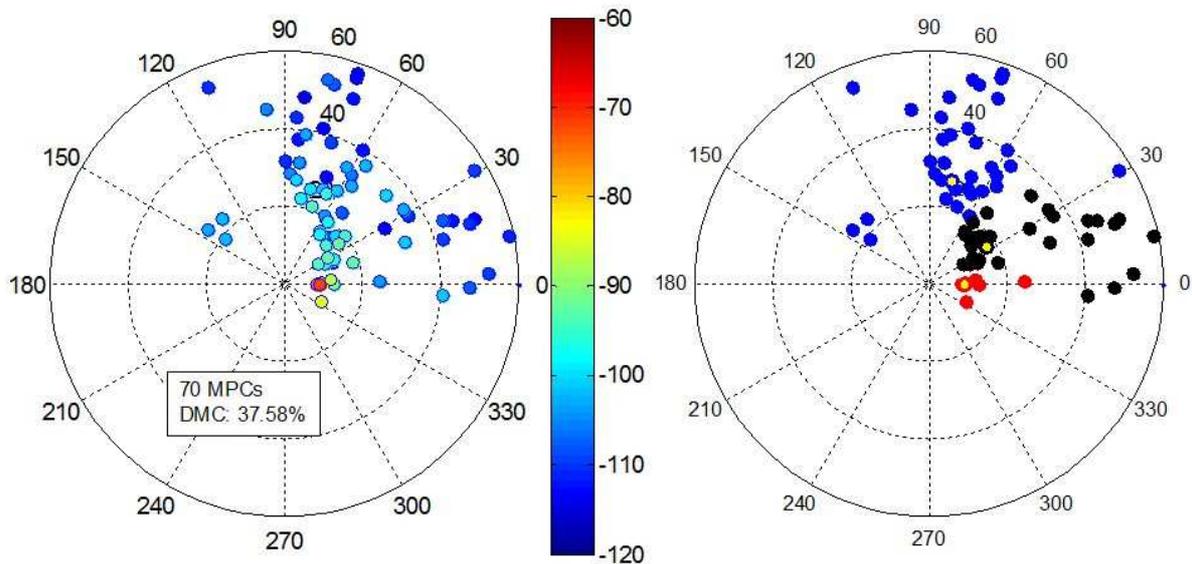
Figure 30 : Estimated MPCs and clusters – Shoulder - Φ = 0° - d_{off} = 8m – environment 1
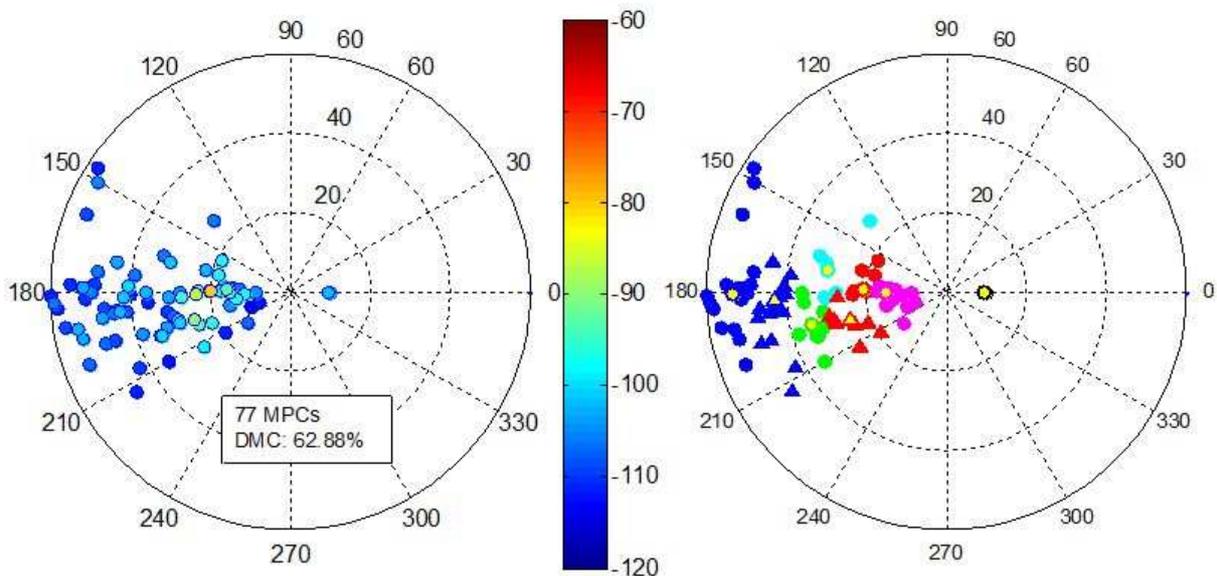
Figure 31 : Estimated MPCs and clusters – Back - Φ = 0° - d_{off} = 8m – environment 1

In order to characterize the MPCs AoA properties, we give the AoA probability density functions (pdf) for some scenarios. Let us note that the given AoA pdf take into account the estimated AoA over all the distances, for a given body orientation, a given Rx location and a given environment. The other AoA pdf are given in the Annexes.
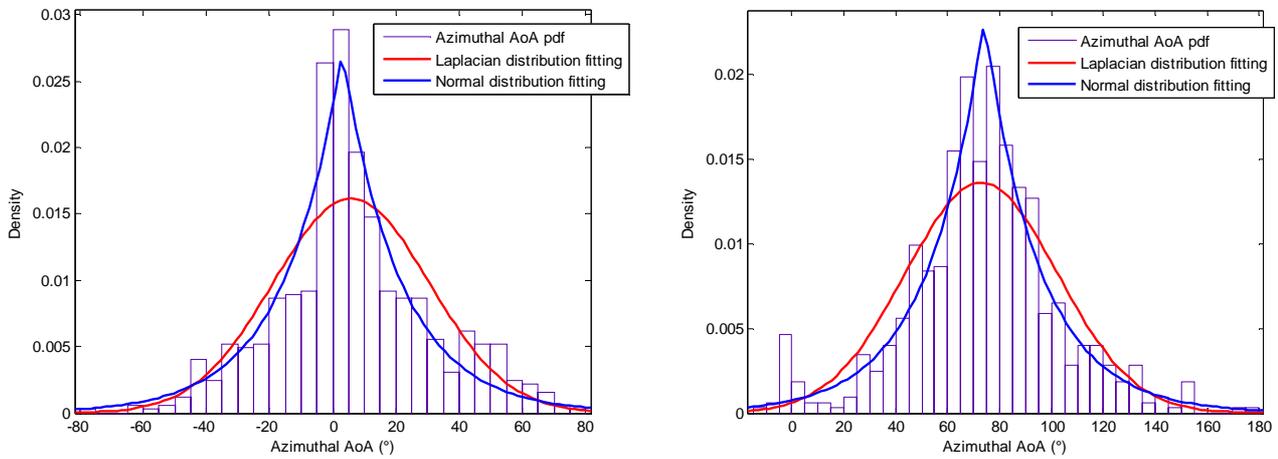
Figure 32 : Azimuthal AoA pdf - Torso - Φ = 0° (left) and 90° (right) - environment 1
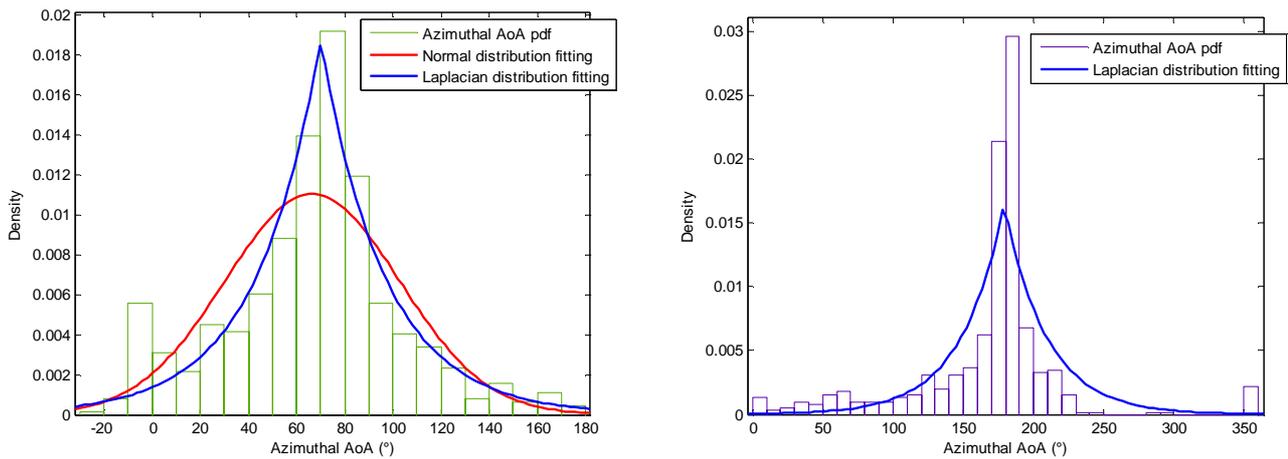
Figure 33 : Azimuthal AoA pdf - Shoulder - Φ = 0° (left) and 90° (right) - environment 1
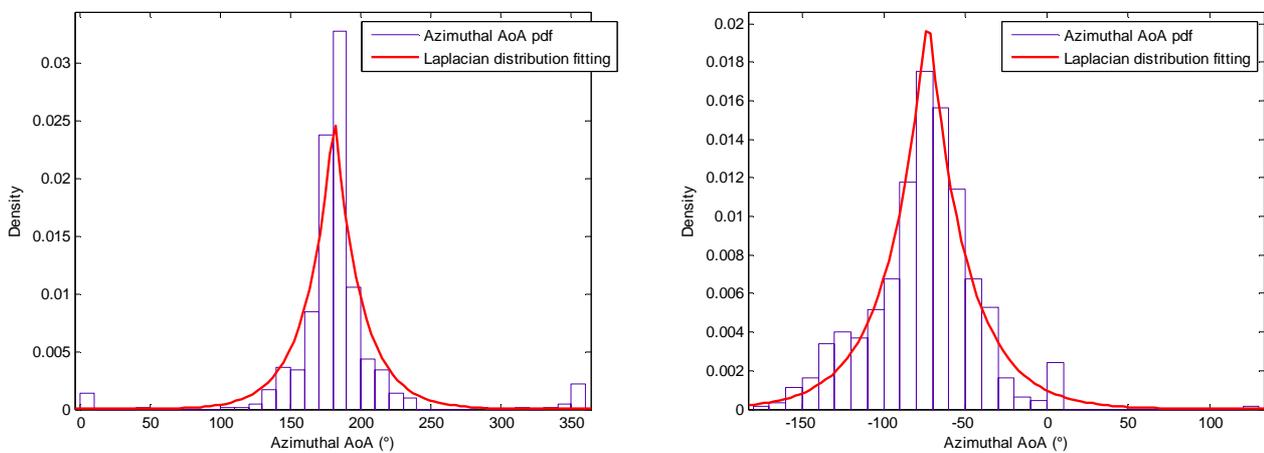
Figure 34 : Azimuthal AoA pdf - Back - Φ = 0° (left) and 90° (right) - environment 1

We observe that the Laplacian distribution is well suited to model the AoA pdf. The Laplacian distribution is described by the following equation:

$$pdf(\phi) = \frac{1}{2\sigma} \, exp\left(-\frac{|\phi - \phi_{mean}|}{\sigma}\right)$$

(16)

with ϕ_{mean} the mean AoA of the distribution and $2\sigma^2$ the variance.

3.6.1 AVERAGE MEAN AOA

Figure 35 gives the estimated ϕ_{mean} values for all the on-body antenna location, all the body orientations and both environments. For a given Rx location, it seems that ϕ_{mean} varies linearly with the body orientation. Therefore, we propose to model the mean AoA by performing a linear regression as described in the following equation:

$$\phi_{mean} = p_1\Phi + p_2$$

(17)

The estimated p_1 and p_2 parameters are given in **Table 20**. Thus, it is possible to model the mean AoA whatever the body orientation even if the measurements have been performed for five body orientations only.
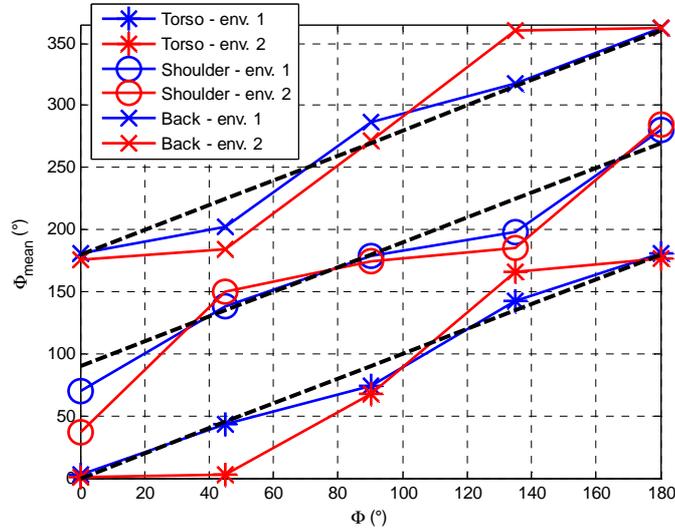
Figure 35 : Estimated mean AoA corresponding ϕ_{mean} to the Laplacian distribution versus the body orientation Φ

	69. p₁	**70. p₂**
71. Torso – env 1	1.01	-2.4°
env 2	1.14	-20°
Shoulder – env 1	1.07	77°
env 2	1.18	60.2°
Back – env 1	1.06	174.4°
env 2	1.22	161.2°

Table 20 : *p₁* and *p₂* values for the mean AoA modeling in function of the body orientation and the environment

3.6.2 AVERAGE AoA VARIANCE

According to equation (16), to model the AoA with a Laplacian distribution, we also have to determine the σ values. This parameter gives information about the angular spread since the variance of the Laplacian distribution is given by $2\sigma^2$.

Figure 36, Figure 37 and Figure 38 give the estimated σ parameter value for Rx located on the torso, the left shoulder and the back respectively in function of the body orientation Φ for both environments. For a given Rx, it appears that σ value evolves similarly in both environments in function of the body orientation. This could be explained by the geometry of the rooms where the measurements have been performed. Both rooms have a rectangular shape. According to the body orientation and the Rx location, Rx antenna can detect MPCs generating by reflections from one or several walls, thus causing a low or great angular spread. In Figure 39, Figure 40, Figure 41, Figure 42 and Figure 43, we attempt to roughly illustrate the possible propagation phenomena which could explain the variation of σ values in function of the body orientation in the case Rx is located on the shoulder.
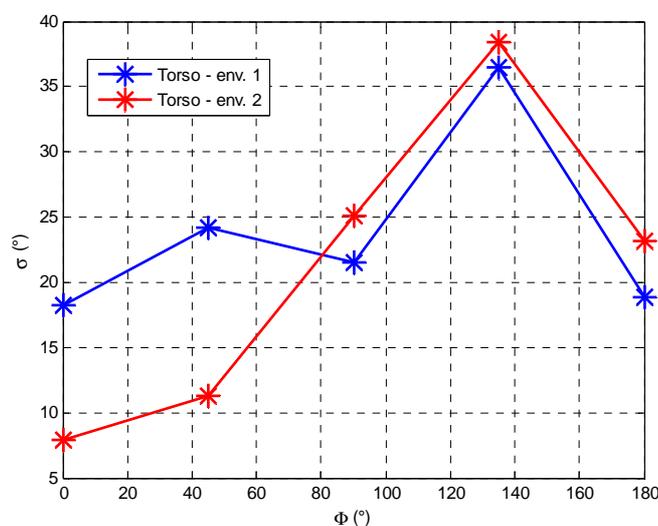
Figure 36 : σ parameter value in function of the body orientation – Torso
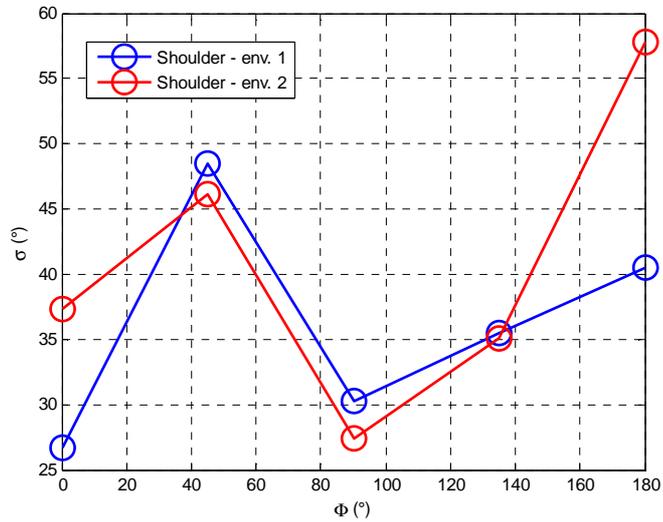
Figure 37 : σ parameter value in function of the body orientation – Shoulder
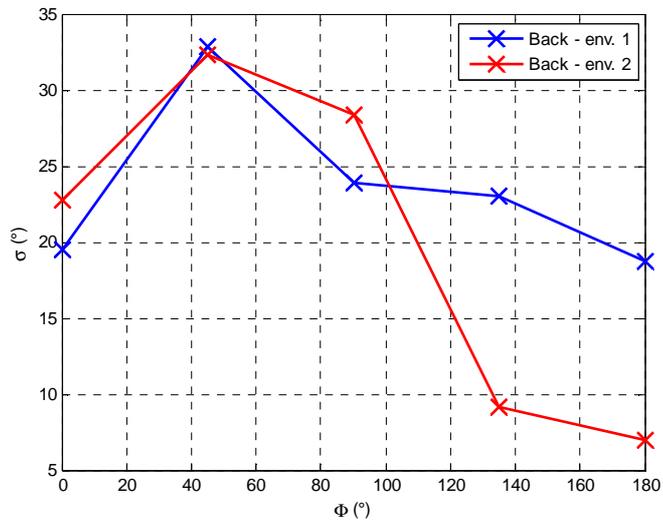
Figure 38 : σ parameter value in function of the body orientation – Back
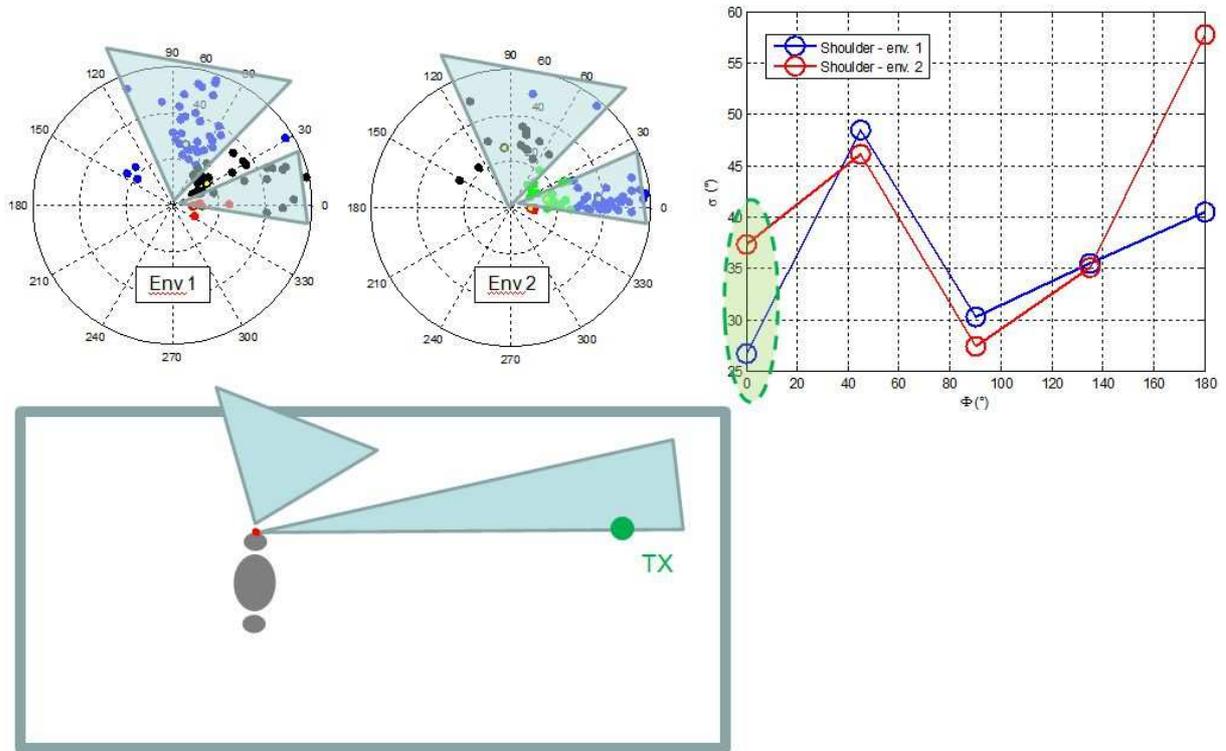
Figure 39 : Illustration of AoA spread – Shoulder - Φ = 0°
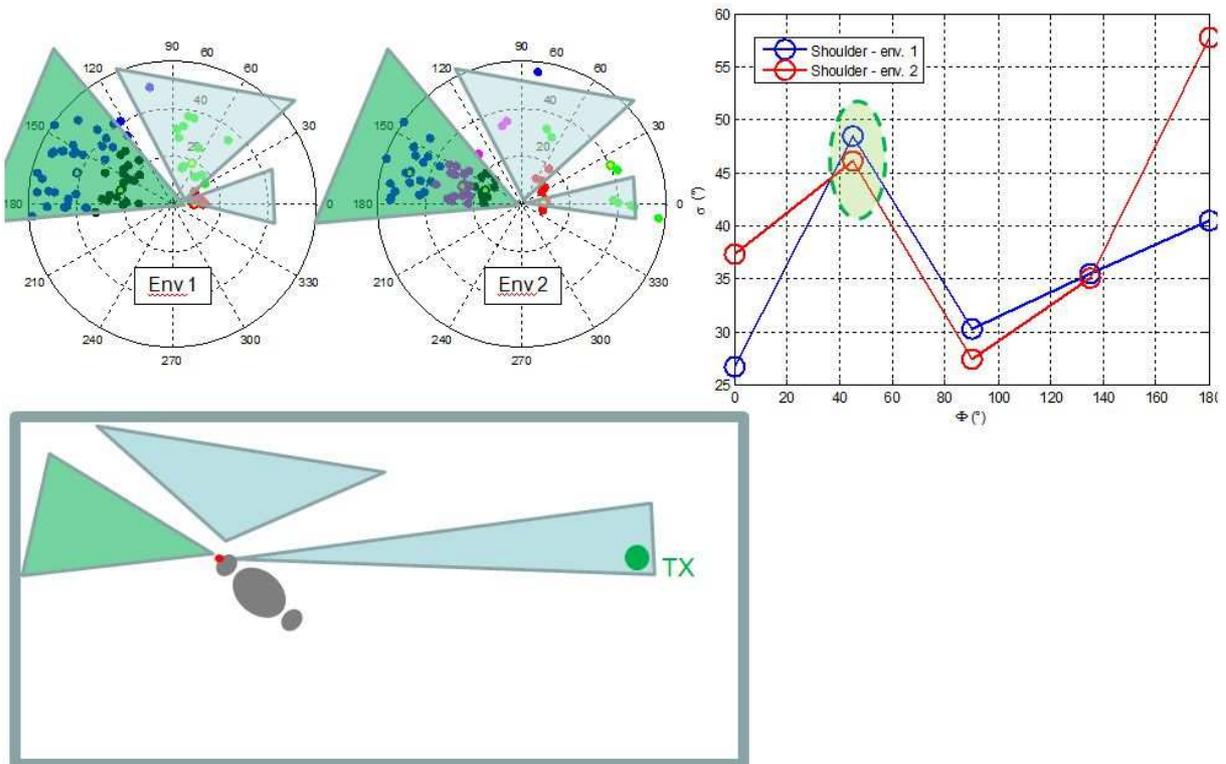
Figure 40 : Illustration of AoA spread – Shoulder - Φ = 45°
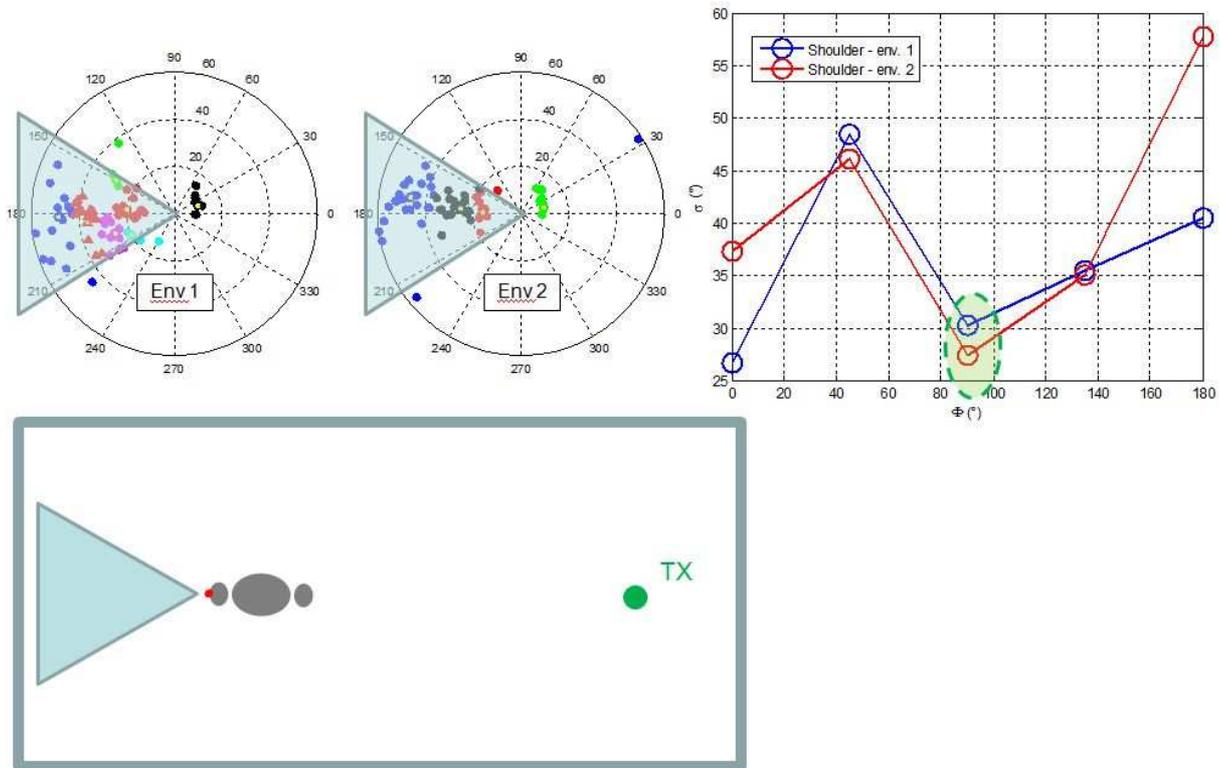
Figure 41 : Illustration of AoA spread – Shoulder - Φ = 90°
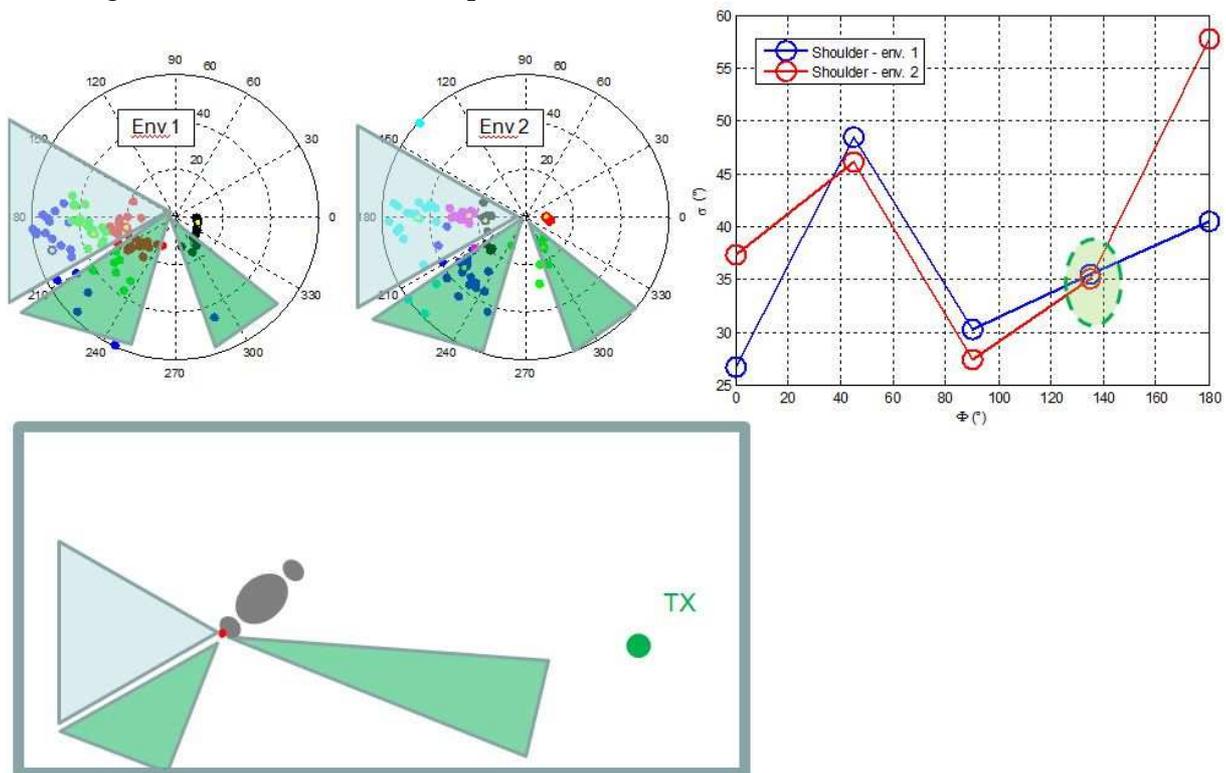
Figure 42 : Illustration of AoA spread – Shoulder - Φ = 135°
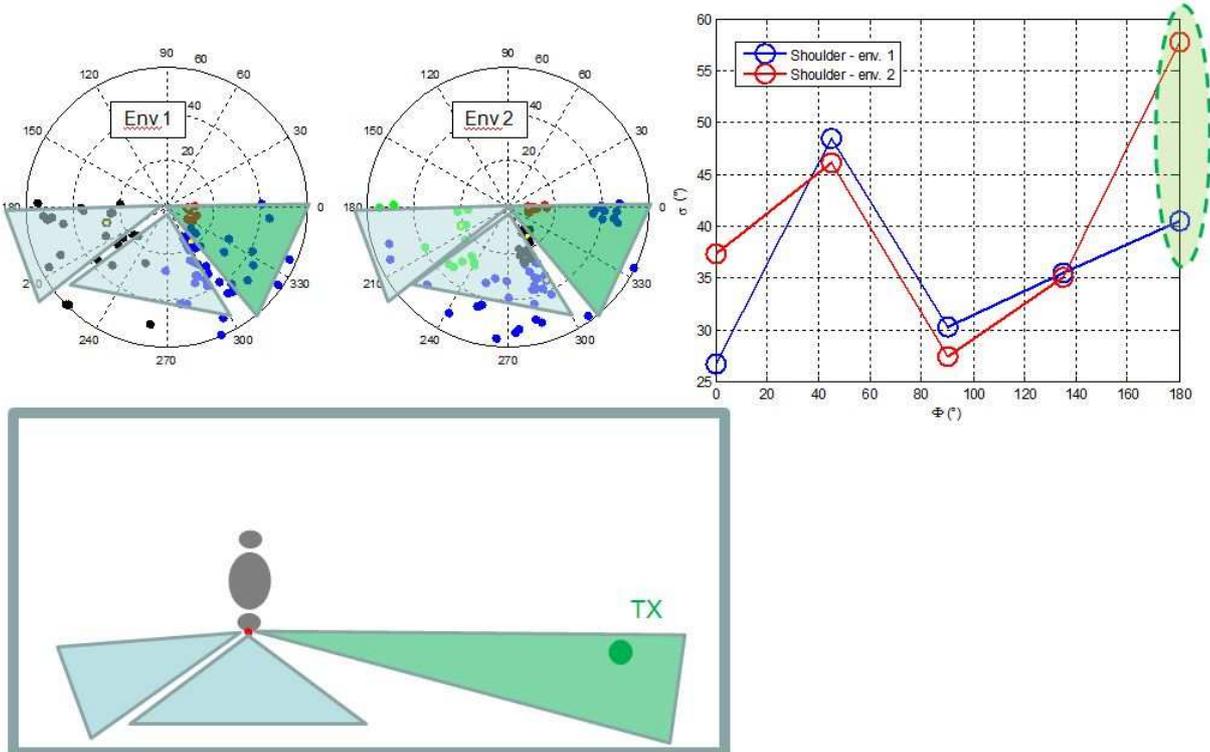
Figure 43 : Illustration of AoA spread – Shoulder - $\Phi = 180°$

3.7. CLUSTER ANGULAR-DELAY SPREAD

As far as here, we characterized and modeled the channel time and angular spreads. In this sub-section, we propose to analyze the angular and delay spreads of the estimated clusters. The cluster delay spread expression is similar to that defined in equation (14) for the channel delay spread. It writes:

$$\tau_{k,rms} = \sqrt{\frac{\sum_{l \in C_k}^{L_k}(\tau_l - \bar{\tau}_k)^2 \times P_l}{\sum_{l \in C_k}^{L_k} P_l}}$$

(18)

And the cluster angular spread expression is:

$$\Phi_{k,rms} = \sqrt{\frac{\sum_{l \in C_k}^{L_k}(\phi_l - \bar{\Phi}_k)^2 \times P_l}{\sum_{l \in C_k}^{L_k} P_l}}$$

(19)

Figure 44 and Figure 45 illustrate cluster delay and angular spreads. All the cluster delay and angular spread values are given in the Annexes.
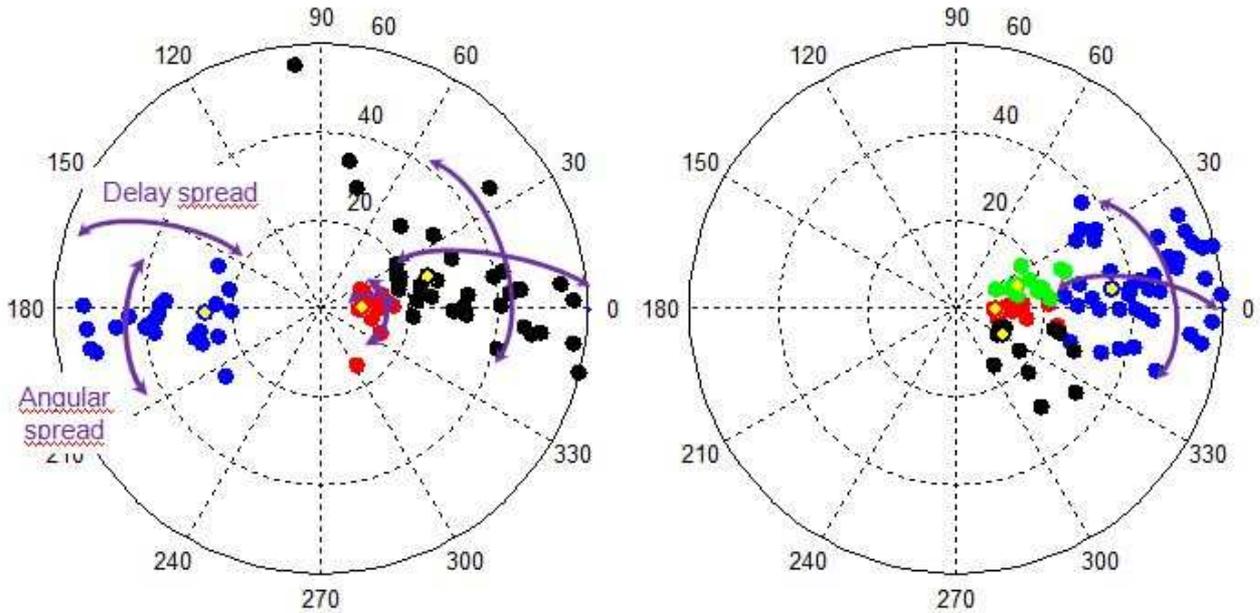
Figure 44 : Clustering results – Isolated antenna (left) and Torso (right) – env 1 – $\Phi = 0°$ - $d_{off} = 8$ m
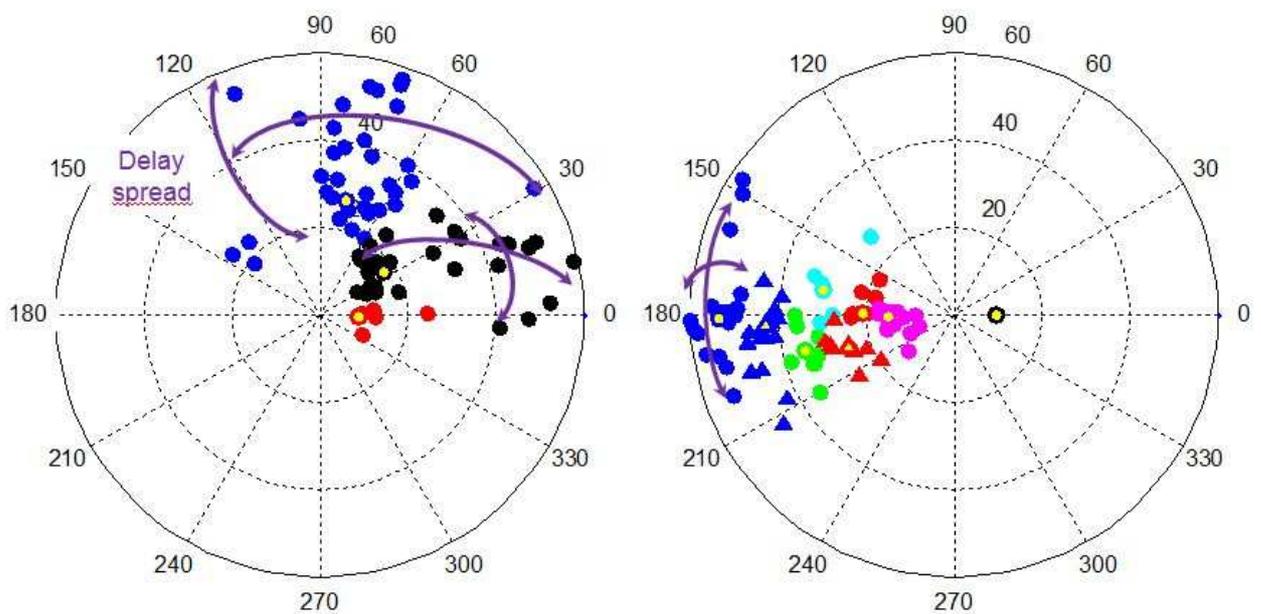
Figure 45 : Clustering results – Shoulder (left) and Back (right) – env 1 – $\Phi = 0°$ - $d_{off} = 8$ m

By observing the clustering results, we remarked that the higher the delay centroid of a cluster, the higher the corresponding angular spread. Figure 46 illustrates well this characteristic. We clearly see that the latter a cluster arrives in time, the larger it will be in the angular domain. For instance,

the cluster in blue, corresponding to the last cluster in delay domain, has the higher angular spread. On the contrary, the cluster in red, corresponding to the first cluster in delay domain, has the lowest angular spread.
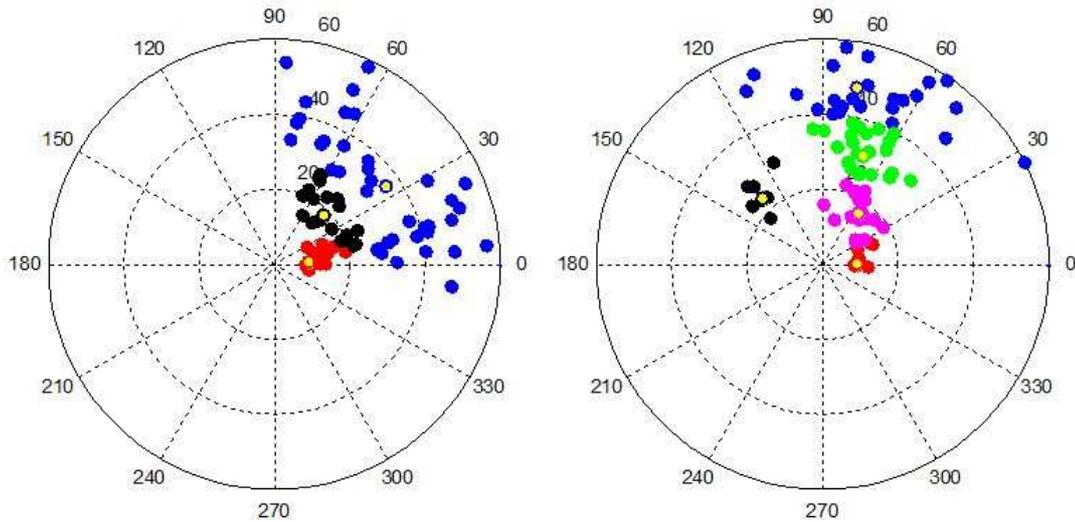
Figure 46 : Clustering results – Torso – env 1 - Φ = 45° (left) and 90° (right)

To ensure the dependence of the cluster angular spreads to the delay centroids, we display in Figure 47, Figure 48 and Figure 49, the cluster angular spread values versus the centroid delays for Rx located on the torso, the left shoulder and the back respectively. More precisely, each figure corresponds to one environment, one Rx location, all the distances and all the body orientations. We remark that the cluster angular spread values are roughly linearly dependent to the centroid delay values. Thus, we propose to model the azimuthal AoA spread in function of the centroid delay according the following equation:

$$\phi_{rms,k} = p_1 \bar{\tau}_k + p_2$$

(20)

The parameter values p_1 and p_2 estimated from the data plotted in Figure 47, Figure 48 and Figure 49, are given in **Table 21**. Let us note that these values strongly depend of the clustering algorithm parameters, especially on the parameter η which determines the importance of the MPC delays compared with the AoA to determine the clusters.

	72. p_1 (°/ms)	73. p_2 (°)
74. **Torso – env 1**	77.71	6.64
env 2	38.05	8.03
Shoulder – env 1	53.31	9.91
env 2	45.90	8.5
Back – env 1	59.64	7.58
Env 2	52.35	5.09

Table 21 : p_1 **and** p_2 **values for cluster AoA spread modeling in function of centroid delay**
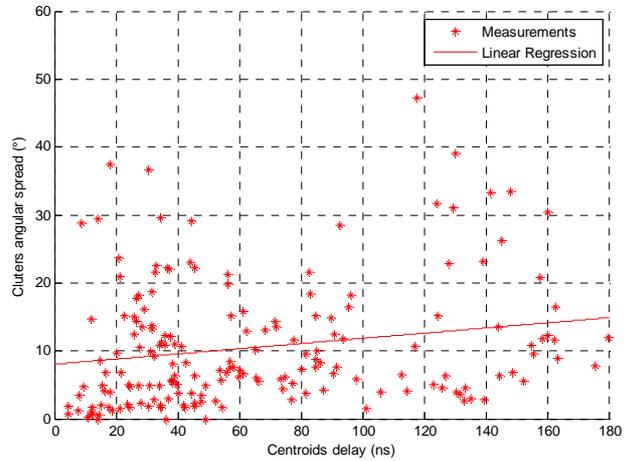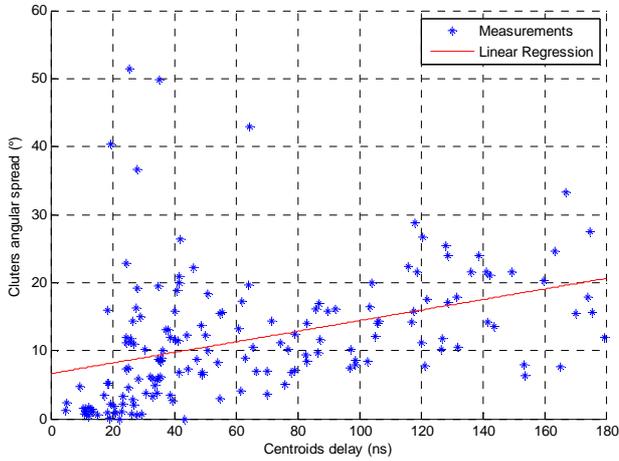
Figure 47 : Cluster AoA spread versus Centroid delay – Torso – env 1 (left) and env 2 (right)
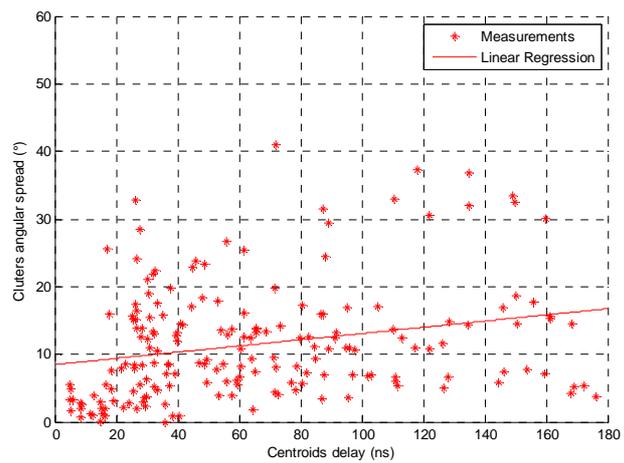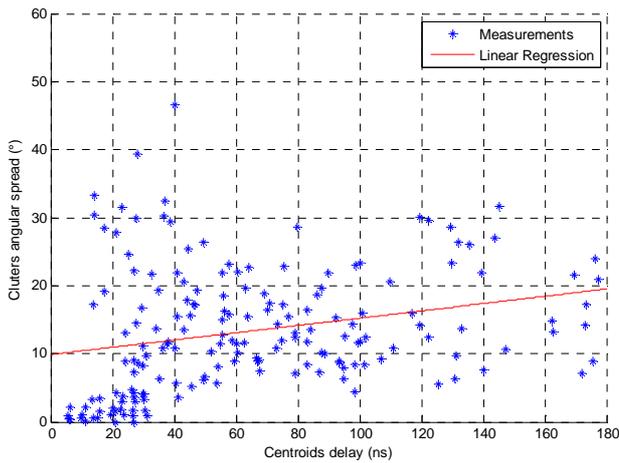
Figure 48 : Cluster AoA spread versus Centroid delay – Shoulder – env 1 (left) and env 2 (right)
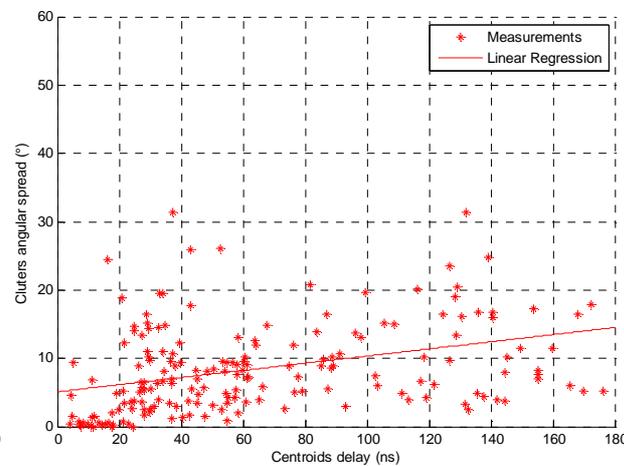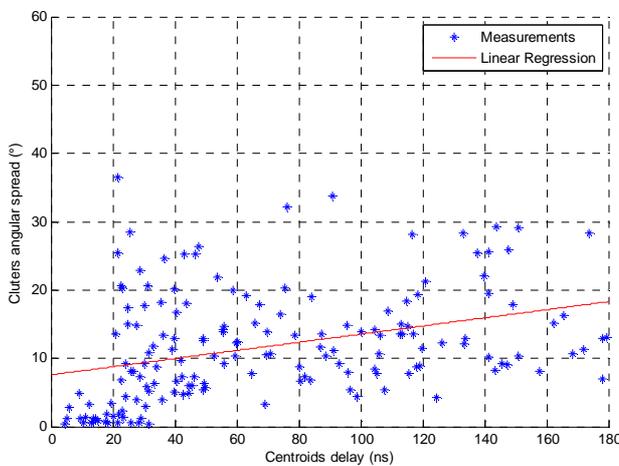
Figure 49 : Cluster AoA spread versus Centroid delay – Back – env 1 (left) and env 2 (right)

PROGRAMME
INFRASTRUCTURES MATERIELLES
ET LOGICIELLES POUR LA SOCIETE
NUMERIQUE – ED. 2011

ANR

CORMORAN

3.8. DIFFUSE MULTI-PATH COMPONENTS

In the literature, it is stated that the high-resolution algorithms for channel parameters estimation such as SAGE allow the estimation of specular MPCs only [28] [29]. Indeed, after removing the SAGE regenerated CIR from the measured CIR, we observe a residual CIR which power is significant. Examples are given in Figure 50 and Figure 51 correspond to the case Rx is located on the torso, for a phantom orientation equal to 0° and 180° respectively.

This residual signal is known as the diffuse multi-path component (DMC) of the channel. It is mainly due to non-discrete signal components present in the propagation channel, and to the superposition of MPCs that have a power too low to be extracted with any high-resolution algorithms.
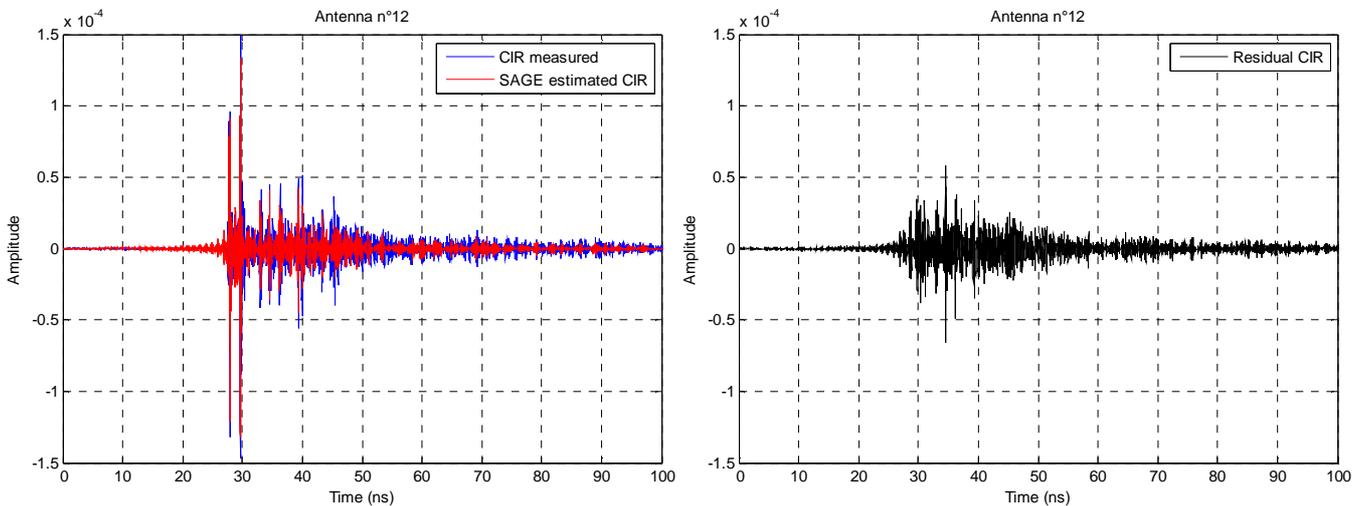
Figure 50 : Measured (left), SAGE regenerated (left) and residual (right) CIRs – Torso - d_{off} = 8m – Φ = 0° - env 1
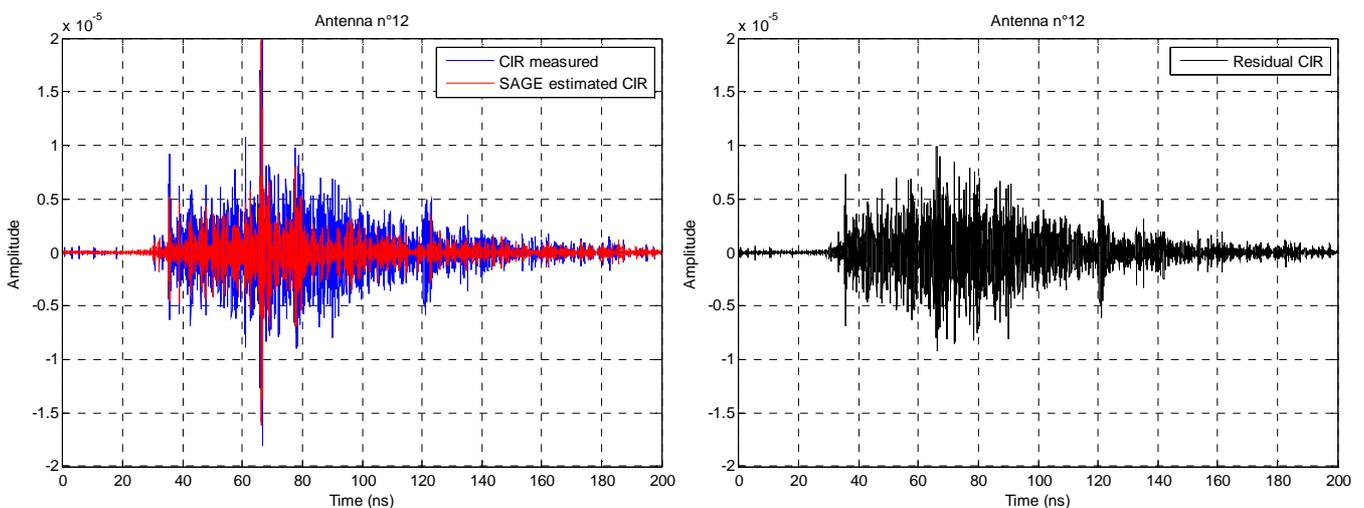
Figure 51 : Measured (left), SAGE regenerated (left) and residual (right) CIRs – Torso - d_{off} = 8m – Φ = 180° - env 1

In this sub-section, we propose to analyse the amount of DMC in UWB Off-Body channels. For that purpose, we define the relative DMC power as:

$$DMC = \sum_{f=f_{min}}^{f_{max}} |H_{meas} - H_{sage}|^2 \Big/ \sum_{f=f_{min}}^{f_{max}} |H_{meas}|^2$$

(21)

Figure 52, Figure 53 and Figure 54 give the relative DMC powers in % for Rx located on the torso, the shoulder and the back respectively. For both environments, it clearly appears that the more the channel is in LOS condition, the lower the amount of DMC is. The DMC is the lowest for a body orientation :

- $\Phi = 0°$ for Rx located on the torso
- $\Phi = 0°$ and $\Phi = 180°$ for Rx located on the shoulder
- $\Phi = 180°$ for Rx located on the back.

This means that in NLOS conditions, the channel contains more DMC. For the body orientations the amount of DMC is lowest, we observe that the higher the distance d_{off}, the higher the amount of DMC. In LOS conditions, the direct path is the strongest one in term of power. It is a specular path and not a diffuse path. The higher the distance between the AP and the Rxs, the lower the direct path power and so, the lower its power relatively to the total channel power. This can explain why in LOS conditions, the higher the distance d_{off}, the higher the DMC relative power. On the contrary, for NLOS conditions, i.e. for :

- $\Phi = 180°$ for Rx located on the torso
- $\Phi = 90°$ for Rx located on the shoulder
- $\Phi = 0°$ for Rx located on the back,

the amount of DMC seems to not be depend to the distance. This can be explained by the fact that in NLOS conditions, there is no direct path, which provides less power from specular waves. Tables of the measured DMC values are given in the Annexes.
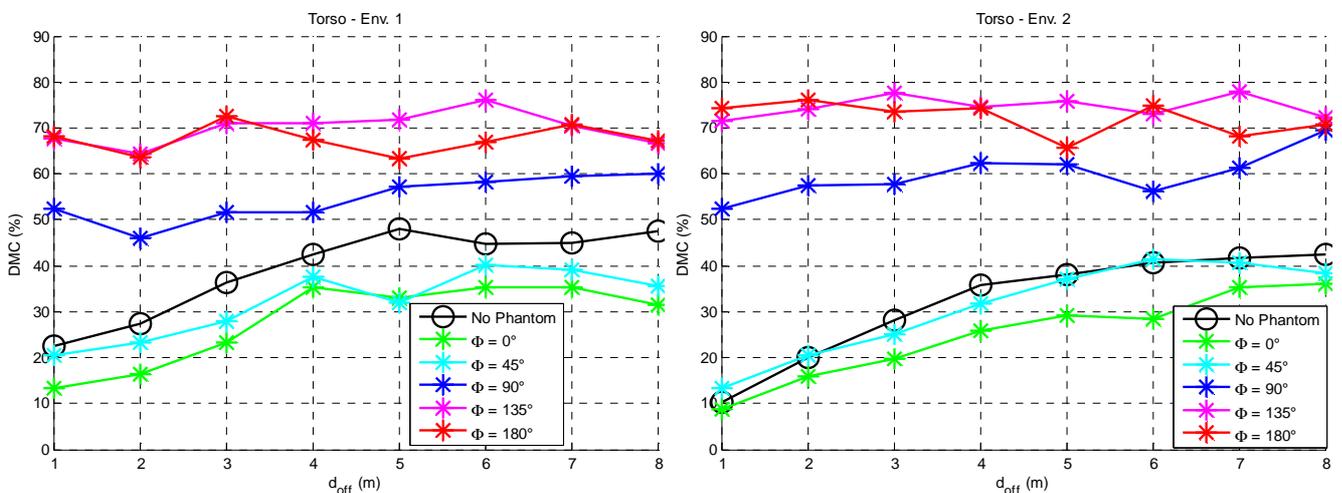
Figure 52 : Relative DMC power (in %) – Torso – env 1 (left) and env 2 (right)
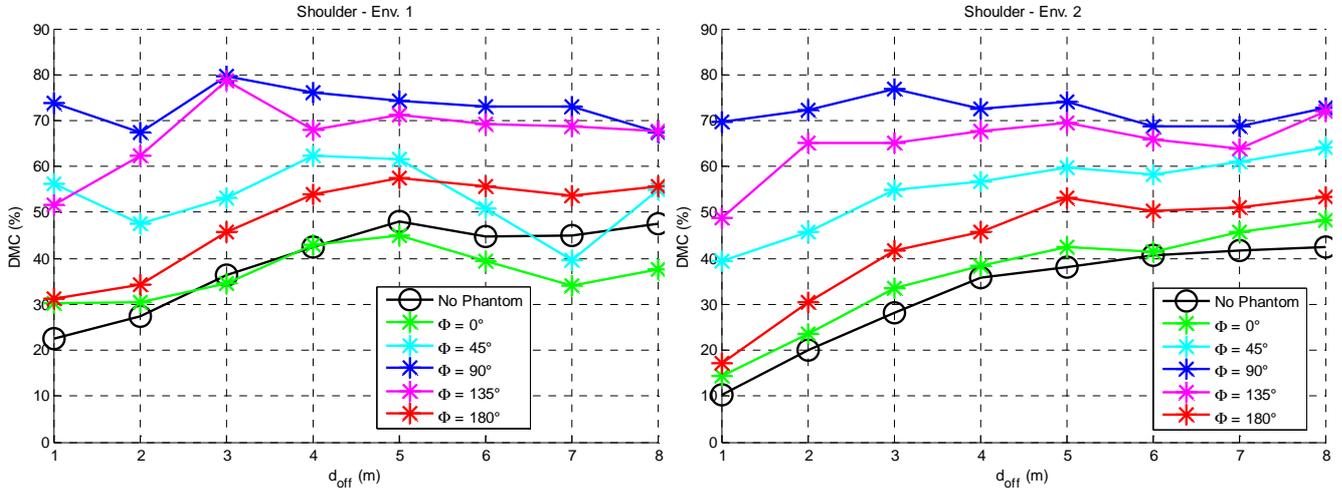
Figure 53: Relative DMC power (in %) – Shoulder – env 1 (left) and env 2 (right)
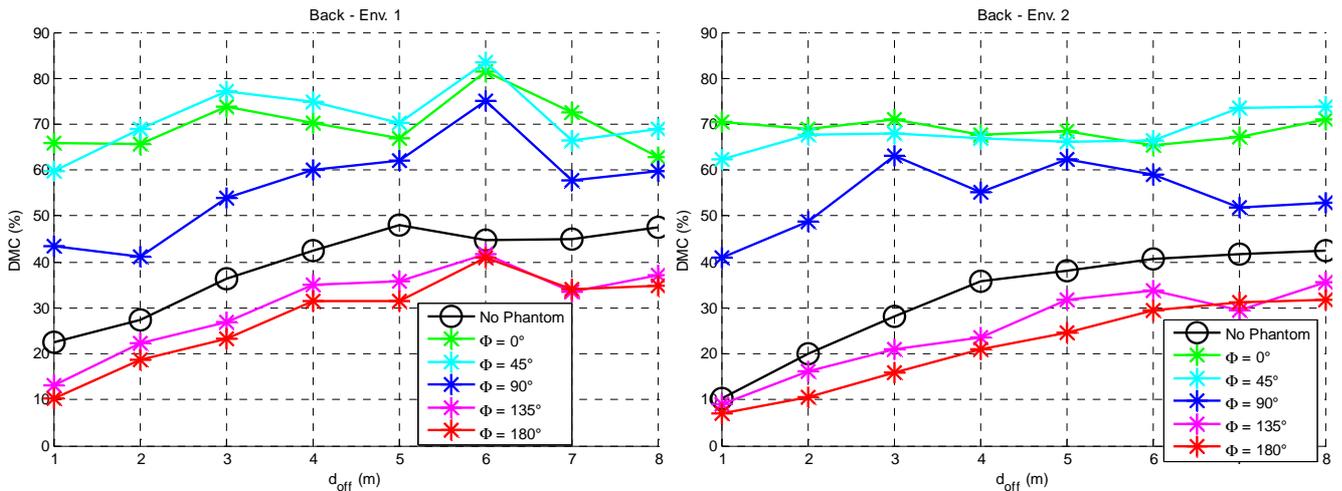
Figure 54 : Relative DMC power (in %) – Back – env 1 (left) and env 2 (right)

3.9. CONCLUSION AND INPUTS FOR THE OTHER TASKS

In this section, a deep investigation of Off-Body channels have been performed and some models have been proposed. First of all, the narrow band channel models already presented in D2.2 have been reminded. Then, UWB channel measurements performed at CEA-Leti have been described. From these measurements, an UWB Off-Body path loss model have been proposed. Tables giving parameter values to model the path loss are given and are so, exploitable for the other tasks of CORMORAN project.

The other analysis and modeling have been possible thanks to the developement of a high-resolution algorithm for channel parameters estimation namely SAGE, and that of a clustering algorithm. Thus, deep analysis of the channel time dispersion and the channel angular distribution have been carried out. More precisely, evolution of the channel time dispersion in function of the Rx antenna and the body orientation is investigated. And the channel azimuthal angular is

modeled by a Laplacian distribution. The parameters of the latter are also modeled in function of the Rx antenna location and the body orientation. Processing the SAGE estimates with the clustering algorithm allowed to analyze the cluster delays and AoA characteristics. And a way to model the cluster angular dispersion from the centroid delays is proposed. All these analysis should allow validating the Off-Body deterministic channel model proposed by UR1, which will be presented in the next section. Finally, the amount of DMC power which is not estimated by SAGE algorithm is investigated.

4. OFF–BODY DETERMINISTIC CHANNEL MODELING

4.1. INTRODUCTION

In this section, we used the Deterministic simulator *PyLayers* to reproduce the measurement conditions that have been presented in the previous sections. The goal is to check the ability of *PyLayers* tool to provide rich channel information in a rather controlled scenario. This is a prerequisite before moving toward more advanced scenarios involving body mobility and large scale mobility. The results here presented have been obtained by means of *PyLayers*, in scenarios close to the one measured in §3.2 of this document and in [3] .

The antennas pattern for the off-body node, i.e. a wire-patch monopole antenna, and the on-body node, i.e. the planar disc monopole [1], have been included in the ray-tracing simulation.

4.2. SIMULATION SETUP

4.2.1 DESCRIPTION OF THE SIMULATED ENVIRONMENT

The simulated environment is described in the specific *PyLayers* format, through a specific editor. The simplified layout is presented in Figure 55, which is a description of the environment presented in Figure 14, without taking into account the large table in the room. The 3 internal walls are of PARTITION type while the outside wall is of WALL type.

PARTITION and WALL corresponding to the following parameters:

- **PARTITION**: 10cm of PLASTER(ε_r= 8 , σ= 0.038)
- **WALL:** 7cm of BRICK(ε_r= 4.9, σ=0.3)

Notice that the slab thickness is not realistic when considering the actual values of thickness wall. The most relevant for the simulation is to consider an asymmetry between the constitutive materials of the two long walls parallel to the radio electric axes. The idea is to recover an asymmetrical distribution of the path energy depending on the direction of arrival of the rays. It is expected that the level coming from the WALL side would be stronger than the level coming from the PARTITION side.

Figure 56 and Figure 57 represent the ray tracing channel obtained in the simulated environment.
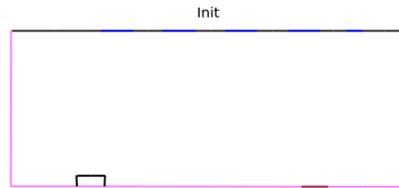
Figure 55 Simplified Layout of environment 1 used in PyLayers "D24.ini"
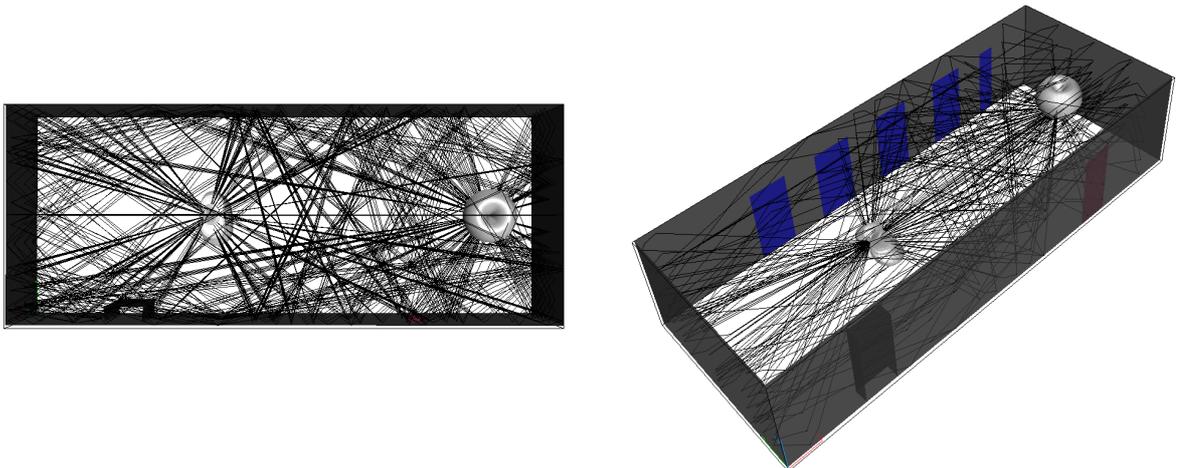
Figure 56 Ray tracing with antenna Φ=0
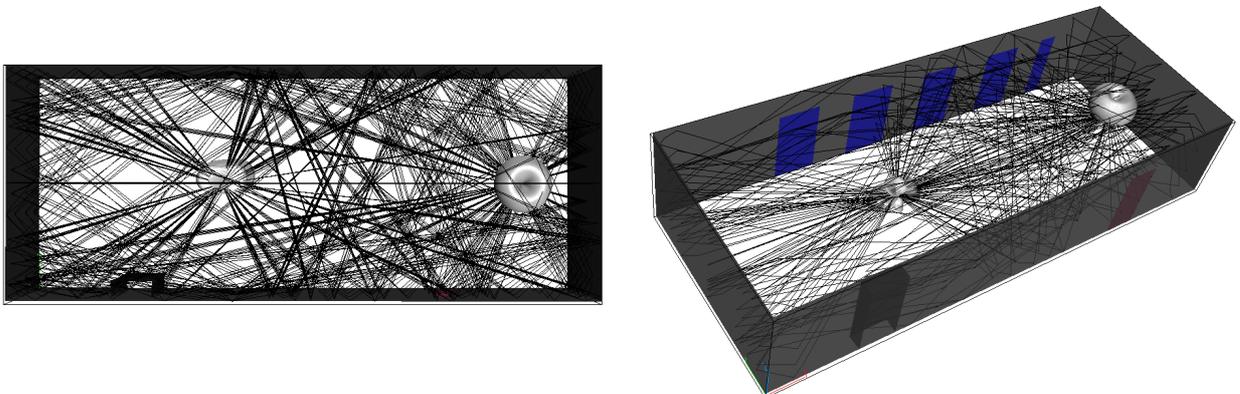
Figure 57 Ray tracing with antenna Φ = 90°

4.2.2   DESCRIPTION OF THE OFF-BODY ANTENNA

The simulation has been performed twice, namely Run1 and Run2, considering different antenna patterns.

In Run1 the off-body antenna was first simulated using a 3rd order polynomial function which mimics roughly the antenna pattern used for the measurements. In a first attempt the antenna pattern was supposed to be frequency independent. In Run2 the 3D simulated realized gain pattern of the wire-patch monopole antenna has been used. In Figure 58 we show the measured realized gain pattern of the wire-patch monopole antenna in the elevation plane [1], and the antenna patterns used in PyLayers Ray tracing. It could be notices that the analytic function which has been used for the pattern in Run1 underestimates the gain for low elevation angles, which could affect the antenna pondering of those rays coming from the ground. The 3D simulated antenna pattern is obviously closer to the measured, presenting a maximum realized gain of around 5dBi, while the gain in the horizontal plane is about 0 dBi, which is slightly higher than the actual gain measured.

The results of both simulations are here presented in order to illustrate the importance of a good representation of the antenna pattern when comes the point of comparison with measurements.

.
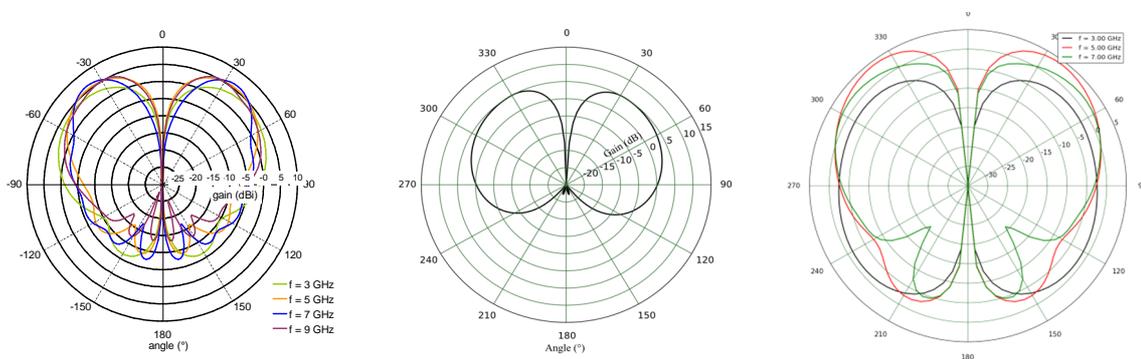
Figure 58 Measured pattern (left) versus simplified function used in PyLayers Ray tracing for Run1 (center) and simulated gain for Run2 (right)

4.2.3   DESCRIPTION OF THE BODY-MOUNTED ANTENNA

The body-worn antenna is a UWB disc planar dipole antenna as described in [1],[3].

In Run1 we considered the measured antenna pattern when the antenna is placed at 30 mm from an arm phantom (see section 2 in [1]). The corresponding gain pattern is presented in Figure 59. In this case the antenna did not correspond to the measured conditions, but it has been used to validate a new developed antenna format in the PyLayers platform.

In order to compare the ray-tracing results to the measured ones, in Run2 we considered the same antenna placed on cylindrical phantom with 30 cm radius and an antenna-body separation of 5 mm, as described in §6.3 of [1]. The results coming from simulation on CST MWS® have been included in PyLayers. The gain patterns in the elevation and azimuth are represented in Figure 60.
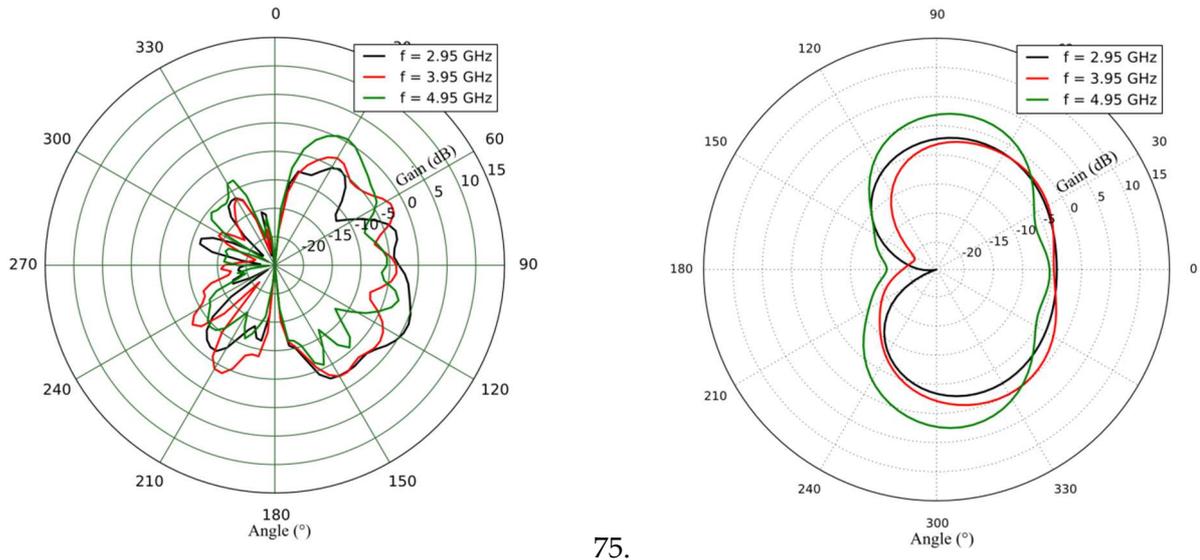
75.

Figure 59 Body-worn antenna used in PyLayers simulation (Run1): elevation (left) and azimuth (right)
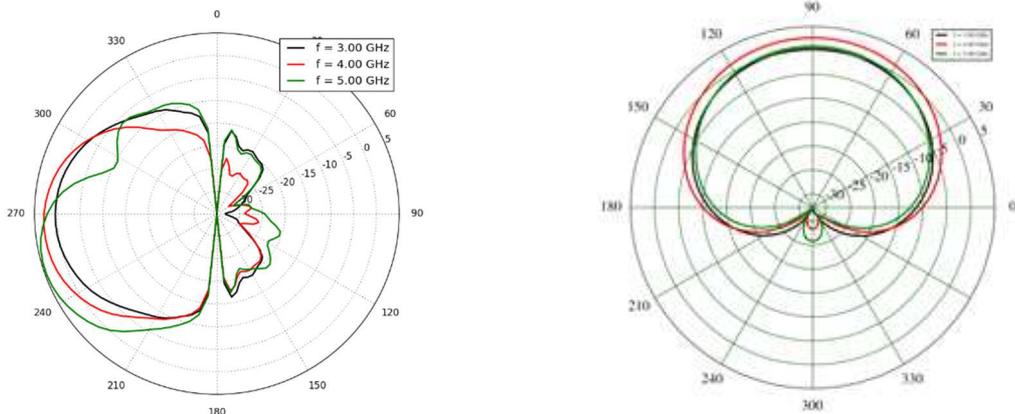
Figure 60 Body-worn antenna used in PyLayers (Run2): elevation (left) and azimuth (right)

4.3. COMPARISON WITH STATISTICAL MODEL

4.3.1   UWB PATH LOSS FROM DETERMINISTIC SIMULATION

As a first step, in this section we evaluate the path loss evolution versus distance d_{off} obtained from the PyLayers ray tracing tool. This comparison aims at validating the deterministic tool and the simulation approach including body-worn antennas, which is going to be further exploited in a more sophisticated scenario involving both body motion kinetics and high level mobility. At this stage it is important to check the tool capability to provide consistent levels with both the choice of antenna and propagation environment. Simulation results are also presented for the two realized sets of simulation, i.e. Run1 and Run2 as described above.

- *Run1 results (Simulation with heuristic antennas, early work)*

Figure 61 ,Figure 62 and Figure 63 illustrate the simulated path loss obtained for 3 different positions of the antenna mounted on body, respectively on torso, shoulder and back.

The main noticeable difference between measured and simulated data concerns the angle rotation value Φ=90° where clearly the simulation overestimates the signal level. This can be clearly explained by considering the gain pattern of Figure 59 which shows that the antenna still captures a significant amount of energy in the simulated channel when rotating the antenna of 90°. The body shadowing effect is very well recovered for the 180 ° value, very much in line with what is expected in the reality.
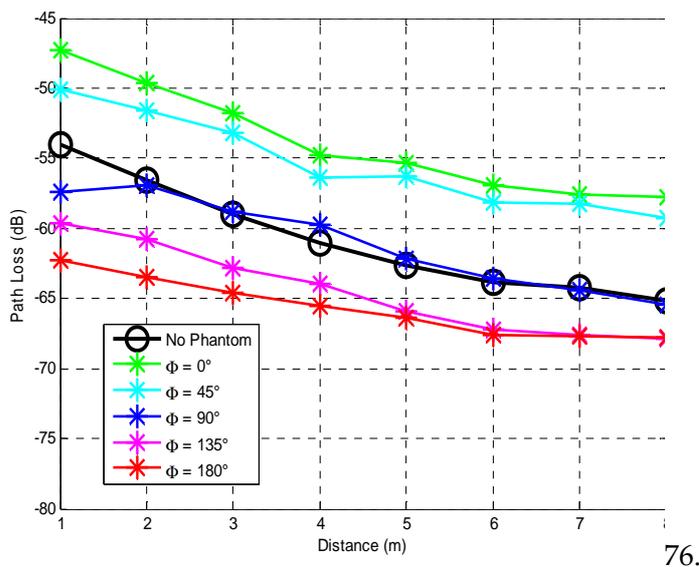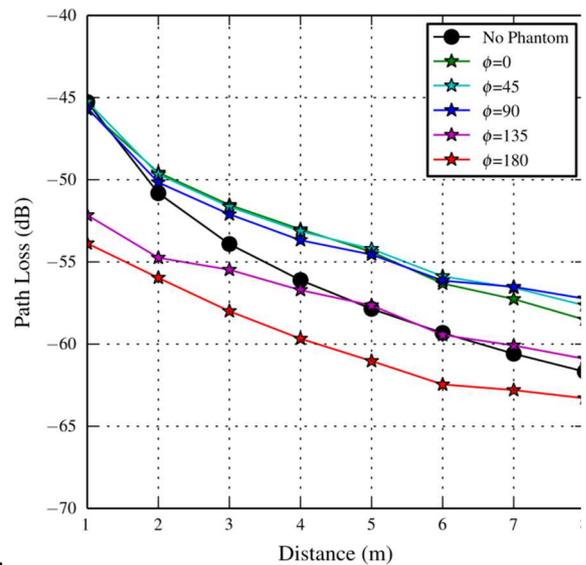
Figure 61 Measured (left) versus simulated Path Loss in Run 1 (right): environment 1, antenna mounted on torso
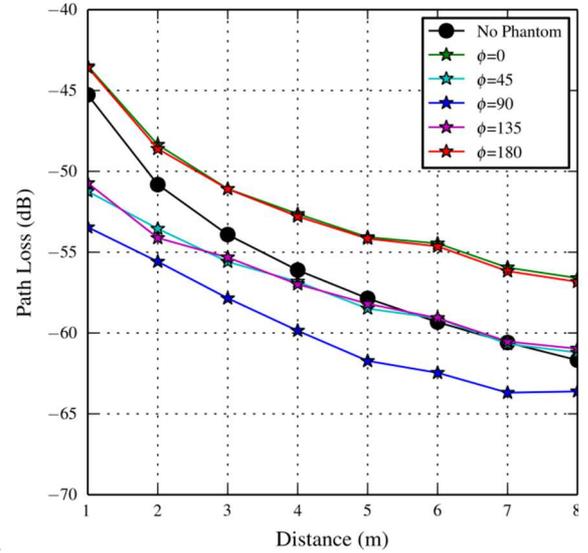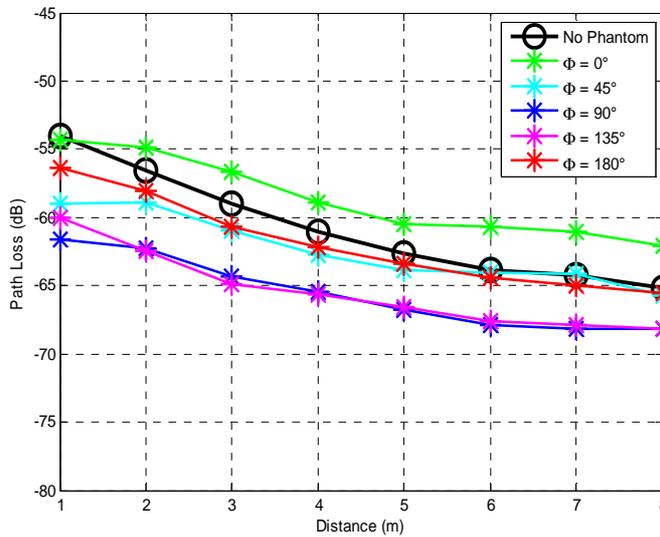
77.

Figure 62 Measured (left) versus simulated Path Loss in Run 1 (right): environment 1, antenna mounted on shoulder
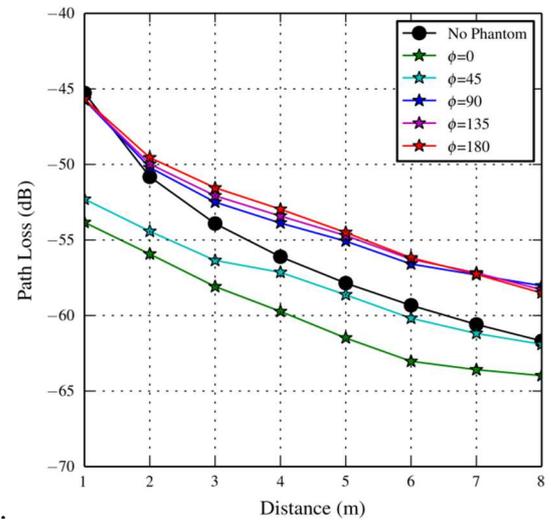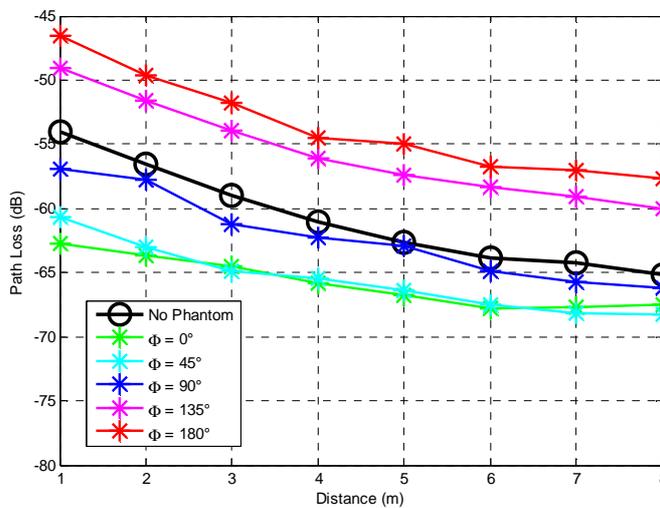
78.

Figure 63 Measured (left) versus simulated Path Loss in Run 1 (right): environment 1, antenna mounted on back

- *Run2 results (Realistic antennas on both sides of the link)*

Figure 64, Figure 65 and Figure 66 illustrate the simulated path loss obtained for 3 different positions of the body mounted antenna, respectively torso, shoulder and back. This is exactly the same situation as for Run1 but considering simulated gain patterns close to the one expected in the real channel measurements. For the 3 scenarios, we have a very good agreement between measurement and simulation is excellent both quantitatively and qualitatively.

It is interesting to notice that the simulation with realistic antennas catches the modification of the path loss exponent in situation of deep occultation exactly, as it was observed in measurements. Indeed at angle values of 180° ,90° and 0° for torso, shoulder and back respectively, the dependency with distance is observed as being almost flat.
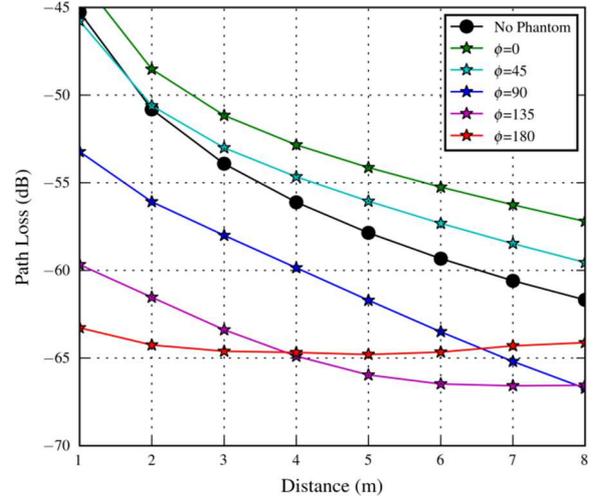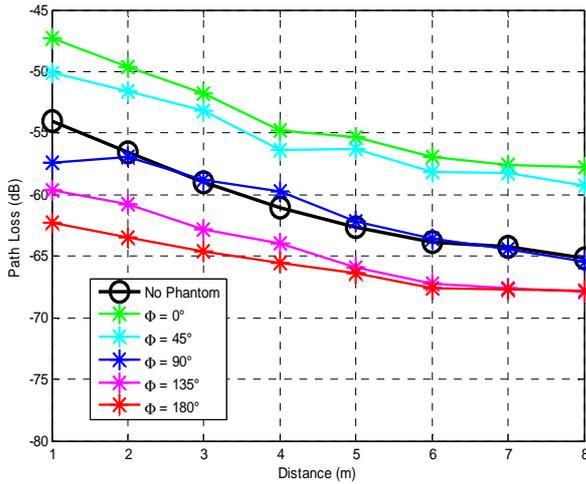
79.

Figure 64 Measured (Left) versus Simulated Path Loss(Right Run 2) (env 1) Rx mounted on torso
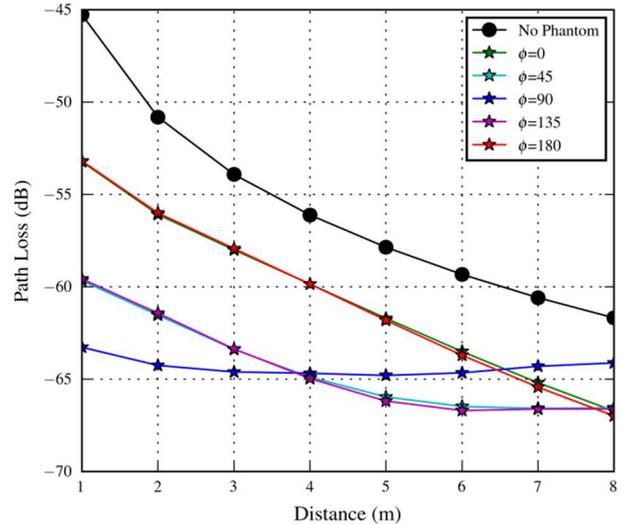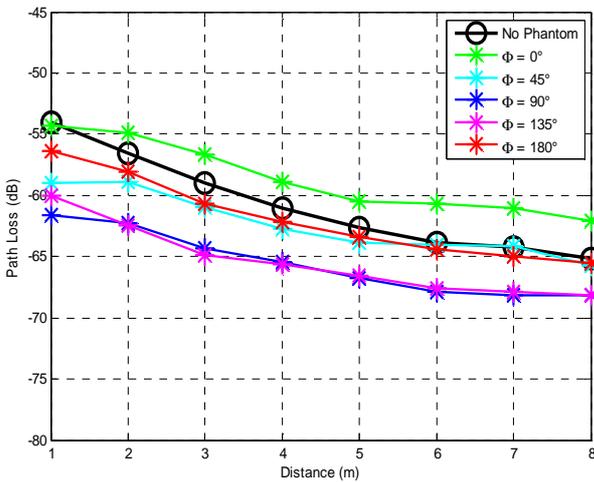
80.

Figure 65 Measured (Left) versus Simulated Path Loss (Right Run 2) mounted on shoulder
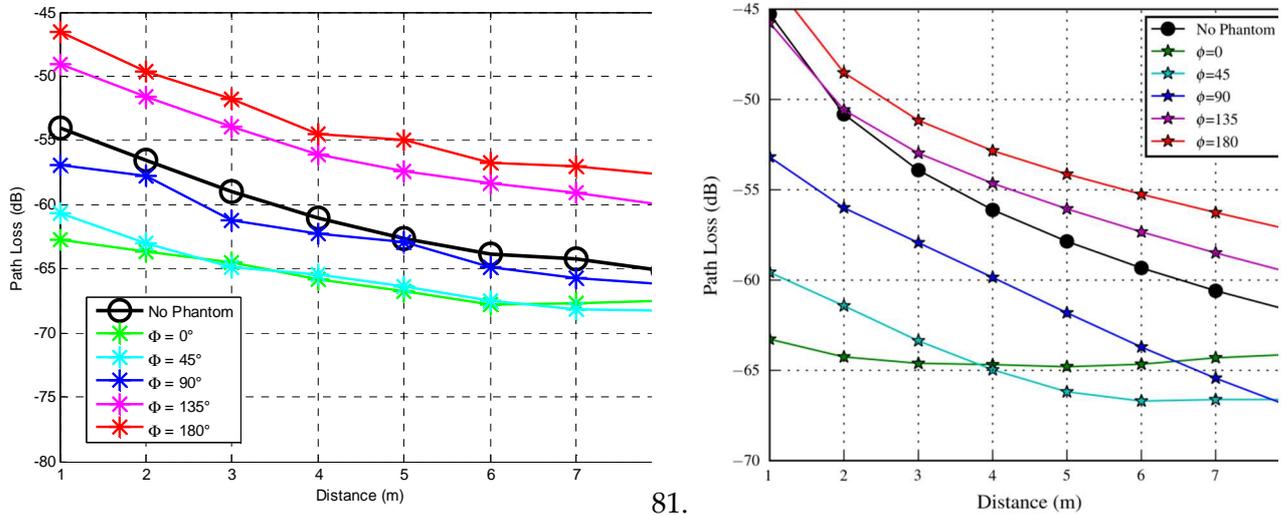
Figure 66 Measured (Left) and Simulated Path Loss (env 1 Run 2) Rx mounted on back

The consequence of this fairly good agreement between measurement and simulation data is very important for further production of simulated results in the CORMORAN scenarios described in D1.1. The significant difference between simulated Run1 and Run2 emphasizes the strong importance of the antenna pattern in shaping the received power.

4.3.1 DETERMINISTIC SIMULATION OF ANGULAR DELAY SPREAD

This section presents a comparison between the results obtained by means of the deterministic tool and those obtained thanks to AoA estimation in real off-body channel measurements. The quantity of interest is the angular delay profile. It has to be underlined that for both simulations runs, the description of the environment is very rough and captures the main room dimensions and the antennas placement according to the description given in Figure 14.

The simulation have been done for two distances (d_{off} = 1m and d_{off} = 8m) in order to allow the comparison with the results obtained from SAGE estimation and presented in section 3. All the antenna positions on the body (Torso, Shoulder and Back) have been evaluated.

In the following, each MPC is represented by a point where the angle represents the simulated AoA in azimuth (body-worn antenna), the distance separating the points from the center of the circle represents the estimated time delays multiplied by the speed of light in free space, and the color is the corresponding MPC power.

Several interesting considerations can be done from the comparison between these preliminary simulations and off-body measurements.

- *Run1 results (Simulation with heuristic antennas, early work)*

First we considered the isolated antenna case were the antenna is not placed on the body. In this case one node is replaced by an ideal isotropic antenna, while an analytical antenna pattern is considered for the off-body node.

The MPC amplitude level is fairly reproduced considering the large indetermination we have on several environment parameters. The observed amplitude level is actually well in line with the observed one from the corresponding measurement data (Figure 67 and Figure 68). This result attests the ability of *PyLayers* to provide the good signal level when considering the proper antenna gain. This achievement is important for further Physical layer abstraction implementation.
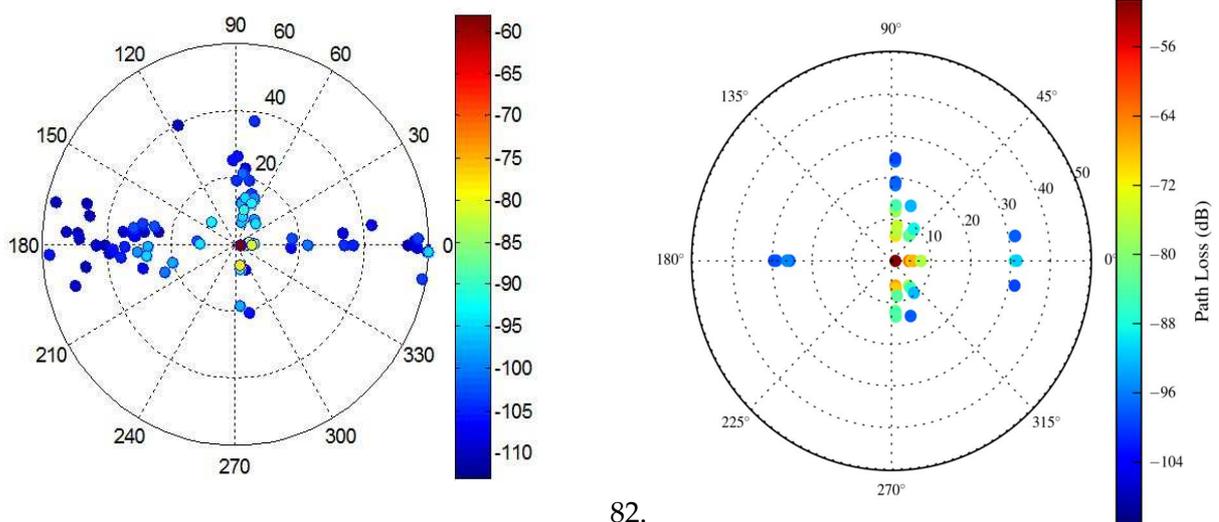
Figure 67 Estimated MPC isolated antenna (d$_{off}$ = 1m): measurements (left) and Ray Tracing Run1 (right)

83.
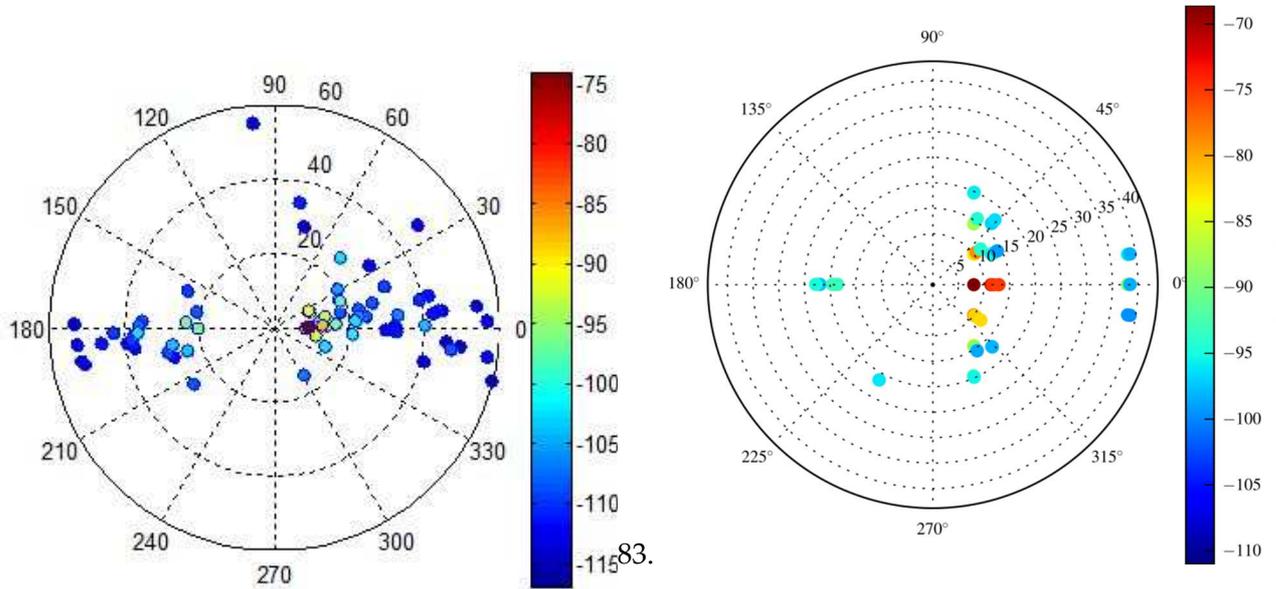
Figure 68 Estimated MPC isolated antenna (d$_{off}$ = 8m): measurements (left) and Ray Tracing Run1 (right)
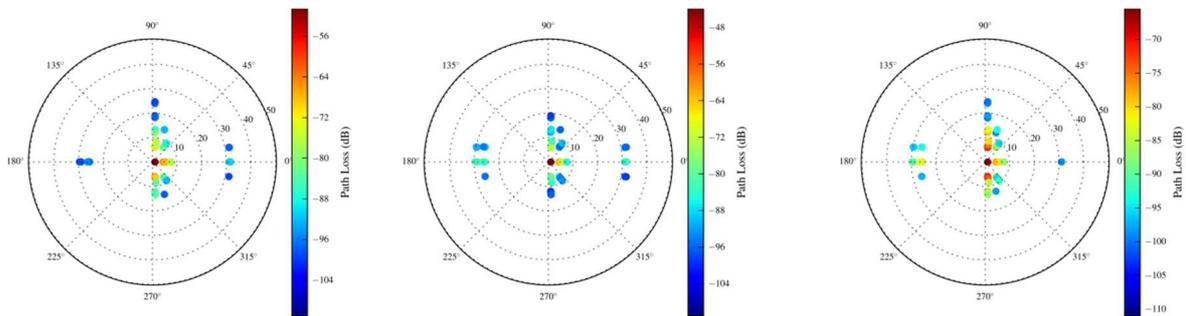
Figure 69 MPC from Ray Tracing Run1: torso (left) , shoulder (center), back (right) at d$_{off}$ =1m
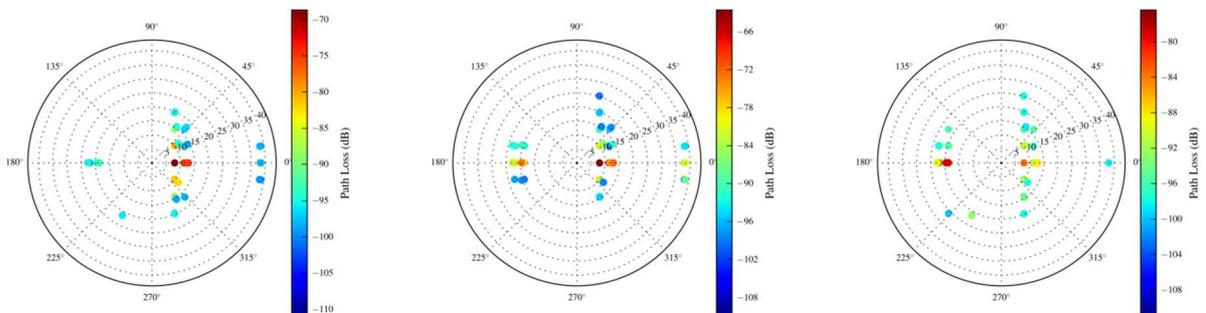
Figure 70 MPC from Ray Tracing Run1: torso (left) , shoulder (center), back (right) at d$_{off}$ =8m

In Figure 69 and Figure 70 we present the results obtained from the first set of simulations, namely Run1, considering a body phantom.
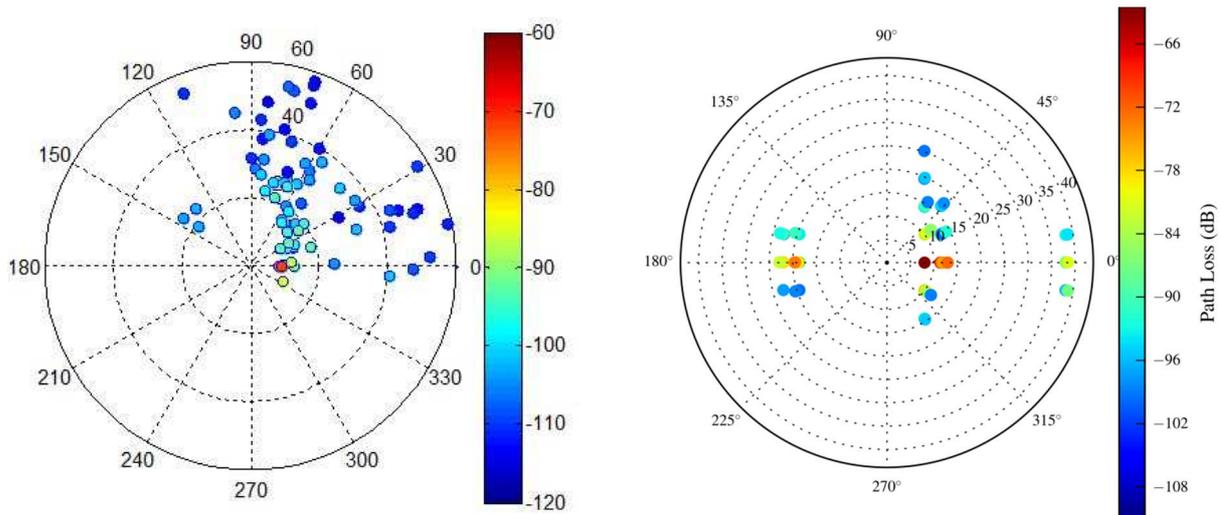
Figure 71 Estimated MPCs from measurements (left) and Ray tracing (right): antenna on shoulder, d$_{off}$ = 8m
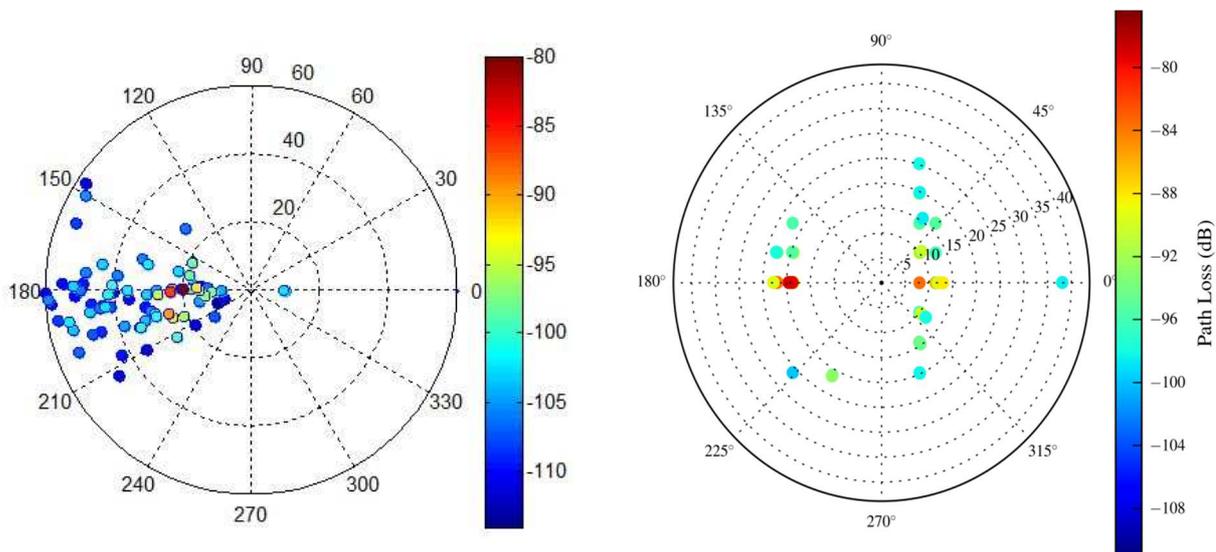
Figure 72 Estimated MPCs from measurements (left) and Ray tracing (right): antenna on back, doff = 8m

Figure 71 and Figure 72 represent the comparison between MPC obtained from ray tracing simulations and the corresponding MPC obtained from the SAGE algorithm. Here we can notice a significant disagreement between the MPCs spatial distribution. Results from measurements find MPCs in a very restricted region of space while the ray tracing do not significantly modify the AoA

distribution. This is mainly due to the body-worn antenna considered. The antenna gain pattern was obtained from measurements considered a small phantom with respect to the reality of channel measurements. As a consequence the angular selectivity of the body-worn antenna is quite different in simulation and measurements, affecting the AoA distribution of the channel.

- *Run 2 (Realistic antennas on both sides of the link)*

In order to fairly compare measurement and simulation, realistic radiation patterns have been included in the *Pylayers* tool.

Figure 73 and Figure 74 represent the situation with no phantom, i.e. isolated antenna. Both amplitude levels and angle distribution are well recovered.
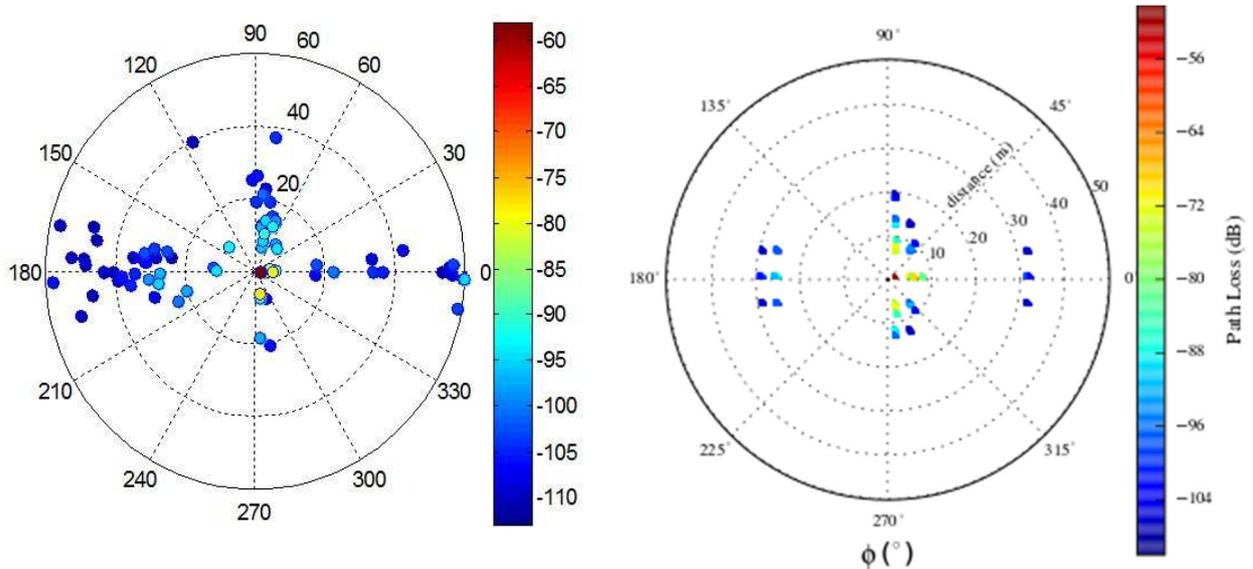
Figure 73 Estimated MPC isolated antenna (d$_{off}$ = 1m): measurements (left) and Ray Tracing Run2 (right)
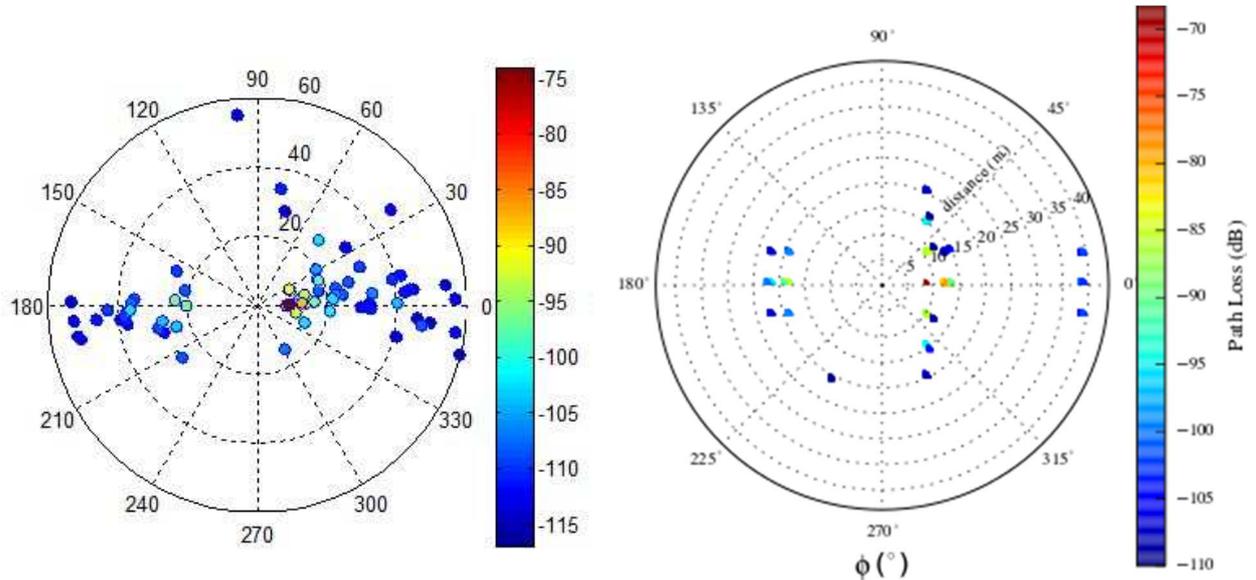
Figure 74 Estimated MPC isolated antenna (d$_{off}$ = 8m): measurements (left) and Ray Tracing Run2 (right)

Figure 75, Figure 76 and Figure 77 illustrate the results for the antenna placed on the torso, shoulder and back respectively, considering d_{off}=8m. The different antenna positions on the body have been obtained by opportunely rotating the antenna pattern of the UWB planar disc dipole on the cylindrical body phantom.

It can be noticed that in Run2 simulations the angular distribution is much more in agreement with measurement. This result highlights the importance of taking into account the proper radiation pattern in the ray-tracing tool in order to effectively reproduce the channel characteristics.
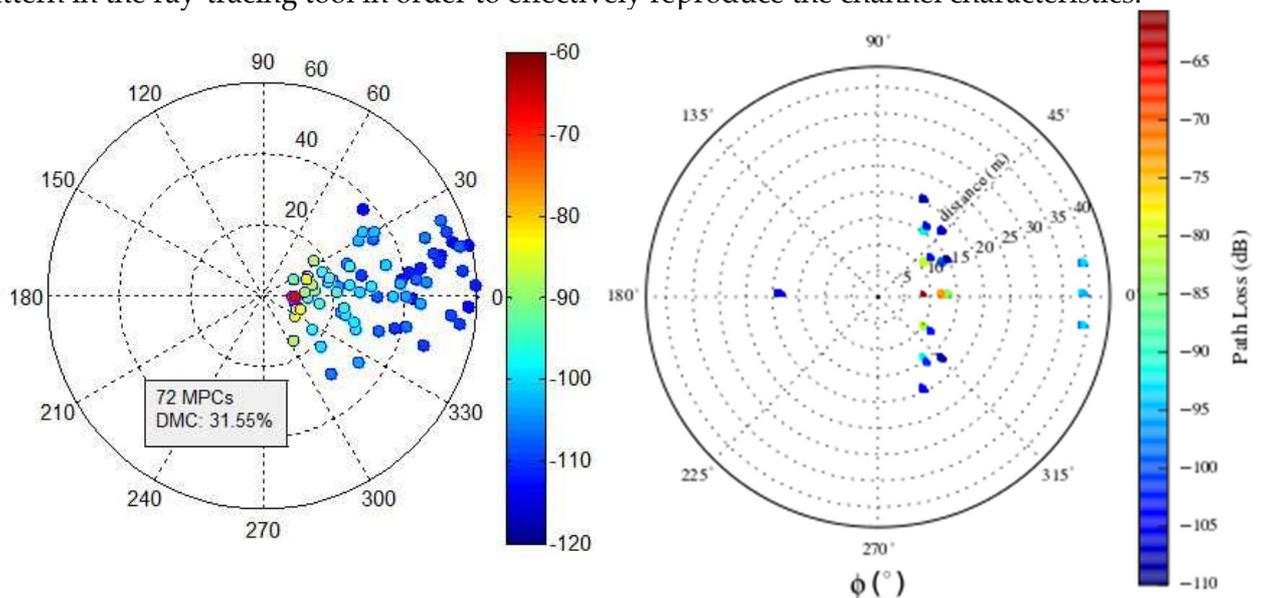
Figure 75 Estimated MPCs from measurements (left) and Ray tracing Run2 (right): antenna on torso, d$_{off}$ = 8m
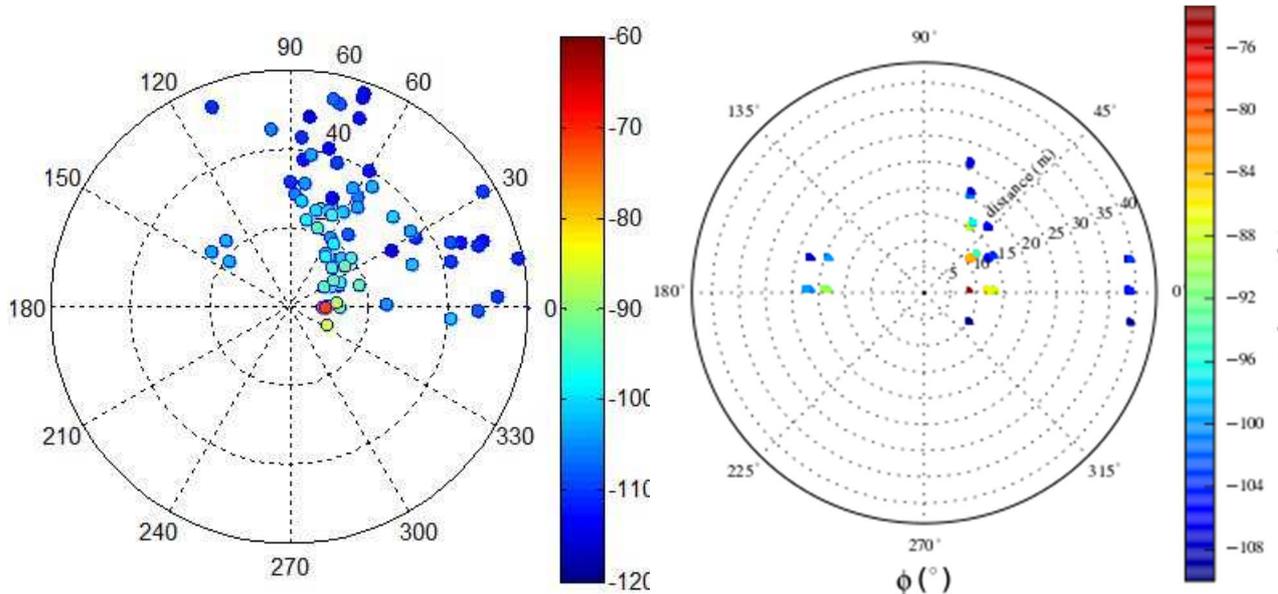
Figure 76 Estimated MPCs from measurements (left) and Ray tracing Run2 (right): antenna on torso, d_{off} = 8m
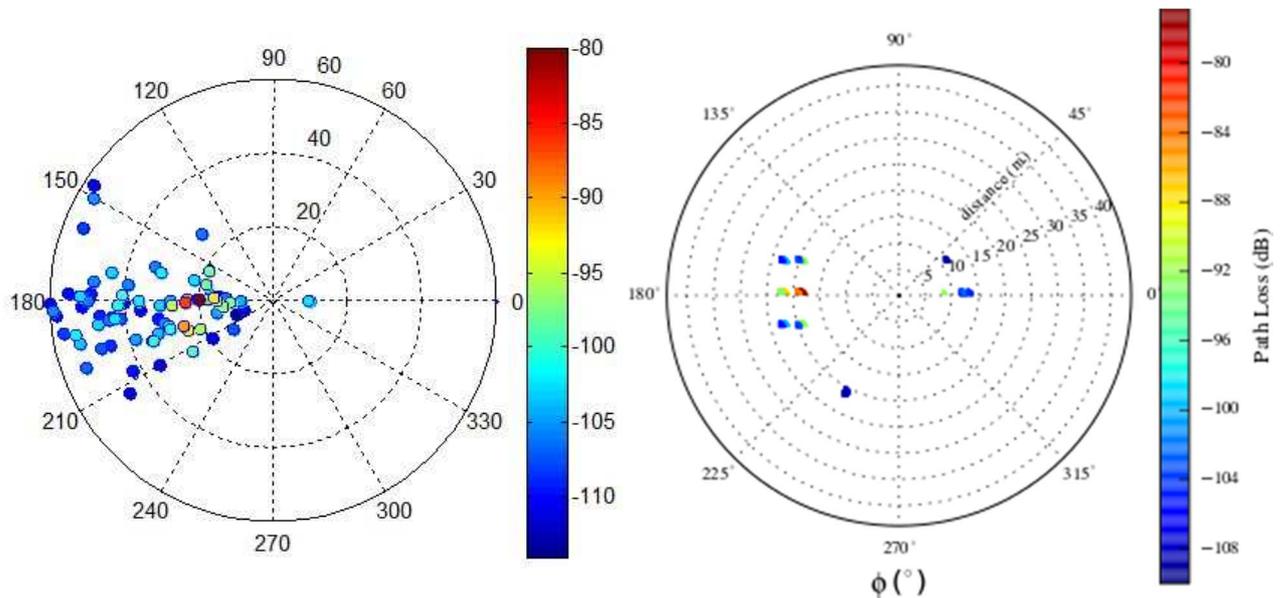
Figure 77 Estimated MPCs from measurements (left) and Ray tracing Run2 (right): antenna on back, d_{off} = 8m

4.4. CONSEQUENCES OF THE COMPARISON MEASUREMENTS-SIMULATION

 At that point of the investigation, the main features of the deterministic ray-tracing tool *PyLayers* has been validated for static scenarios starting from measurements. It has been shown that even

with a simplified environment description and a fairly approximated antenna pattern on the body, the tool is able to retrieve the main channel characteristics. This result open new perspectives in terms of PHY layer simulation (as expected for D2.5), in which different scenarios and antenna orientations could be considered along body movement.

5. BODY-TO-BODY CHANNEL MODELING

5.1. REMIND NB B2B STATISTICAL CHANNEL MODEL

Body to body channel characterization and modeling has been presented in [2]. Starting from indoor real-time measurements at 2.45 GHz, the radio channel was modeled, both in Line-of-Sight (LOS) and Non Line-of-Sight (NLOS) conditions, through a mean channel gain component plus a fading contribution, the latter arising from the body movements. The body shadowing effect was also evaluated considering the orientation of one human body with respect to another one. Two different antennas were employed in the measurements, to assess their impact on the radio channel characteristics [31]. Models are reported in §4.1.3, [2].

5.2. COOPERATIVE WBAN COMMUNICATION MODELING

5.2.1 MEASUREMENT SCENARIOS DESCRIPTION

In addition to the previous measurement campaigns of Body-to-Body channel, new WBAN measurements had been performed at CEA-Leti in cooperative communication contexts in the sense that On/Off-Body and Body-to-Body channels were measured simultaneously. For that purpose, we used the phantom, an AP (a mast with an antenna at its top) and human subjects. In total, two human subjects have been involved in this measurement campaign which has been carried out in the environment 2.

For each measurement acquisition, one human subject, the phantom and the AP were aligned as showed in Figure 78. The human subject was always located between the external node and the phantom. The antennas carried by the human subjects and the phantom were Thomson UWB dipoles. That used for the external gateway was a TLM. Two antennas were located on the human subject, one on the torso and the other one on the back. One antenna was located on the torso of the phantom. For convenience, we number the so-obtained nodes from 1 to 4 as illustrated in Figure 79. Strictly all the radio links (On/Off/Body-to-body) were simultaneously measured by a VNA whatever the mobility scenario was.

Measurements had been performed in a dynamic context, i.e. the human subject walked, from the front of the AP to the front of the phantom. Due to the frequency sweep duration of the VNA, it was not possible to perform measurements on a wide frequency band. Thus, the measurements have been performed at 4 GHz which corresponds to the center frequency of the UWB lower band. The analysis of these measurements at 4 GHz, which will be presented in D2.4, will be extendable to the entire UWB lower band. Indeed, in the next section, we show that the analysis and observations made at 2.4 GHz are the same at 4.2 GHz.

The dynamic measurements have been carried out for 5 phantom orientations: from 0° to 180° with a step equal to 45°. For each phantom orientation, 5 measurement acquisitions corresponding to 5 walk cycles were performed by human subject. All the walk cycles corresponded to the same

straight line trajectory. The departure of the trajectory corresponded to the case d_{B2B} = 7m, and the arrival to d_{B2B} = 1m. Therefore, one cycle of walk corresponded to a walk of 6m.

Figure 78 : Photography of a WBAN measurement in a cooperative scenario
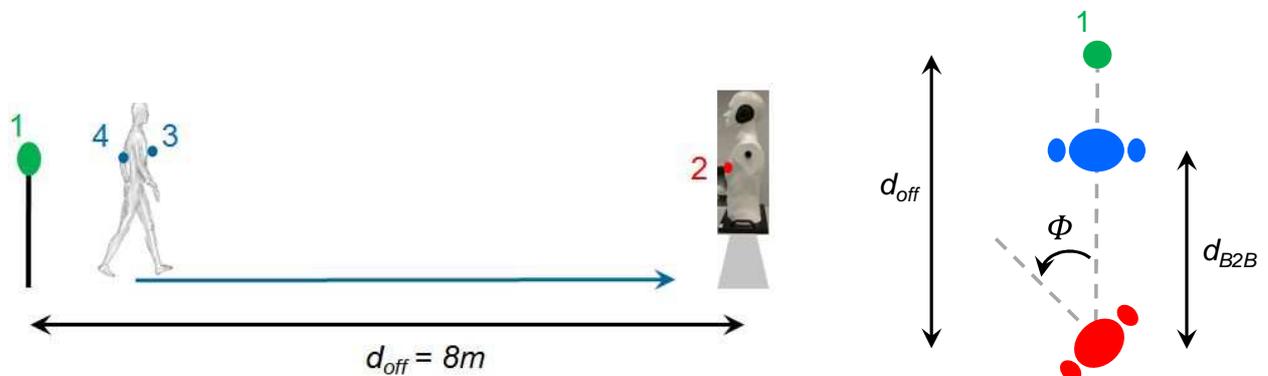
Figure 79 : Dynamic measurement campaign illustration in a cooperative scenario

5.2.2   SPACE-TIME CORRELATION ANALYSIS

Before taking a look on the measurements, for a phantom orientation Φ° equal to 0°, we obviously expect that the power of :

- the Off-Body link (4-1) will decrease
- and that of the Body-to-Body link (4-2) will increase in time since during the measurement acquisitions, the subject was walking away from the AP and towards the phantom. For this reason, we first analyze these radio links.

Similarly to the analysis carried out in section 2.2 for dynamic On-Body measurements, we propose to extract the slow fading components. Figure 80 and Figure 81 give the channel measurement and

the extracted slow fading component for the links (4-1) and (3-2) for both subjects, for a phantom orientation equal to 0° and 180° respectively. The time window width for the extraction of the slow fading components is equal to 720 ms. As expected, the power of the Off-Body link (4-1) decreases while that of the Body-to-Body link (3-2) increases.
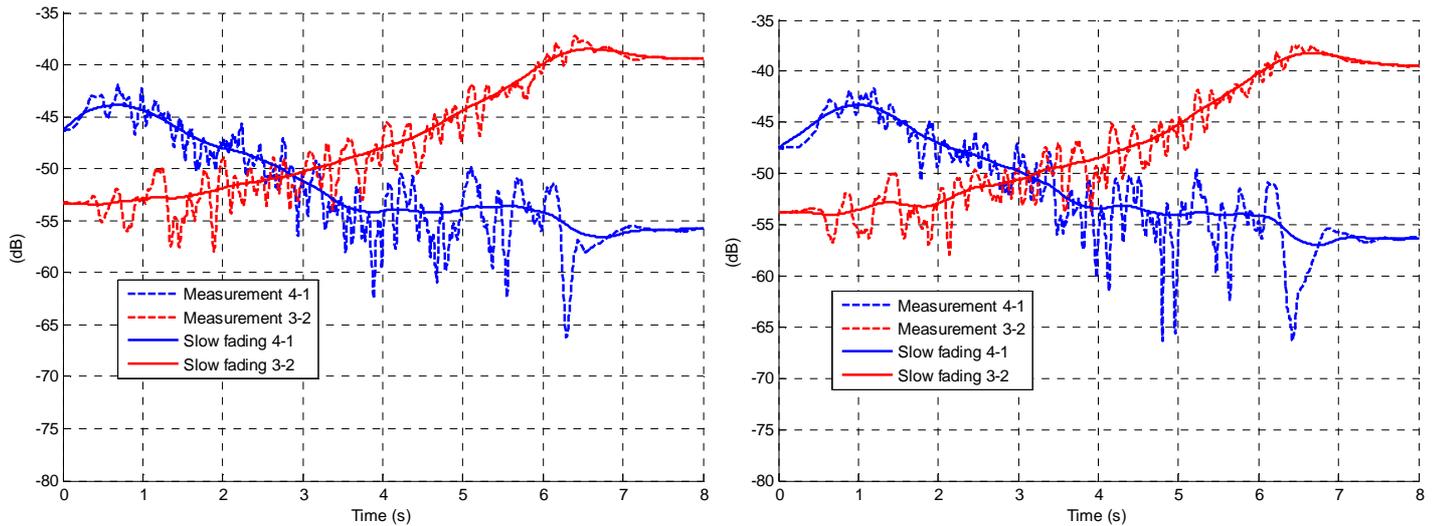
Figure 80 : Measured signal and extracted slow fading component – subject 1 (left) and subject 2 (right) – Φ = 0° - links (4-1) and (3-2) – Δt = 720 ms
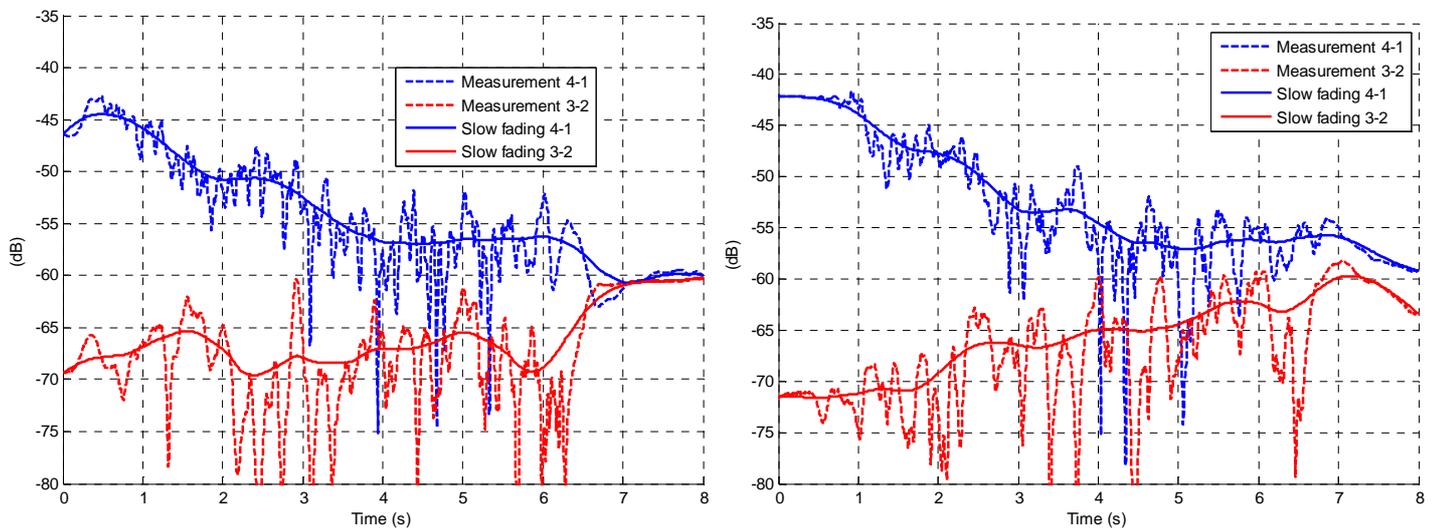
Figure 81 : Measured signal and extracted slow fading component – subject 1 (left) and subject 2 (right) – Φ = 180° - links (4-1) and (3-2) - Δt = 720 ms

We give in Table 22 the space-time correlation values measured between the measurements and the slow fading components of the link (4-1) and the link (3-2) averaged over the 5 cycles of walk. We note that the links are anti-correlated in most of the scenarios. The absolute correlation values are higher when they are computed from the slow fading components than the measurements.

This can be explained by the fact the measurements contain a fast fading component which, contrary to the slow fading component, is independent between the different links.

Expected for subject 1 for which the correlation is significantly lower for a phantom orientation equal to 180°, the phantom orientation do not seem to have any influence on the correlation properties. Indeed, by comparing Figure 80 and Figure 81, we note that the phantom orientation has influences on the channel power of link (3-2) but not on its variation in time.

$\rho_{(4-1),(3-2)}$	84. Subject 1 Slow fading	85. Subject 1 Measurement	86. Subject 2 Slow fading	87. Subject 2 Measurement
$\Phi = 0°$	-0.85	-0.67	-0.79	-0.59
$\Phi = 45°$	-0.90	-0.68	-0.89	-0.67
$\Phi = 90°$	-0.84	-0.38	-0.82	-0.40
$\Phi = 135°$	-0.79	-0.44	-0.68	-0.07
$\Phi = 180°$	-0.23	0.00	-0.87	-0.36

Table 22 : Space-Time correlation values between link (4-1) and link (3-2) – measurements and slow fading components

By investigating the space-time correlation between the Off-Body link (3-1) and the Body-to-Body link (4-2), we remarked that the obtained correlation values were pretty random. Indeed, by observing the measurements and the slow fading curves, we do not note any general trend as showed in Figure 82 and Figure 83. It could be explained by the fact that both links are in NLOS conditions, whatever if the phantom orientation. Therefore, as demonstrated in [16] and [31], the channel power links do not depend to the distances.
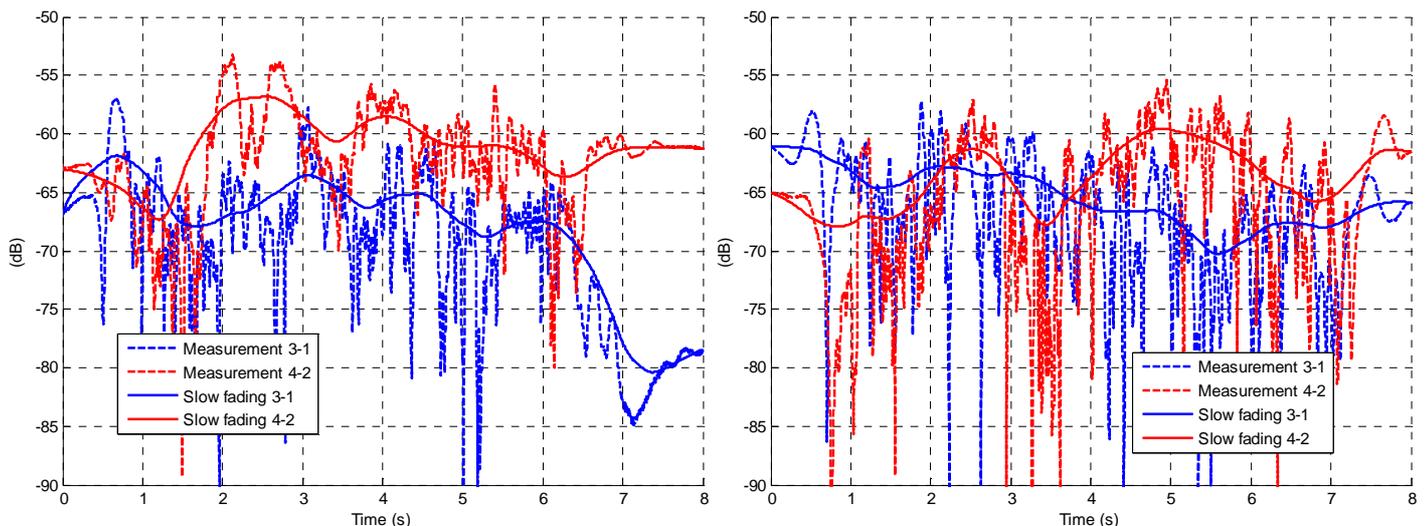
Figure 82 : Measured signal and extracted slow fading component – subject 1 (left) and subject 2 (right) – $\Phi = 0°$ - links (3-1) and (4-2) – $\Delta t = 720$ ms
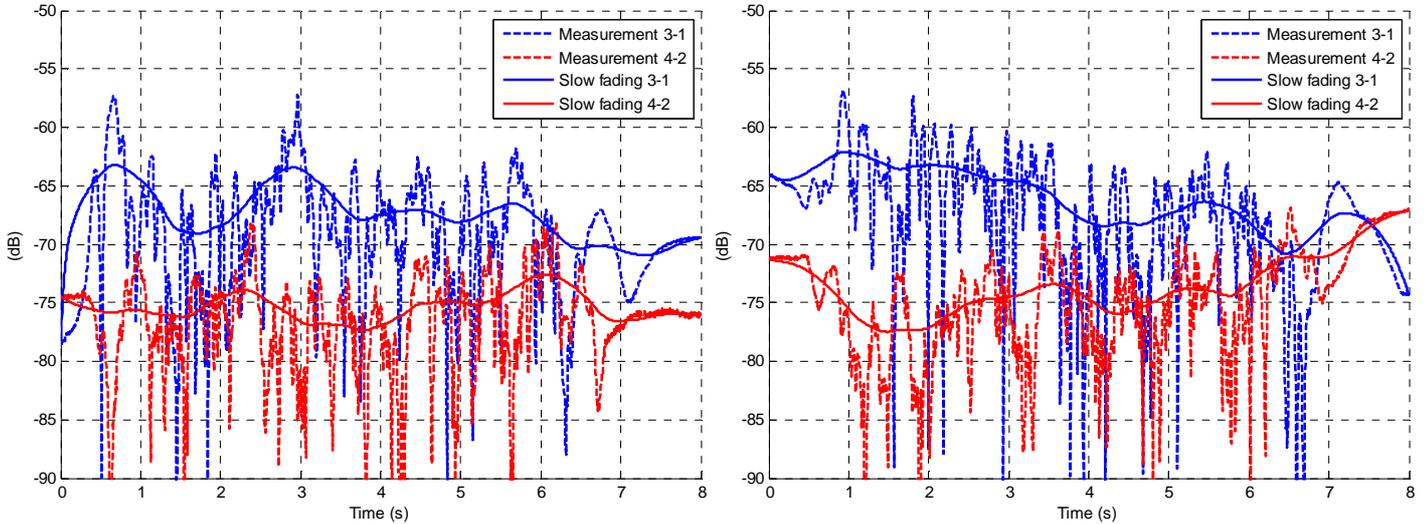
Figure 83 : Measured signal and extracted slow fading component – subject 1 (left) and subject 2 (right) – Φ = 0° - links (3-1) and (4-2) – $\Delta t = 720$ ms

5.3. CONCLUSION AND INPUTS FOR THE OTHER TASKS

In this section, we remind the narrow band Body-to-Body channel models proposed in D2.2. They are exploitable for communication systems performance. An analysis of dynamic WBAN measurements in cooperative context has been carried out. Space-time correlation properties have been analyzed between an Off-Body link and a Body-to-Body link. However, no correlation property has been observed for the other links.

6. INPUTS FOR THE PHYSICAL SIMULATOR

In the previous sections, we presented the channel models for different scenarios defined in CORMORAN. One of the mains objectives of the project is to create a simulator capable to test different location algorithms and protocols for cooperative BANs. To this purpose, it is important to identify and understand the key-blocks in the simulation framework of the radio transmission chain and make the relation with the channel models studied here. Thus, it is suitable to define the proper radio metrics (such as the SNR, delay spread, PDP, CIR, BER or Ranging Error) at the abstraction of the PHY Layer for the simulation of upper layers.

One possible implementation could make use of the WSNET framework. From one side, WSNET will focus on simulating the upper layers to support the applications defined for CORMORAN and on the other side, PyLayers will focus on the abstraction of the antennas, interferences and impulse response channel for the different BAN scenario. It has to be considered that a full simulation of a PHY layer may slow down the simulation in WSNET. In fact, WSNET was conceived to simulate networks at packet level which makes a quick simulation, while, if we implement the simulation at the bit level by creating the whole transmission chain, this will increase the time of simulation. Thus an abstraction of the PHY layer is needed.

Here we argue about a possible implementation of a Physical Layer Simulator for a typical UWB system of interest for CORMORAN.

6.1. TYPICAL UWB TRANSMISSION SYSTEM

6.1.1 RELATED WORKS

For better understanding, we will explain some transmission systems studied for UWB on the last years. Firstly, the study carried out in [32] proposes a chain of transmission UWB PHY with OOK modulation in multi-bands (MB-OOK), using a non-coherent reception. The proposed solution is suitable for systems with high bandwidth, short range and low power consumption such as it was defined in the IEEE 802.15.3a standard. In the same work, they studied the coexistence with other transmission systems with high synchronization dependency. For this, they used the bit error probability (BER) as a comparison metric depending on the energy per bit transmitted. Thus, it is shown that the MB-OOK benefits from a significant bit energy and therefore greater relative to MB-OFDM systems. Moreover, it is also proposed an asynchronous and quadratic approach for the receiver using the results from [33]. Therefore, the performance analysis is conducted from the viewpoint of decision theory which leads to a hypothesis test by thresholding to calculate the BER depending on the energy reception of a pulse and frequency band of transmission.

This last work has been focused on the use of non-coherent receivers in high data rates. In [34] the authors compared three different receivers in AWGN and multipath channel at low data rate. For that, they analyze the performance of stored reference (SR), transmitted reference (TR), and energy detector (ED) receivers in 802.15.4a CM1 channels. First, they show that in the case of imperfect channel estimation, SR energy collection will have important degradation, while ED and TR are

not affected. However, in higher sampling rates SR achieves better synchronization and energy detector, while TR and ED have few improvements. Moreover, they analyze the BER of different modulations (OOK, PPM and DPSK) with each receiver. Thus, SR seems to be better at low SNR and its performance does not change for the three modulations. Finally, ED shows a more favorable BER than TR for OOK and PPM modulations.

In [35], a complete PHY Layer was proposed for the standard IEEE 802.15.4a, therefore, this study was able to highlight some important steps to consider a PHY UWB layer dedicated for sensor networks. Thus, the study was oriented towards low rate and short range applications for the future connected objects. For that, they proposed a non-coherent approach which considerably reduces the PHY layer complexity and cost. Thus, the ED and the variable threshold comparator proposed in the receiver shows that the amplitude of the signal that is not important for UWB radio systems, but the absence or presence of a pulse at a given instant. Furthermore, rather decision theory is also considered to know if a frame is received successfully by using the Constant False Alarm Rate (CFAR) approach. From this work, [36] proposed a PHY Layer more focused on BAN using a coherent and a non-coherent receiver with PPM-BPSK modulation and a 2-bits coded pulse for a data rate varying from 1.42 to 31.24 Mbps. They showed that the coherent receiver stays optimal for an AWGN channel and sub-optimal for fading channels. In the other side, the non-coherent approach loses in performance by 5.17 dB in comparison with the coherent receiver. Moreover, the two receivers were also tested in the BAN context for CM3 and CM4 channels to find the minimum SNR and gain to support the chosen QoS (PER = 10^{-4}). However, the results showed that the gains founded are not enough to achieve the desired performance. In return, they proposed some axes to be explored which were taken in the work of the BANET project and contribute in the definition of the IEEE 802.15.6 standard.

In the same context, [37],[38] proposed different energy detector receivers for low cost and low complexity systems. Thus, they show that this kind of receiver can be applied in the case of low rate and low cost applications. As highlighted in [39], we can observe an overview of non-coherent UWB design, including practical implementation aspects, tradeoffs and system processing schemes. From this work, they showed that non coherent receivers lose 5 dB or more with respect to optimal coherent receivers. However, they are less complex and less vulnerable to time-variant multipath effects, phase jitter, synchronization offsets and incomplete energy capture.

Moreover, [40] also proposed a non-coherent receiver with a multipath fusion decision by calculating the sum, weighted by their reliability. The results indicate that this receiver is robust and capable of providing better performance than that of a conventional non-coherent receiver and near optimal. For this they proposed to exploit the high resolution of the receiver to reduce the impact of paths interfered by marginalizing their contribution to the recombination of decisions. This technique requires measuring the conditional probability of error interfered paths, through an observation of the received signal. The simulation show that its performance is quite acceptable, for an interferer more powerful by 10 dB than the useful signal; it is observed a degradation of 1

dB compared to the single-user case. Therefore, this work contributes to demonstrate that UWB link can coexist with one or more interfering with the only condition that the receivers may incorporate a policy of interference rejection. This last point about multi-path interference should be considered as second goal when implementing the PHY layer abstraction for WSNET.

Finally, [41]-[44] show some last works on the ED receivers related in the BAN context using the standards IEEE 802.15.4a and IEEE 802.15.6. Their contribution remains in the optimization of integration interval and the energy threshold for the decision at the receiver.

6.1.2   PHY LAYER INPUTS

From these works, we can sum up that the non-coherent receiver is and keeps a good tradeoff between complexity and performance that could be considered for further studies in WP3. To this purpose, one solution could be to implement a full PHY Layer for the transceiver and receiver. To illustrate this solution, Figure 75 depicts the PHY layer transmission chain in four blocks for the transceiver and receiver. At the transceiver chain, the first one corresponds to the raw data processing, the MPDU created by the MAC layer is coded through BCH encoder to improve the robustness and create the PSDU. Then, the PHR frame is coded by a short BCH code to obtain the PHR that will be appended to the PSDU.
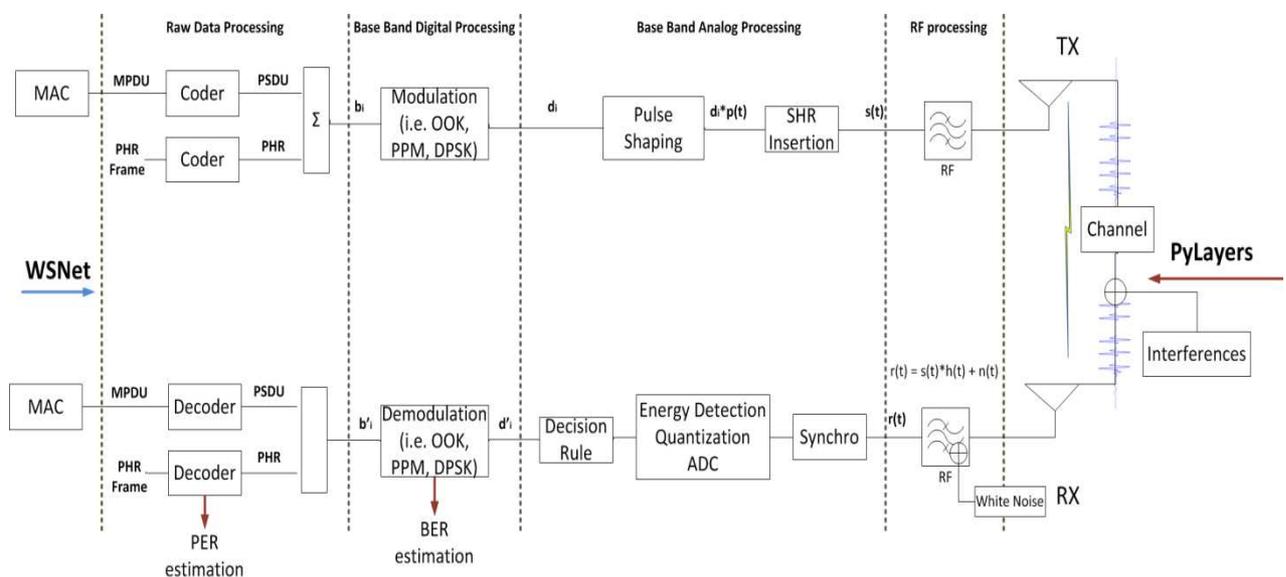
Figure 84 : PHY Layer Transmission System

Therefore, the first block will give a train of information bits (b_i) to the next bloc which is the responsible for the base band digital processing. This block gives a modulated signal (d_i) according to the standard used (e.g. OOK, DPSK) and the UWB symbol structure explained in [45]. It is also

considered the scrambling sequence and the time hopping sequence generation which allows the coexistence of BANs as explained in [45].

Then, the third block is the responsible of the pulse shape ($d_i * p(t)$). In the standard [45], there are three pulse shapes (short, chirp and chaotic) proposed for the IR-UWB and two pulse waveforms (single and burst). The choice is done by implementers, however, the pulse shall respect regulation spectral mask defined in the standard, including the pulse waveform duration, the PRF and the peak PRF (Pulse Repetition Frequency). And after that the SHR is appended to send the IR-UWB signal $s(t)$.

The last block handles the RF processing and transmission to the channel according to the UWB bands frequency allowed. This block has been already implemented in PyLayers but still there are some abstractions to be done for the channel simulation, such as the interference modeling.

At the receiver chain, we can apply the inverted sequence of the transceiver, starting with the RF processing block by translating the received signal into base band. This signal includes the white noise $n(t)$ and the channel impulse response (CIR), $r(t) = s(t) * h(t) + n(t)$.

After that, the signal can be decoded and estimated by different kinds of reception techniques, e.g. non-coherent, coherent or differential. The chosen technique will depend on the nature of the channel and complexity we want to implement at the receiver. As described before, the non-coherent reception is proposed to simplify the complexity. It can work with or without a RAKE technique for multi-path. However, the robustness in this technique depends on the decision rule which detects the reception of a pulse [39]. Thus, it is possible to define the Impulse Error Rate (IER) of estimated symbols (d'_i) and send it to the next block. Then, the symbols are demodulated by the same technique used in the transceiver. Therefore, it is possible to estimate the transmitted bits ($d = b_{0i}$), but also calculate the Bit Error Rate (BER). Then, the last block decodes the message to recover the MPDU and calculate the Packet Error Rate.

The complexity of this solution is the calculation to create a complete trans-mission chain forcing WSNET to take more time for simulations. But also the synchronization needed with Pylayers at the impulse level to get the CIR, which could be the only input needed to have a simulation for upper layers. In fact, if we create a reception model that could calculate the PER depending only on the CIR at a specific moment, the complexity of the PHY Layer will be reduced. In D2.5 we will explore more the pros and cons of this last solution.

7. CONCLUSIONS

This deliverable presents the main results of channel modeling activities carried out in the framework of the task T2.

Given the objectives of the CORMORAN project who aims the exploitation of different WBAN links for cooperative localization and navigation purposes, different WBAN scenarios have been investigated, resulting into a variety of models for on-body, off-body and body-to-body links.

One of the main features of the WBAN channels is their dependence on the antenna characteristics on the body.

First the effect of the body on antenna radiation properties have been investigated and modeled in D2.1. The main result of D2.1 is a compact representation of the antenna pattern on the body that can be exploited in deterministic tools. Secondly the effect of the antenna on channel characteristics has been modeled. The results of previous measurements campaigns and models carried out by CORMORAN partners have been presented in D2.2 together with an extensive State-of-the-Art.

To exploit cooperation approaches specific channel measurements have been carried out in the scope of CORMORAN and reported in D2.2 and D2.3. These measurements have been here exploited together with measurements provided by an external partner of CORMORAN, in order to model the space-time correlation in on-body channel. It has been proven that periodic and regular movement yield to correlation patterns on some links that could be exploited for cooperative approaches. Nevertheless when the user is set free to move, without constraints on the walking path, the correlation properties could change along the observation time. This results into a non-wide-sense stationary channel, whose correlation characteristics have been modeled.

In addition the correlation between links of different nature (on-body, off-body and body-to-body) has been modeled following a reference scenario as described in D1.1.

Focusing on the UWB off-body channel, an extensive measurement campaign has been carried out in indoor environment. Measurements have been carried out in order to compare the channel characteristics when considering an antenna isolated or attached to a body, i.e. a human phantom in measurements. Three different on-body positions (torso, shoulder and back), and distance from 1 to 8 meters have been investigated according to the scenarios described in D1.1. The antennas employed in channel measurements, have been previously characterized in D2.1.

Thanks to a UWB implementation of the SAGE algorithm for Angle of Arrival estimation, and K-means algorithm for cluster identification a full statistic channel model has been proposed for these scenarios.

These results have been used to validate the use of a ray-tracing tool, namely *PyLayers*, for off-body communication. It has been proven that even with a simplified description of the environment the tool is able to provide good accuracy of the channel characteristics. By combining the results of ray-tracing tool together with the model of the antenna on the body, it is possible to retrieve the off-body channel characteristic with a good level of approximation of multipath components' amplitudes, delays and angles of arrival.

This result opens new perspectives in terms of channel modeling allowing the description of different on-body antenna positions and environments in the Physical simulator, which have not been necessary addressed by measurement campaigns. In order to properly take into account the body kinetics, the antenna orientation change along movements is being modeled in CORMORAN. This work, being part of the Physical emulator development, will allow the combination of deterministic and statistic empirical channel models to evaluate cooperative approaches in WBANs and design and evaluate upper layers protocols.

8. REFERENCES

[1] CORMORAN Deliverable D2.1 – "On-Body Antennas Characterization & Exploitable Radiation Properties", Meriem Mhedhbi, Stéphane Avrillon, Bernard Uguen, Melsuine Pigeon, Raffaele D'Errico, Pierre Pasquero

[2] CORMORAN Deliverable D2.2 –" 1st Channel Measurement campaign and identification of relevant radio models and parameters", Oudomsack Pierre Pasquero, Raffaele d'Errico, Meriem Mhedhbi, Bernard Uguen

[3] CORMORAN Deliverable D2.3 – "Final Channel Measurement Campaign", Oudomsack Pierre Pasquero, Raffaele D'Errico, Bernard Uguen, Stéphane Avrillon, Meriem Mhedhbi, Paul Ferrand, Arturo Mauricio, Claire Goursaud, Jean-Marie Gorce, Jimenez Guizar

[4] R. D'Errico and L. Ouvry, "Time-variant BAN channel characterization", in *Proc. of IEEE 20th International Symposium on Personal, Indoor and Mobile Radio Communications* (PIMRC 2009), Tokyo, Japan, Sept. 2009, pp. 732-736

[5] R. D'Errico and L. Ouvry "Doppler Characteristics and Correlation Proprieties of On-Body Channels", the 5th European Conference on Antennas and Propagation (EuCAP 2011), Rome, Italy, 11-15 April 2011

[6] R. Rosini, R. D'Errico, "Comparing On-Body Dynamic Channels for Two Antenna Designs", LAPC 12 Loughborough UK, November 2012

[7] R. D'Errico and L. Ouvry, "Delay Dispersion of the On-Body Dynamic Channel", The Third European Conference on Antennas and Propagation (EUCAP 2010), April 2010, Barcelona

[8] S. van Roy, F. Quitin, L. Liu, C. Oestges, F. Horlin, J. Dricot and P. de Doncker, "Dynamic channel modeling for multi-sensor body area network", *Antennas and Propagation, IEEE Transactions on*, vol. 61, no. 4, pp. 2200-2208, 2013

[9] M. Lauzier, P. Ferrand, A. Fraboulet, H. Parvery and JM Gorce, "Full Mesh Channel Measurements on Body Area Networks under Walking Scenarios", in *Proc. In IEEE Antennas and Propagation (EuCAP),* 2013 7th European Conference on, 2013

[10] "HiKoB FOX sensor," http://www.hikob.com/hikob-fox, 2012

[11] R. I. Jennrich, "An asymptotic χ² test for the equality of two correlation matrices," *Journal of the American Statistical Association*, vol. 65, pp. 904–912, 1970

[12] K. Larntz and M. D. Perlman, "A simple test for the equality of correlation matrices," *Department of Statistics, University of Washington*, Tech. Rep., 1985.

[13] A. A. Goulianos, T. W. C. Brown and S. Stavrou, "A Novel Path-Loss Model for UWB Off-Body Propagation", in *Proc. of IEEE Vehicular Techn. Conf.,* Singapore, May 11-14, 2008

[14] A. A. Goulianos, T. W. C. Brown and S. Stavrou, "Power delay profile modeling of the ultra wideband off-body propagation channel", IET Microwaves, Antennas & Propagation, 2009

[15] A. A. Goulianos, T. W. C. Brown, B. G. Evans and S. Stavrou,"Wideband Power Modeling and Time Dispersion Analysis for UWB Indoor Off-Body Communications", *IEEE Trans. on Antennas and Propagation*, vol. 57, no. 7, July 2009

[16] R. Rosini and R. D'Errico, "Off-Body Channel Modelling at 2.45 GHz for Two Different Antennas", in *Proc. of IEEE 6th European Conference on Antennas and Propagation* (EuCAP 2011)

[17] R. Rosini and R. D'Errico, "Space-time correlation for on-to-Off Body channels at 2.45 GHz," Antennas and Propagation (EuCAP), 2013 7th European Conference on , vol., no., pp.3529,3533, 8-12 April 2013

[18] N. Czink, "The Random Cluster Model – A Stochastic MIMO Channel Model for Broadband Wireless Communication Systems of the 3rd Generation and Beyond", *PhD thesis dissertation*, 2007

[19] A. P. Dempster, N. M. Laird, and D. B. Rubin, "Maximum likelihood from incomplete data via the EM algorithm," J. Royal Statist. SOc., Ser. B, vol. 39, no. 1, PP. 1-38, 1977

[20] B. H. Fleury, D. Dahlaus, R. Heddergott, and M. Tschudin, "Wideband Angle of Arrival Estimation using the SAGE Algorithm", International Symposium on Spread Spectrum Techniques and Applications, ISSSTA 1996

[21] C. Chong, D. I. Laurenson, C. Tan, S. McLaughlin, M. A. Beach, and A. Nix, "Joint detection-estimation of directional channel parameters using the SAGE algorithm", IEEE International Conference on Communications, vol. 2, New York, USA, April 2002, pp. 906-910

[22] M. Matthaiou and N. Nrazavi-Ghods, "Characterization of an indoor MIMO channel in frequency domain using the 3D-SAGE algorithm", in IEEE International Conference on Communications, vol. 24-28, June 2007, pp. 5868 – 5872

[23] K. Haneda and J.-I. Takada, "An application of SAGE algorithm for UWB propagation channel estimation", in IEEE Conference on Ultra Wideband Systems and Technologies, Nov. 2003, pp. 483 – 487

[24] K. Haneda, J.-I. Takada, and T. Kobayashi, "Experimental evaluation of a SAGE algorithm for ultra wideband channel sounding in an anechoic chamber," in International Workshop on Joint UWBST & IWUWBS, May 2004, pp.66-70

[25] S. V. Roy, L. Liu, C. Oestges and Ph. De Doncker, "An Ultra-wideband SAGE Algorithm for Body Area Networks", in *Proc. of IEEE ICEAA 2009*

[26] B. H. Fleury, M. Tschudin, R. Heddergott, D. Dahlaus, K. I. Pedersen, "Channel Parameter Estimation in Mobile Radio Environments Using the SAGE Algorithm", Journal on Selected Areas in Communications, vol. 17, no. 3, March 1999

[27] A. Richter, J. Salmi and V. Koivunen, "An Algorithm for Estimation and Tracking of Distributed Diffuse Scattering in Mobile Radio Channels", *in Proc. of IEEE 7th International Workshop on Signal Processing Advances for Wireless Communications*, Jul. 2006

[28] F. Quitin, C. Oestges, F. Horlin and P. De Doncker, "A Polarized Clustered Channel Model for Indoor Multiantenna Systems at 3.6 GHz", *IEEE Trans. On Vehicular Technology*, Oct. 2010

[29] F. Quitin, C. Oestges, F. Bellens, S. van Roy, F. Horlin and P. De Doncker, "Extracting specular-diffuse clusters from MIMO channel measurements", in *Proc. Of IEEE 12nd International Symposium on Personal, Indoor and Mobile Radio Communications* (PIMRC 2011)

[30] K. Haneda, J. Takada and T. Kobayashi, "Cluster Properties Investigated From a Series of Ultrawideband Double Directional Propagation Measurements in Home Environments", in *Proc. In IEEE Transaction on Antennas and Propagation*, vol. 54, no. 12, Dec. 2006

[31] R. Rosini, R. D'Errico and R. Verdone, "Body-to-Body Communications: a Measurement-based Channel Model at 2.45 GHz", in *Proc. of IEEE 23rd International Symposium on Personal, Indoor and Mobile Radio Communications (*PIMRC 2012)

[32] Louis-Marie Aubert and S Paquelet, "Mise en place d'une couche physique pour les futurs systèmes de radiocommunications hauts débits uwb", PhDReport, 2005.

[33] S. Paquelet, L.-M. Aubert, and B. Uguen, "An impulse radio asynchronous transceiver for high data rates", pages 1–5. *Institute of Electrical and Electronics Engineers, 2004.*

[34] I. Guvenc and H. Arslan, "Bit error rates of IR-UWB transceiver types at sub-nyquist sampling rates", pages 1080–1085, *Institute of Electrical and Electronics Engineers, 2006*

[35] Jean Schwoerer, "Études et implémentation d'une couche physique UWB impulsionnelle à bas débit et faible complexité¶", *PhD thesis*, 2006.

[36] Ahmed BENFARAH, "Conception d'une chaîne de communication pour réseaux ban sur couche phy uwb-ir" *Master's thesis, Universite Pierre et Marie Curie (Paris VI), Telecom ParisTech*, 2009

[37] Soon-Woo Lee, Young-Jin Park, Jimyung Kang, and Kwan-Ho Kim, "An IR-UWB Receiver Design for Low Cost Applications", pages 653–656, *Institute of Electrical and Electronics Engineers,* Sep 2007.

[38] Dazhong Mu and Zhengding Qiu, "Weighted non-coherent energy detection receiver for UWB OOK systems", pages 1846–1849, *Institute of Electrical and Electronics Engineers*, Oct 2008.

[39] Klaus Witrisal, Geert Leus, Gerard Janssen, Marco Pausini, Florian Troesch, Thomas Zasowski, and Jac Romme, "Noncoherent ultra-wideband systems", *IEEE Signal Processing Magazine,* 26(4):48–66, Jul 2009.

[40] Benoît Miscopein, "Systèmes uwb impulsionnels noncohérents pour les réseaux de capteurs: coexistence et coopération", *PhD thesis, Ph. D. dissertation*, INSA Lyon, 2010.

[41] Ville Niemela, Alberto Rabbachin, Attaphongse Taparugssanagorn, Matt Hamalainen, and Jari Iinatti, "A comparison of UWB WBAN receivers indifferent measured hospital environments", pages 1–5. *Institute of Electrical and Electronics Engineers*, Nov 2010.

[42] Ville Niemela, Jari Iinatti, Matti Hamalainen, and Attaphongse Taparugssanagorn, "On the energy detector, P- and s-rake receivers in a measured UWB channel inside a hospital", pages 1–5. *Institute of Electrical and Electronics Engineers,* Nov 2010.

[43] Ville Niemela, Matti Hamalainen, and Jari Iinatti, "On IEEE 802.15.6 UWB symbol length for energy detector receivers performance with OOK and PPM", pages 33–37. *Institute of Electrical and Electronics Engineers,* Mar 2013.

[44] Ville Niemelä, Jussi Haapola, Matti Hämäläinen, and Jari Iinatti, "Integration interval and threshold evaluation for an energy detector receiver with ppm and ook modulations", *In Proceedings of the 7th International Conference on Body Area Networks,* pages 242–248. ICST, 2012

[45] IEEE standard for local and metropolitan area networks - part 15.6: Wire-less body area networks, 2012. IEEE Std 802.15.6-2012.

9. ANNEXES

9.1. SAGE AND CLUSTERING RESULTS

We present here figures giving SAGE and clustering results for environments, all the Rx antenna location, all the phantom orientations, for a distance equal to 8 m.

9.1.1   ENVIRONMENT 1

• *Isolated antenna*
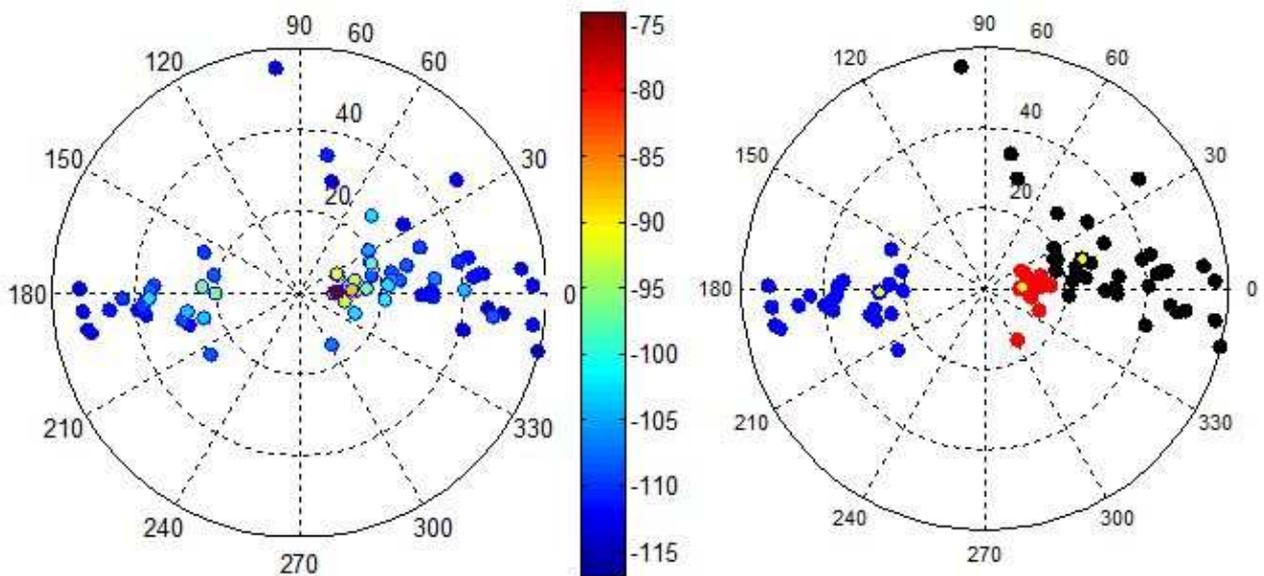
Figure 85 : SAGE (left) and Clustering (right) results – Isolated antenna – d_{off} = 8m – env 1

- *Rx on Torso*
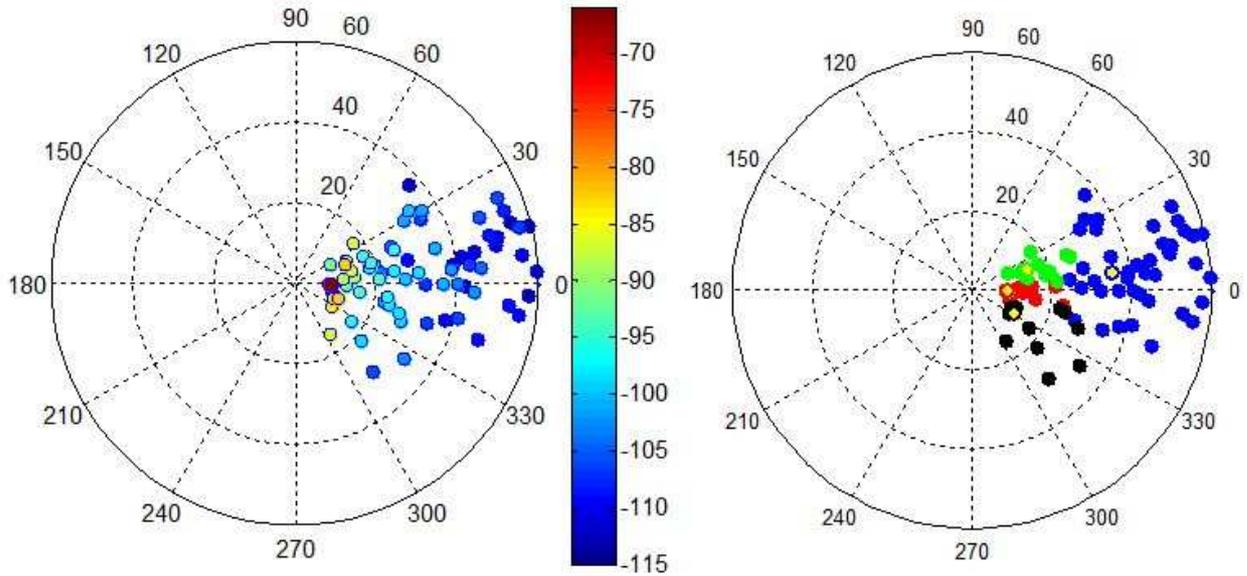
Figure 86 : SAGE (left) and Clustering (right) results – Torso – env 1 - d_{off} = 8m – $\Phi = 0°$
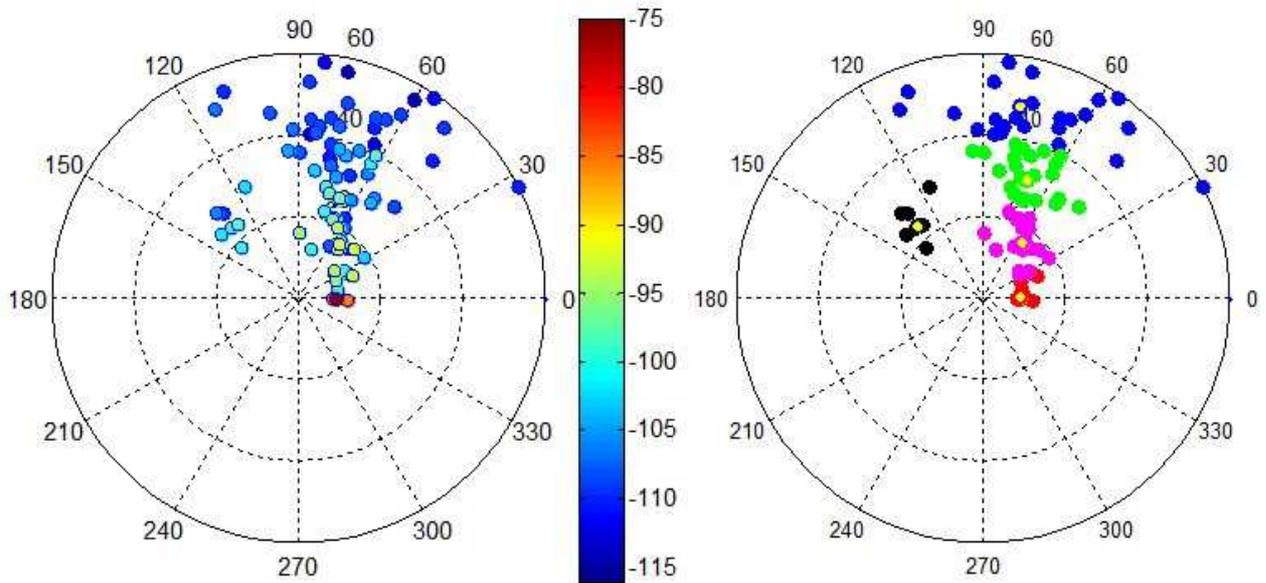
Figure 87 : SAGE (left) and Clustering (right) results – Torso – env 1 - d_{off} = 8m – $\Phi = 90°$
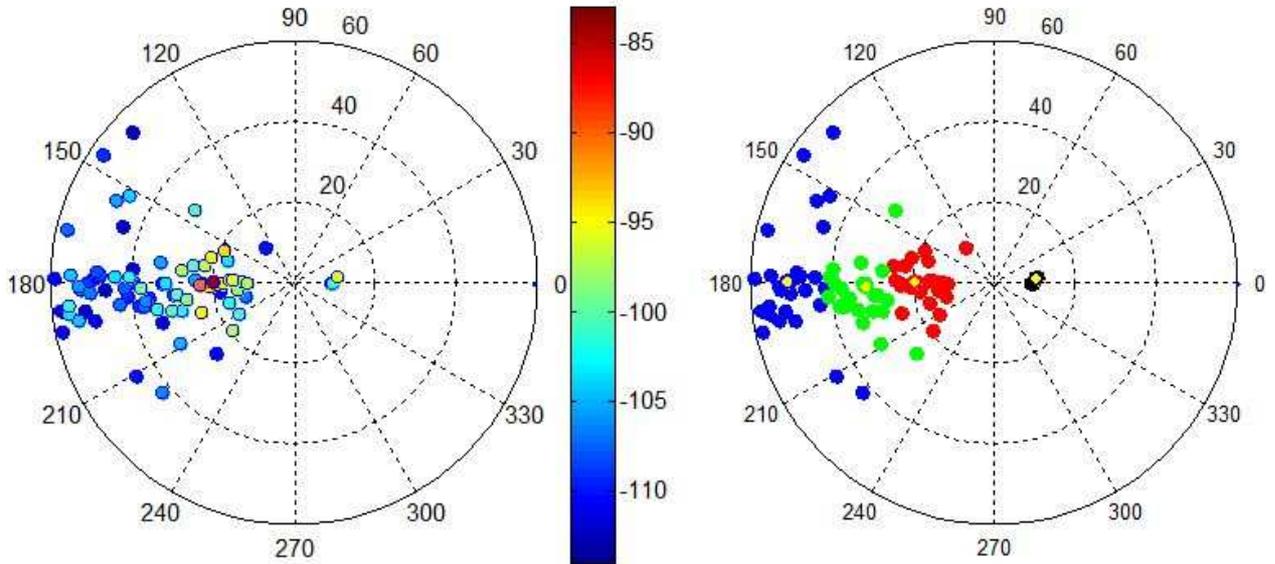
Figure 88 : SAGE (left) and Clustering (right) results – Torso – env 1 - d_{off} = 8m – $\Phi = 180°$

- *Rx on Shoulder*
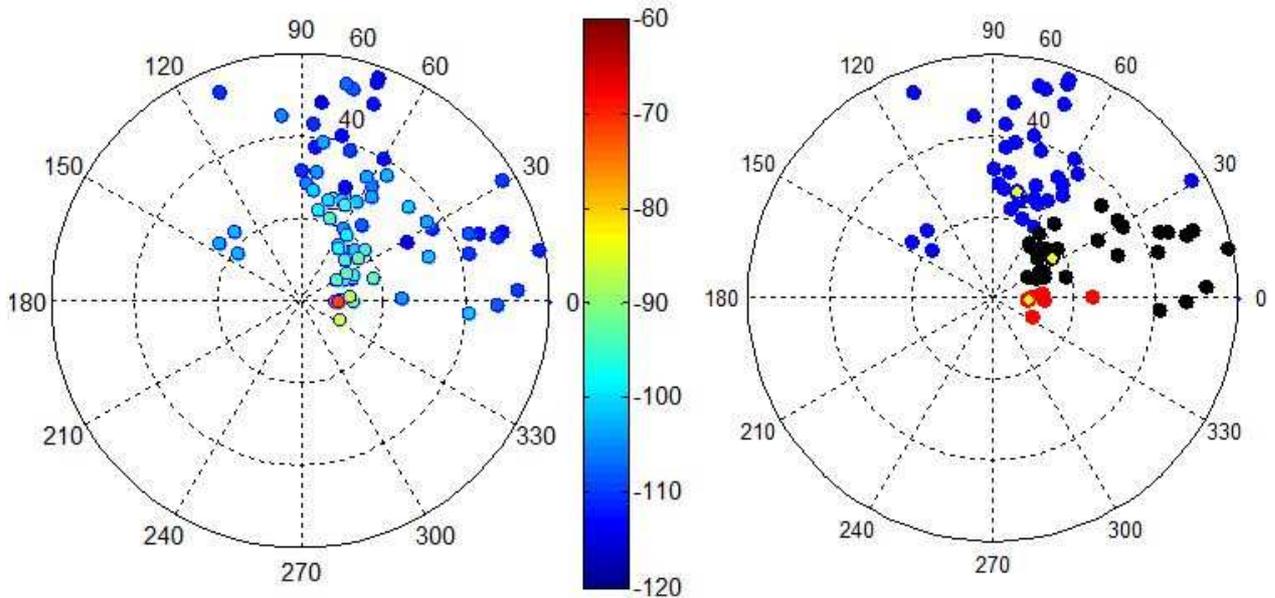
Figure 89 : SAGE (left) and Clustering (right) results – Shoulder – env 1 - d_{off} = 8m – $\Phi = 0°$
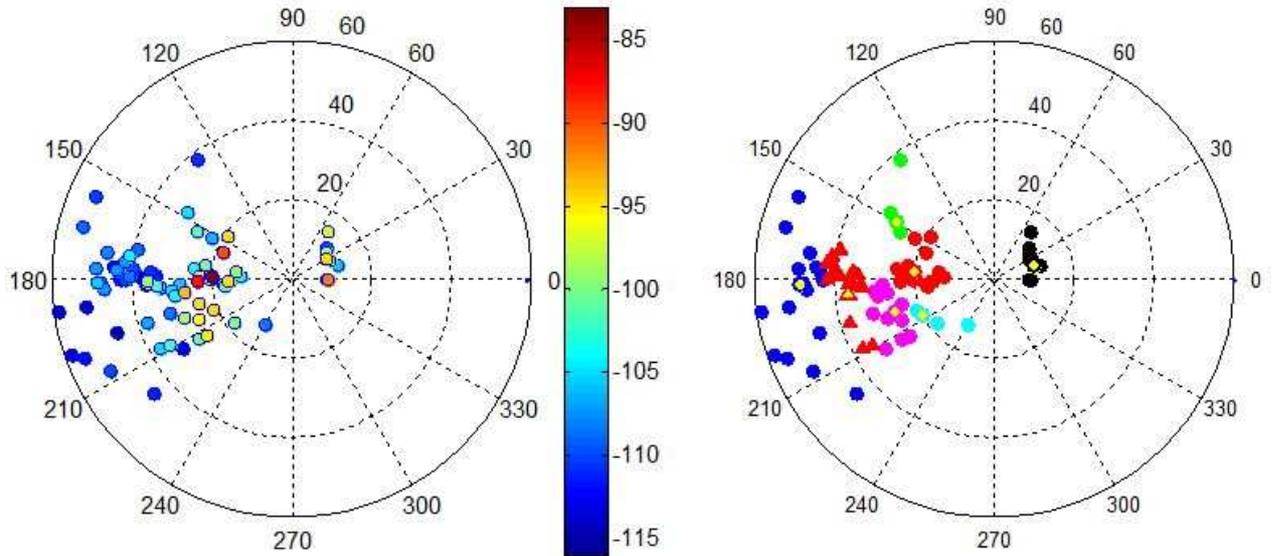
Figure 90 : SAGE (left) and Clustering (right) results – Shoulder – env 1 - d_{off} = 8m – Φ = 90°
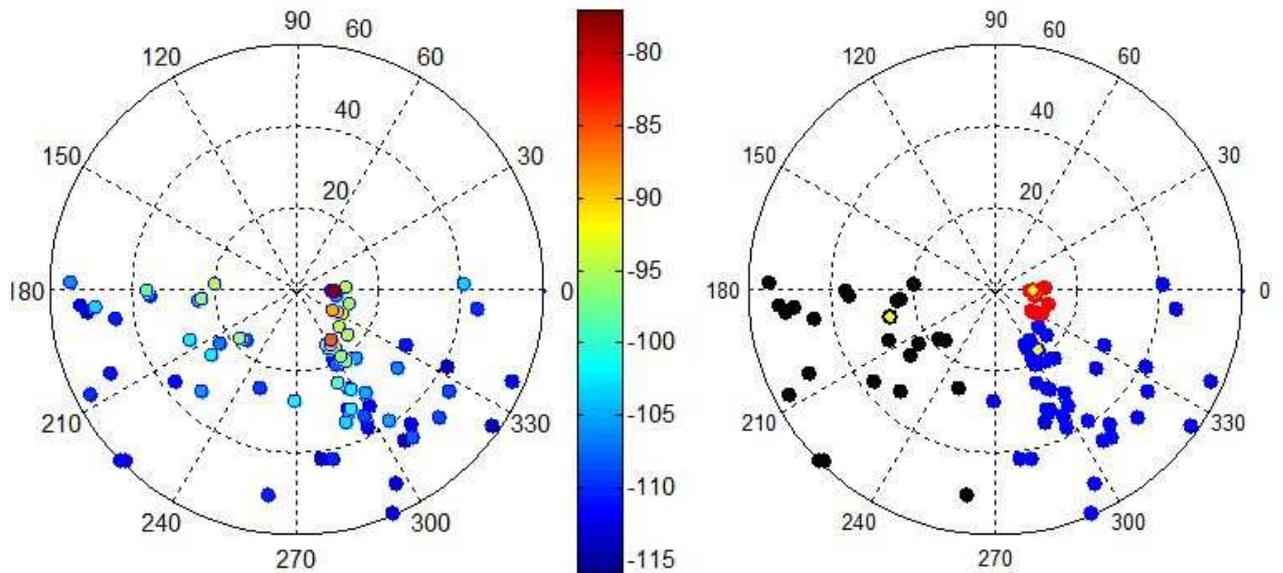
Figure 91: SAGE (left) and Clustering (right) results – Shoulder – env 1 - d_{off} = 8m – Φ = 180°

- *Rx on Back*
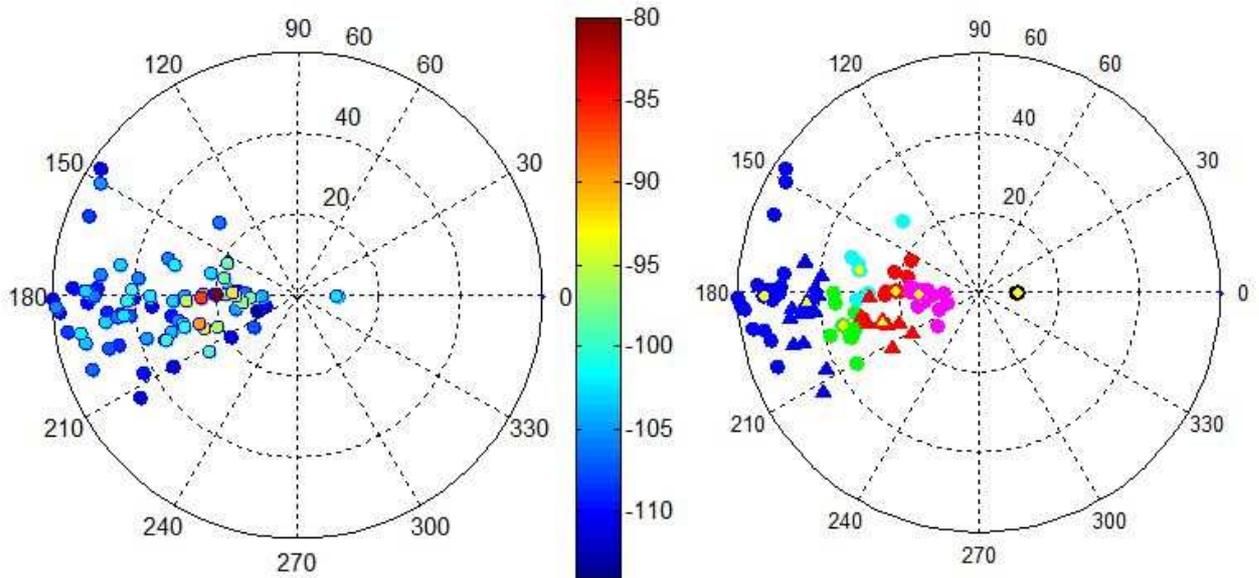
Figure 92 : SAGE (left) and Clustering (right) results – Back – env 1 - d_{off} = 8m – $\Phi = 0°$
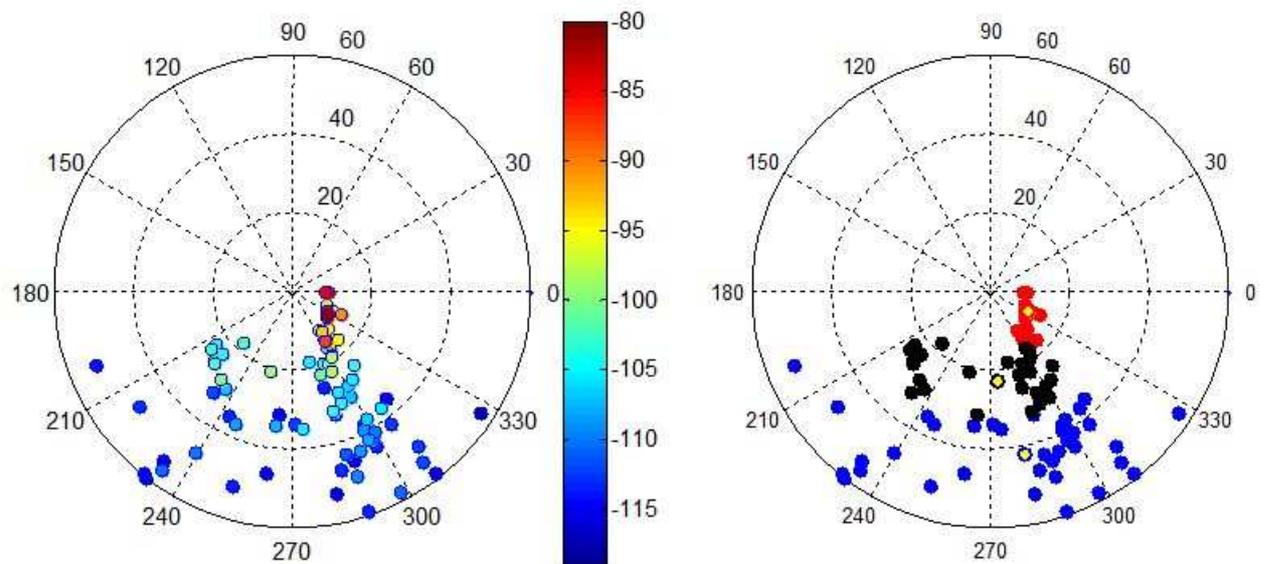
Figure 93: SAGE (left) and Clustering (right) results – Back – env 1 - d_{off} = 8m – $\Phi = 90°$
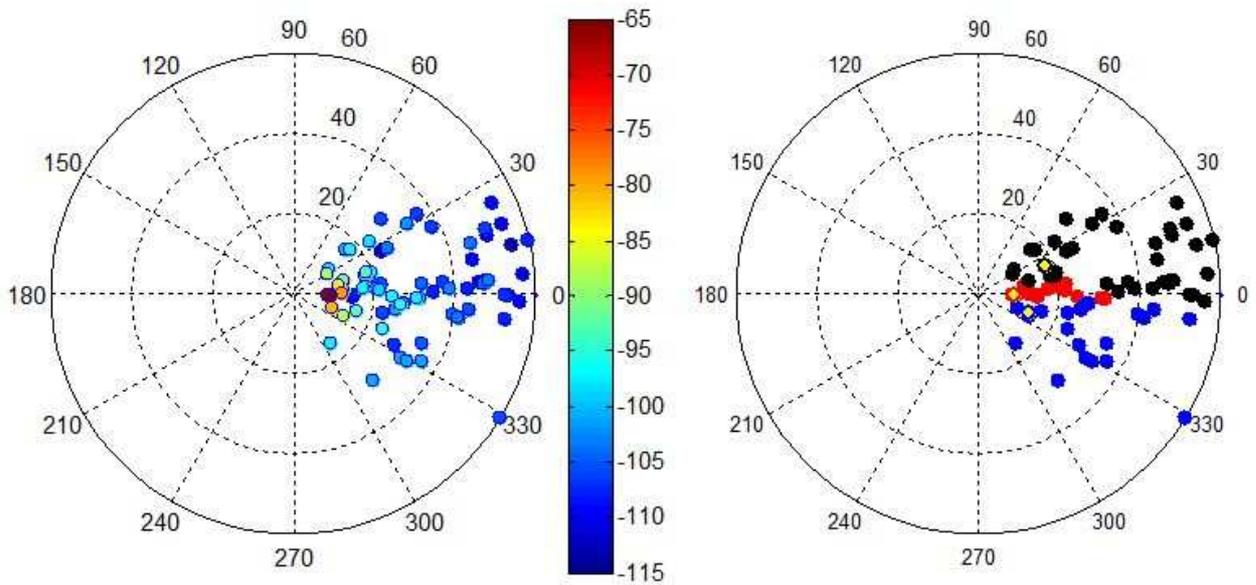
Figure 94 : SAGE (left) and Clustering (right) results – Back – env 1 - d_{off} = 8m – $\Phi = 180°$

9.1.2 ENVIRONMENT 2

- *Isolated antenna*
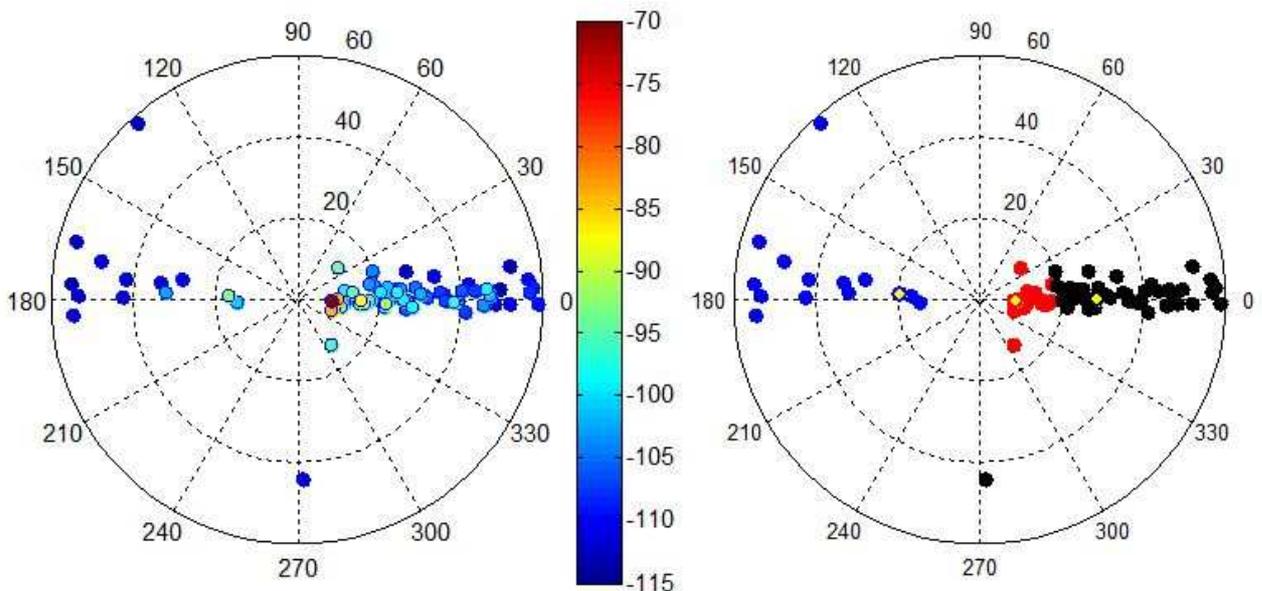
Figure 95: SAGE (left) and Clustering (right) results – Isolated antenna – env 2 - d_{off} = 8m

- *Rx on Torso*
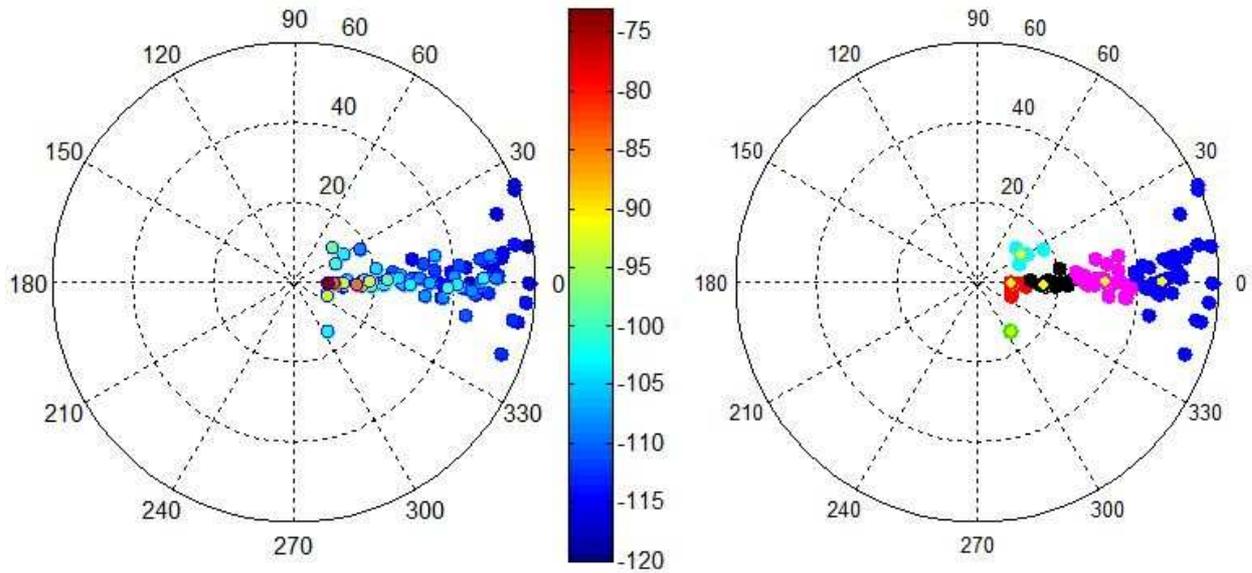
Figure 96 : SAGE (left) and Clustering (right) results – Torso – env 2 - d_{off} = 8m – $\Phi = 0°$
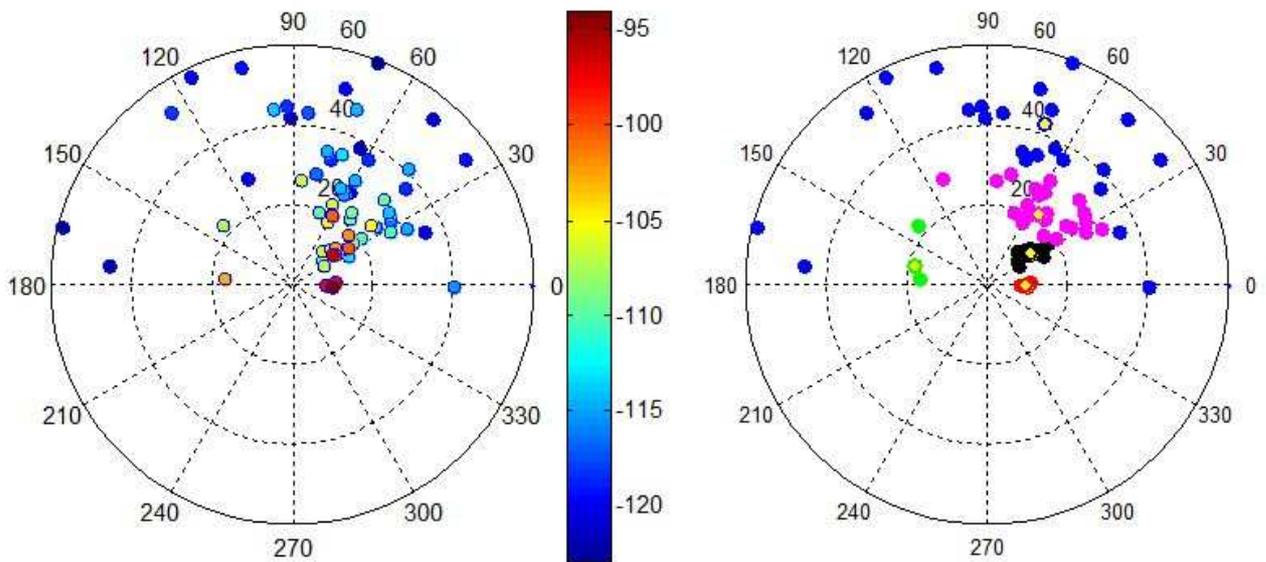
Figure 97 : SAGE (left) and Clustering (right) results – Torso – env 2 - d_{off} = 8m – $\Phi = 90°$
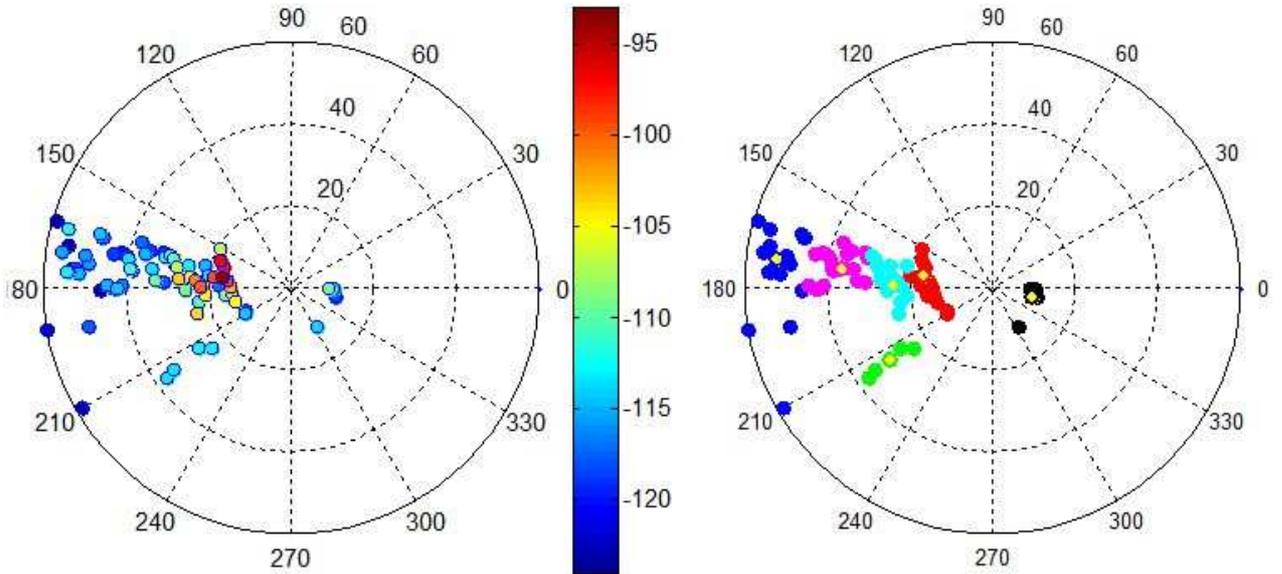
Figure 98: SAGE (left) and Clustering (right) results – Torso – env 2 - d_{off} = 8m – Φ = 180°

- *Rx on Shoulder*

Figure 99 : SAGE (left) and Clustering (right) results – Shoulder – env 2 - d_{off} = 8m – Φ = 0°
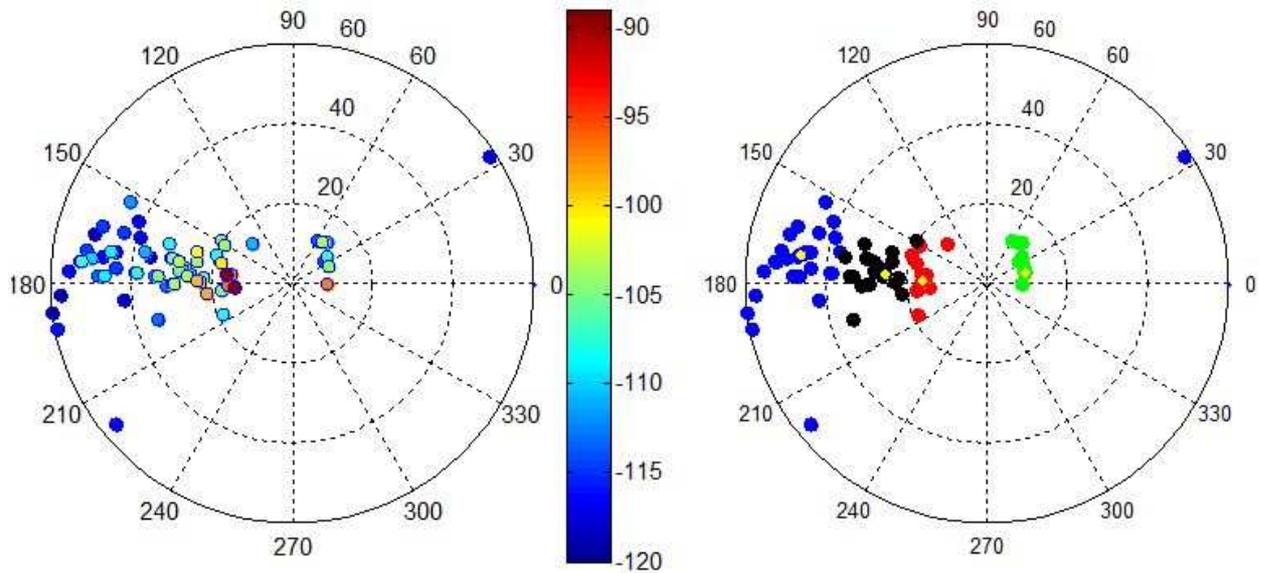
Figure 100: SAGE (left) and Clustering (right) results – Shoulder – env 2 - d_{off} = 8m – $\Phi = 90°$
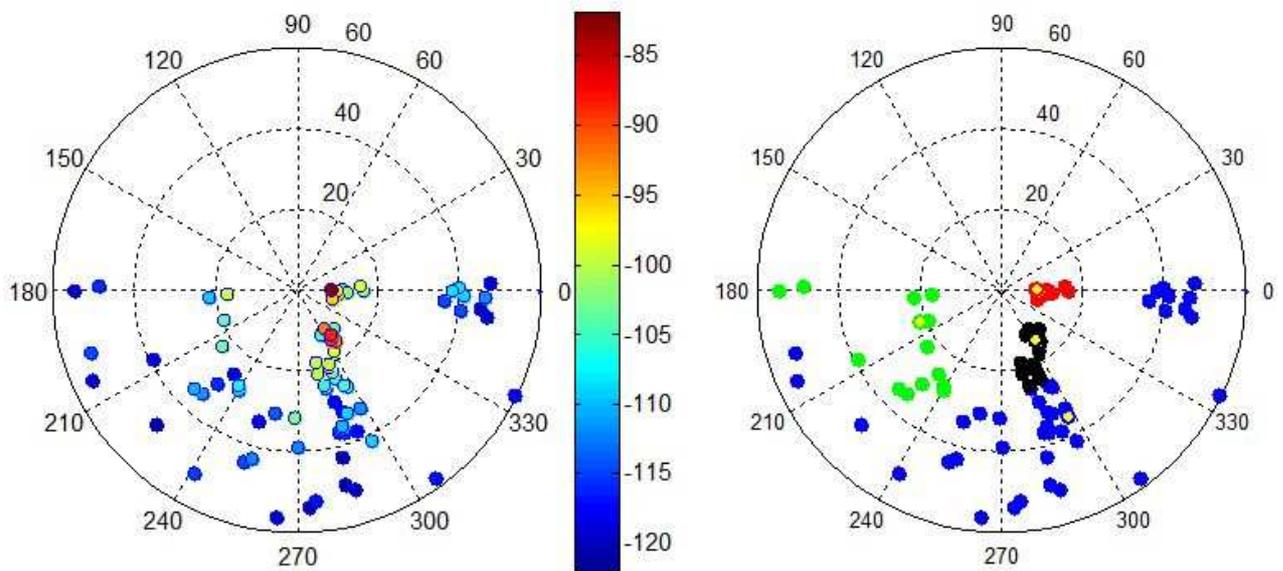
Figure 101: SAGE (left) and Clustering (right) results – Shoulder – env 2 - d_{off} = 8m – $\Phi = 180°$

- *Rx on Back*
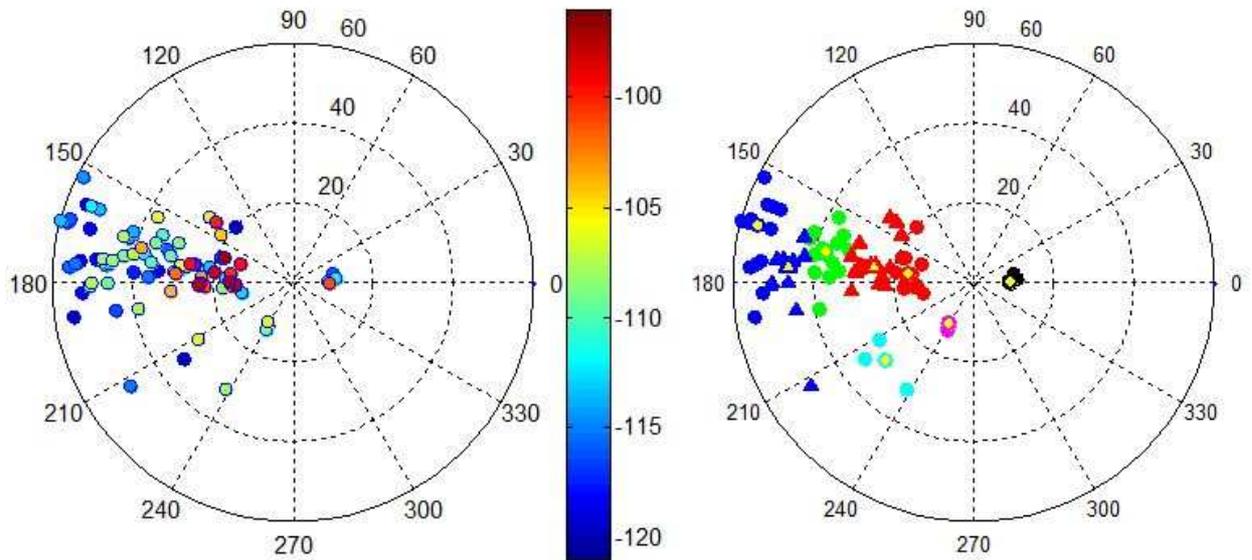
Figure 102: SAGE (left) and Clustering (right) results – Back – env 2 - d_{off} = 8m – $\Phi = 0°$
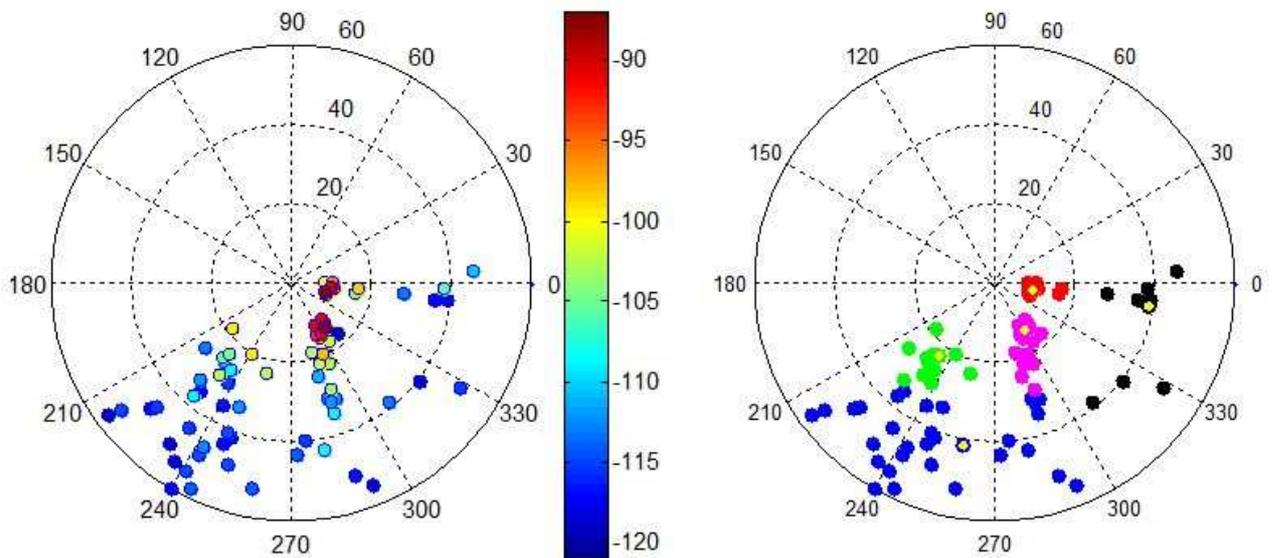
Figure 103: SAGE (left) and Clustering (right) results – Back – env 2 - d_{off} = 8m – $\Phi = 90°$
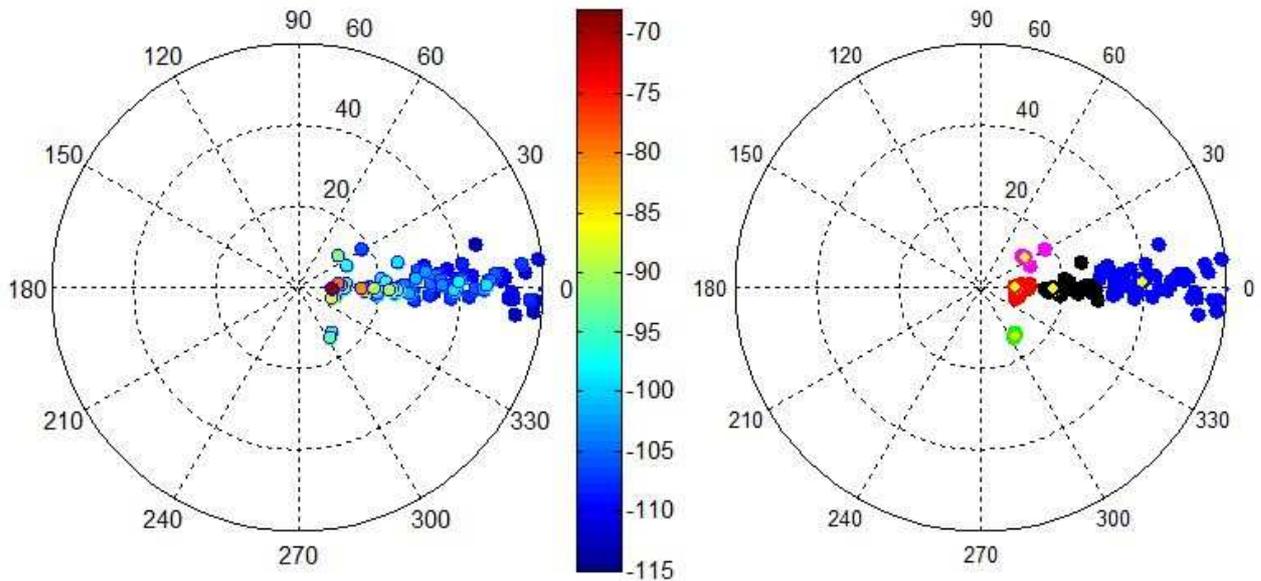
Figure 104: SAGE (left) and Clustering (right) results – Back – env 2 - d_{off} = 8m – $\Phi = 180°$

9.2. CENTROID DELAY

9.2.1   ISOLATED ANTENNA

$\bar{\tau}_k$ (ns)	d_{off} = 1m	d_{off} = 2m	d_{off} = 3m	d_{off} = 4m	d_{off} = 5m	d_{off} = 6m	d_{off} = 7m	d_{off} = 8m
$k = 1$	5.00	10.34	12.50	16.14	18.70	25.98	28.22	31.01
$k = 2$	54.80	81.47	77.24	89.27	85.32	95.63	81.20	86.56
$k = 3$		29.15	40.56	49.68	46.70			84.06
$k = 4$		19.91		36.52	43.67			

Table 23 : Centroid delay – Isolated antenna – env 1

9.2.2   RX ON TORSO

$\bar{\tau}_k$ (ns)	d_{off} = 1m	d_{off} = 2m	d_{off} = 3m	d_{off} = 4m	d_{off} = 5m	d_{off} = 6m	d_{off} = 7m	d_{off} = 8m
$k = 1$	5.3	11.5	13.3	15.0	19.4	25.3	26.7	29.4
$k = 2$	29.0	25.8	34.5	44.6	41.8	117.5	131.5	117.0
$k = 3$			35.6	25.2	106.2	44.3	54.8	40.1
$k = 4$				38.7				49.0

Table 24: Centroid delay – Torso – $\Phi = 0°$ – env 1

$\bar{\tau}_k$ (ns)	d_{off} = 1m	d_{off} = 2m	d_{off} = 3m	d_{off} = 4m	d_{off} = 5m	d_{off} = 6m	d_{off} = 7m	d_{off} = 8m

	d_{off} $= 1m$	d_{off} $= 2m$	d_{off} $= 3m$	d_{off} $= 4m$	d_{off} $= 5m$	d_{off} $= 6m$	d_{off} $= 7m$	d_{off} $= 8m$
$k = 1$	4.9	10.6	13.0	18.7	20.6	23.5	26.2	30.6
$k = 2$	70.3	32.4	33.7	122.1	35.0	118.6	48.6	120.5
$k = 3$	24.5	17.5	49.2	35.7	105.3	41.3	120.1	62.0

Table 25: Centroid delay – Torso – Φ = 45° – env 1

$\bar{\tau}_k$ (ns)	d_{off} $= 1m$	d_{off} $= 2m$	d_{off} $= 3m$	d_{off} $= 4m$	d_{off} $= 5m$	d_{off} $= 6m$	d_{off} $= 7m$	d_{off} $= 8m$
$k = 1$	9.4	12.2	13.5	24.3	20.8	23.2	26.9	30.9
$k = 2$	143.8	54.9	104.0	116.0	138.6	142.3	149.5	160.0
$k = 3$	71.6	27.1	34.8	54.1	64.0	78.1	87.0	79.1
$k = 4$	26.7	126.8		40.1	35.4	38.1	75.8	102.7
$k = 5$		50.9					38.7	55.5

Table 26: Centroid delay – Torso – Φ = 90° – env 1

$\bar{\tau}_k$ (ns)	d_{off} $= 1m$	d_{off} $= 2m$	d_{off} $= 3m$	d_{off} $= 4m$	d_{off} $= 5m$	d_{off} $= 6m$	d_{off} $= 7m$	d_{off} $= 8m$
$k = 1$	24.4	28.4	35.3	26.0	41.5	76.9	63.0	64.6
$k = 2$	74.4	89.9	141.3	136.1	163.4	167.1	174.8	128.6
$k = 3$	19.1	23.4	87.4	85.8	82.8	27.9	27.7	
$k = 4$	36.1	47.5		22.2	33.0	103.3	92.2	
$k = 5$	11.4	12.4		42.0	20.8	128.7	50.8	
$k = 6$	98.6				118.1	46.1	128.0	
$k = 7$						33.0		

Table 27: Centroid delay – Torso – Φ = 135° – env 1

$\bar{\tau}_k$ (ns)	d_{off} $= 1m$	d_{off} $= 2m$	d_{off} $= 3m$	d_{off} $= 4m$	d_{off} $= 5m$	d_{off} $= 6m$	d_{off} $= 7m$	d_{off} $= 8m$
$k = 1$	18.5	24.4	83.0	86.8	36.1	41.0	70.3	65.5
$k = 2$	153.6	165.2	141.5	179.4	153.2	175.7	174.1	170.1
$k = 3$	97.1	11.3	19.4	18.5	25.7	28.2	27.9	34.4
$k = 4$	10.8	98.9	35.0	121.2	83.1	79.2	97.4	105.8
$k = 5$	66.7	61.0		37.3		126.9	43.4	
$k = 6$	41.5			50.2			61.5	
$k = 7$							39.3	
$k = 8$							132.0	

Table 28: Centroid delay – Torso – Φ = 180° – env 1

9.2.3 RX ON SHOULDER

$\bar{\tau}_k$ (ns)	$d_{off} = 1m$	$d_{off} = 2m$	$d_{off} = 3m$	$d_{off} = 4m$	$d_{off} = 5m$	$d_{off} = 6m$	$d_{off} = 7m$	$d_{off} = 8m$
$k = 1$	6.3	10.2	13.5	15.9	20.9	23.4	26.5	29.8
$k = 2$	36.3	26.8	37.5	55.6	79.3	55.5	75.4	89.7
$k = 3$				40.4	97.8		35.3	58.7
$k = 4$				52.1	30.1			
$k = 5$					60.7			

Table 29: Centroid delay – Shoulder – Φ = 0° – env 1

$\bar{\tau}_k$ (ns)	$d_{off} = 1m$	$d_{off} = 2m$	$d_{off} = 3m$	$d_{off} = 4m$	$d_{off} = 5m$	$d_{off} = 6m$	$d_{off} = 7m$	$d_{off} = 8m$
$k = 1$	5.6	23.1	17.4	15.8	20.3	23.8	27.4	30.2
$k = 2$	93.2	102.1	98.9	70.0	143.8	122.4	133.0	139.6
$k = 3$	34.3	49.6	40.1	129.5	56.4	64.2	63.2	75.3
$k = 4$	36.6	31.4		38.8	30.5	46.6	72.9	63.9
$k = 5$	99.4	11.1			79.2			
$k = 6$		53.7						

Table 30: Centroid delay – Shoulder – Φ = 45° – env 1

$\bar{\tau}_k$ (ns)	$d_{off} = 1m$	$d_{off} = 2m$	$d_{off} = 3m$	$d_{off} = 4m$	$d_{off} = 5m$	$d_{off} = 6m$	$d_{off} = 7m$	$d_{off} = 8m$
$k = 1$	21.0	26.9	23.2	25.0	26.9	47.2	67.6	67.4
$k = 2$	140.2	147.4	135.4	176.4	172.0	175.4	173.0	162.6
$k = 3$	55.8	38.1	86.4	88.7	83.2	94.9	29.6	34.8
$k = 4$	93.2	14.2	44.4	129.9	45.1	26.8	95.2	94.8
$k = 5$	27.7	83.2		46.2	45.6	73.5	131.2	87.9
$k = 6$	21.3			40.1	125.3	131.0	41.1	66.9
$k = 7$	9.8				109.8	24.3		122.3
$k = 8$	60.2					41.4		
$k = 9$						54.0		

Table 31: Centroid delay – Shoulder – Φ = 90° – env 1

$\bar{\tau}_k$ (ns)	$d_{off} = 1m$	$d_{off} = 2m$	$d_{off} = 3m$	$d_{off} = 4m$	$d_{off} = 5m$	$d_{off} = 6m$	$d_{off} = 7m$	$d_{off} = 8m$
$k = 1$	6.4	13.9	13.8	17.3	27.9	27.8	26.5	69.2
$k = 2$	101.6	100.0	92.2	169.4	145.4	107.1	162.5	177.3
$k = 3$	44.2	49.5	62.7	84.2	79.8	74.8	70.8	32.8
$k = 4$	50.0		132.1	111.0		173.4	100.8	116.9
$k = 5$	21.3		37.0	42.9			40.8	

$\bar{\tau}_k$ (ns)				57.8				
$k = 6$				57.8				

Table 32: Centroid delay – Shoulder – $\Phi = 135°$ – env 1

$\bar{\tau}_k$ (ns)	$d_{off} = 1m$	$d_{off} = 2m$	$d_{off} = 3m$	$d_{off} = 4m$	$d_{off} = 5m$	$d_{off} = 6m$	$d_{off} = 7m$	$d_{off} = 8m$
$k = 1$	6.0	11.2	13.9	15.1	19.5	22.7	27.0	29.9
$k = 2$	24.2	77.1	98.3	100.2	98.4	83.2	119.4	60.5
$k = 3$		26.1	66.5	28.4	30.9	42.9	59.5	87.7
$k = 4$		27.9	55.6	57.7	119.5	87.0	79.0	
$k = 5$			29.7		54.9			

Table 33: Centroid delay – Shoulder – $\Phi = 180°$ – env 1

9.2.4   RX ON THE BACK

$\bar{\tau}_k$ (ns)	$d_{off} = 1m$	$d_{off} = 2m$	$d_{off} = 3m$	$d_{off} = 4m$	$d_{off} = 5m$	$d_{off} = 6m$	$d_{off} = 7m$	$d_{off} = 8m$
$k = 1$	24.7	25.6	36.6	80.1	80.4	59.7	69.5	69.1
$k = 2$	157.8	150.8	141.1	165.5	179.5	149.2	139.8	178.1
$k = 3$	9.6	86.8	87.3	17.6	22.1	24.1	28.4	31.5
$k = 4$	96.5		13.9	49.1	118.2	95.8		115.5
$k = 5$	63.2			104.5	31.5			49.8
$k = 6$				39.6	98.7			100.0
$k = 7$					55.6			83.6
$k = 8$					151.1			143.3

Table 34: Centroid delay – Back – $\Phi = 0°$ – env 1

$\bar{\tau}_k$ (ns)	$d_{off} = 1m$	$d_{off} = 2m$	$d_{off} = 3m$	$d_{off} = 4m$	$d_{off} = 5m$	$d_{off} = 6m$	$d_{off} = 7m$	$d_{off} = 8m$
$k = 1$	20.8	28.7	21.7	47.8	82.1	78.6	69.9	71.0
$k = 2$	104.6	162.5	143.7	173.7	171.9	147.5	168.4	177.9
$k = 3$	36.3	74.2	43.9	108.8	20.1	23.4	27.8	42.9
$k = 4$	66.0	12.4	95.7	21.6	145.4	133.4	115.0	107.8
$k = 5$		105.9		88.8	55.4	40.5	46.6	119.9
$k = 6$		31.3		124.6	39.9	49.2		147.6
$k = 7$					119.1	113.2		55.9
$k = 8$								93.1

Table 35: Centroid delay – Back – $\Phi = 45°$ – env 1

$\bar{\tau}_k$ (ns)	$d_{off} = 1m$	$d_{off} = 2m$	$d_{off} = 3m$	$d_{off} = 4m$	$d_{off} = 5m$	$d_{off} = 6m$	$d_{off} = 7m$	$d_{off} = 8m$
$k = 1$	5.3	11.1	13.6	22.6	23.2	24.9	30.3	35.5

k = 2	49.5	116.6	106.4	120.8	137.7	133.0	113.3	141.3
k = 3	126.3	24.0	58.8	53.8	67.4	56.0	52.5	76.2
k = 4	22.6		91.1		49.1	91.0	75.7	
k = 5			26.6					

Table 36: Centroid delay – Back – Φ = 90° – env 1

$\bar{\tau}_k$ (ns)	d_{off} = 1m	d_{off} = 2m	d_{off} = 3m	d_{off} = 4m	d_{off} = 5m	d_{off} = 6m	d_{off} = 7m	d_{off} = 8m
k = 1	4.6	10.5	13.0	18.0	18.3	23.0	25.8	30.9
k = 2	25.9	32.9	34.0	114.9	45.4	84.0	64.8	141.1
k = 3				30.2	112.7	31.6	105.1	60.3
k = 4					28.9		33.4	

Table 37: Centroid delay – Back – Φ = 135° – env 1

$\bar{\tau}_k$ (ns)	d_{off} = 1m	d_{off} = 2m	d_{off} = 3m	d_{off} = 4m	d_{off} = 5m	d_{off} = 6m	d_{off} = 7m	d_{off} = 8m
k = 1	5.7	9.0	14.4	15.1	19.6	21.7	27.6	29.1
k = 2			36.1	30.6	42.8	118.5	133.7	44.4
k = 3			39.2	44.3	116.9	41.8	42.4	59.4
k = 4				40.6	40.0	46.2		

Table 38: Centroid delay – Back – Φ = 180° – env 1

9.3. CLUSTER DELAY DISPERSION

9.3.1   ISOLATED ANTENNA

τ_{rms} (ns)	d_{off} = 1m	d_{off} = 2m	d_{off} = 3m	d_{off} = 4m	d_{off} = 5m	d_{off} = 6m	d_{off} = 7m	d_{off} = 8m
k = 1	4.34	3.64	4.20	2.78	2.75	9.69	7.99	3.98
k = 2	30.43	33.88	30.87	20.70	17.02	26.21	21.10	24.28
k = 3		11.04	13.50	23.35	27.80			30.83
k = 4		13.89		14.79	18.96			

Table 39 : Cluster delay dispersion values – Isolated Antenna – env 1

9.3.2   RX ON TORSO

τ_{rms} (ns)	d_{off} = 1m	d_{off} = 2m	d_{off} = 3m	d_{off} = 4m	d_{off} = 5m	d_{off} = 6m	d_{off} = 7m	d_{off} = 8m
k = 1	5.05	4.55	4.97	3.52	3.47	6.53	3.34	2.93
k = 2	9.48	11.57	33.66	22.90	24.26	27.29	31.27	28.75

		d_{off} = 1m	d_{off} = 2m	d_{off} = 3m	d_{off} = 4m	d_{off} = 5m	d_{off} = 6m	d_{off} = 7m	d_{off} = 8m
$k = 3$				15.86	15.46	34.15	12.87	17.20	10.15
$k = 4$					12.63				9.84

Table 40: Cluster delay dispersion values – Torso – $\Phi = 0°$ – env 1

τ_{rms} (ns)	d_{off} = 1m	d_{off} = 2m	d_{off} = 3m	d_{off} = 4m	d_{off} = 5m	d_{off} = 6m	d_{off} = 7m	d_{off} = 8m
$k = 1$	2.86	3.11	2.79	5.72	2.70	5.71	1.75	5.51
$k = 2$	25.12	17.38	17.14	31.45	14.14	28.02	21.11	23.35
$k = 3$	7.06	12.26	32.04	12.51	35.00	11.57	34.64	10.76

Table 41: Cluster delay dispersion values – Torso – $\Phi = 45°$ – env 1

τ_{rms} (ns)	d_{off} = 1m	d_{off} = 2m	d_{off} = 3m	d_{off} = 4m	d_{off} = 5m	d_{off} = 6m	d_{off} = 7m	d_{off} = 8m
$k = 1$	4.11	1.86	2.00	4.72	0.37	1.94	2.15	3.49
$k = 2$	21.34	12.64	30.09	28.69	24.54	23.23	20.54	18.15
$k = 3$	13.92	8.11	10.73	12.43	18.17	13.68	15.44	11.44
$k = 4$	8.40	27.45		14.57	10.65	8.46	13.33	17.10
$k = 5$		11.22					9.78	10.11

Table 42: Cluster delay dispersion values – Torso – $\Phi = 90°$ – env 1

τ_{rms} (ns)	d_{off} = 1m	d_{off} = 2m	d_{off} = 3m	d_{off} = 4m	d_{off} = 5m	d_{off} = 6m	d_{off} = 7m	d_{off} = 8m
$k = 1$	9.45	7.77	12.47	2.32	12.34	7.20	13.81	13.60
$k = 2$	24.12	22.84	21.08	26.17	14.99	12.10	12.34	23.66
$k = 3$	0.98	5.94	8.28	8.11	10.60	3.46	1.92	
$k = 4$	8.02	12.57		0	8.62	8.45	7.91	
$k = 5$	1.14	1.90		9.43	0.66	8.90	6.62	
$k = 6$	17.36				9.00	9.13	13.56	
$k = 7$						7.42		

Table 43: Cluster delay dispersion values – Torso – $\Phi = 135°$ – env 1

τ_{rms} (ns)	d_{off} = 1m	d_{off} = 2m	d_{off} = 3m	d_{off} = 4m	d_{off} = 5m	d_{off} = 6m	d_{off} = 7m	d_{off} = 8m
$k = 1$	5.62	7.49	13.95	9.83	10.04	10.97	3.67	9.54
$k = 2$	19.15	19.46	15.99	13.93	22.15	10.78	11.60	17.07
$k = 3$	10.52	1.56	5.82	1.45	6.69	2.94	1.06	1.87
$k = 4$	1.70	11.56	10.31	12.02	12.97	10.33	6.93	14.71
$k = 5$	8.61	7.07		11.36		12.80	0.00	
$k = 6$	9.04	4.88		7.70			14.13	
$k = 7$							4.81	
$k = 8$							10.30	

Table 44: Cluster delay dispersion values – Torso – $\Phi = 180°$ – env 1

9.3.3   RX ON SHOULDER

τ_{rms} (ns)	$d_{off}=1m$	$d_{off}=2m$	$d_{off}=3m$	$d_{off}=4m$	$d_{off}=5m$	$d_{off}=6m$	$d_{off}=7m$	$d_{off}=8m$
$k=1$	4.33	2.48	3.03	2.36	3.00	3.01	2.79	2.26
$k=2$	18.71	13.01	20.38	31.57	23.30	24.08	28.95	25.39
$k=3$				13.04	30.58		11.49	24.83
$k=4$				36.80	7.07			
$k=5$					25.74			

Table 45: Cluster delay dispersion values – Shoulder – Φ = 0° – env 1

τ_{rms} (ns)	$d_{off}=1m$	$d_{off}=2m$	$d_{off}=3m$	$d_{off}=4m$	$d_{off}=5m$	$d_{off}=6m$	$d_{off}=7m$	$d_{off}=8m$
$k=1$	1.66	1.69	7.06	2.35	2.59	1.70	2.12	1.44
$k=2$	24.14	21.61	23.44	22.40	19.63	26.21	20.62	23.20
$k=3$	15.67	13.86	10.56	26.12	16.02	18.26	26.48	11.49
$k=4$	11.51	1.03		9.34	7.05	84.87	9.56	21.37
$k=5$	16.04	2.28			8.79			
$k=6$		14.05						

Table 46: Cluster delay dispersion values – Shoulder – Φ = 45° – env 1

τ_{rms} (ns)	$d_{off}=1m$	$d_{off}=2m$	$d_{off}=3m$	$d_{off}=4m$	$d_{off}=5m$	$d_{off}=6m$	$d_{off}=7m$	$d_{off}=8m$
$k=1$	0.00	9.48	9.37	6.64	4.75	4.17	11.42	7.44
$k=2$	21.54	18.97	16.34	13.61	16.06	11.60	12.82	12.59
$k=3$	10.55	7.63	10.59	9.79	9.53	7.18	3.28	6.45
$k=4$	6.88	3.16	11.57	11.26	12.22	0.00	7.09	10.70
$k=5$	9.44	15.74		10.67	6.28	6.97	8.66	5.74
$k=6$	6.71			11.24	9.99	9.37	5.05	5.92
$k=7$	2.65				5.55	2.58		8.59
$k=8$	9.31					3.71		
$k=9$						2.30		

Table 47: Cluster delay dispersion values – Shoulder – Φ = 90° – env 1

τ_{rms} (ns)	$d_{off}=1m$	$d_{off}=2m$	$d_{off}=3m$	$d_{off}=4m$	$d_{off}=5m$	$d_{off}=6m$	$d_{off}=7m$	$d_{off}=8m$
$k=1$	2.37	6.89	4.03	3.96	7.67	9.23	0.91	11.29
$k=2$	17.53	20.83	9.42	15.02	23.98	13.33	17.11	14.83
$k=3$	20.36	14.34	5.93	5.81	15.24	10.36	9.00	6.47
$k=4$	13.89		19.56	9.83		17.73	11.65	13.46
$k=5$	3.26		6.78	10.12			6.65	

				9.04				
$k = 6$				9.04				

Table 48: Cluster delay dispersion values – Shoulder – $\Phi = 135°$ – env 1

τ_{rms} (ns)	$d_{off} = 1m$	$d_{off} = 2m$	$d_{off} = 3m$	$d_{off} = 4m$	$d_{off} = 5m$	$d_{off} = 6m$	$d_{off} = 7m$	$d_{off} = 8m$
$k = 1$	2.55	2.29	1.72	1.81	1.92	1.69	2.44	2.64
$k = 2$	11.48	24.79	19.90	26.29	22.06	29.29	27.05	22.33
$k = 3$		12.70	21.93	11.77	6.09	8.79	12.78	33.03
$k = 4$		13.98	20.50	17.78	24.67	20.32	17.63	
$k = 5$			6.87		10.09			

Table 49: Cluster delay dispersion values – Shoulder – $\Phi = 180°$ – env 1

9.3.4 RX ON BACK

τ_{rms} (ns)	$d_{off} = 1m$	$d_{off} = 2m$	$d_{off} = 3m$	$d_{off} = 4m$	$d_{off} = 5m$	$d_{off} = 6m$	$d_{off} = 7m$	$d_{off} = 8m$
$k = 1$	10.37	9.34	11.64	8.17	6.13	14.93	12.16	5.06
$k = 2$	23.58	22.93	17.36	19.19	8.81	18.72	22.32	9.57
$k = 3$	2.26	17.04	10.24	1.25	1.53	1.72	1.22	0.72
$k = 4$	9.37		1.13	10.23	7.76	10.25		6.34
$k = 5$	7.27			8.91	5.05			6.69
$k = 6$				10.43	4.97			6.66
$k = 7$					5.00			6.35
$k = 8$					5.78			8.31

Table 50: Cluster delay dispersion values – Back – $\Phi = 0°$ – env 1

τ_{rms} (ns)	$d_{off} = 1m$	$d_{off} = 2m$	$d_{off} = 3m$	$d_{off} = 4m$	$d_{off} = 5m$	$d_{off} = 6m$	$d_{off} = 7m$	$d_{off} = 8m$
$k = 1$	4.31	8.95	5.40	12.22	6.53	7.38	10.91	5.00
$k = 2$	26.18	18.71	15.29	15.94	13.25	12.76	14.40	10.33
$k = 3$	12.29	11.99	12.53	14.30	1.29	1.01	2.01	7.90
$k = 4$	18.38	1.52	12.04	4.87	16.44	12.65	14.13	0.77
$k = 5$		11.05		11.40	9.34	8.87	6.17	5.68
$k = 6$		10.73		11.97	10.04	8.51		7.41
$k = 7$					13.87	11.13		7.57
$k = 8$								7.36

Table 51: Cluster delay dispersion values – Back – $\Phi = 45°$ – env 1

τ_{rms} (ns)	$d_{off} = 1m$	$d_{off} = 2m$	$d_{off} = 3m$	$d_{off} = 4m$	$d_{off} = 5m$	$d_{off} = 6m$	$d_{off} = 7m$	$d_{off} = 8m$
$k = 1$	2.08	2.30	1.87	5.94	5.09	5.83	4.83	6.64

$k = 2$	10.68	33.81	21.34	26.45	27.89	10.40	24.47	24.77
$k = 3$	31.39	8.37	6.46	12.46	16.76	12.86	11.57	13.31
$k = 4$	6.12		32.69		8.32	9.83	10.70	
$k = 5$			7.19					

Table 52: Cluster delay dispersion values – Back – Φ = 90° – env 1

τ_{rms} (ns)	d_{off} = 1m	d_{off} = 2m	d_{off} = 3m	d_{off} = 4m	d_{off} = 5m	d_{off} = 6m	d_{off} = 7m	d_{off} = 8m
$k = 1$	2.53	2.95	2.84	6.15	2.62	4.60	1.78	4.67
$k = 2$	17.17	16.77	2.00	34.37	15.37	25.76	23.47	26.94
$k = 3$				9.91	33.31	4.81	35.55	19.43
$k = 4$					6.70		4.46	

Table 53: Cluster delay dispersion values – Back – Φ = 135° – env 1

τ_{rms} (ns)	d_{off} = 1m	d_{off} = 2m	d_{off} = 3m	d_{off} = 4m	d_{off} = 5m	d_{off} = 6m	d_{off} = 7m	d_{off} = 8m
$k = 1$	7.68	4.25	3.82	2.88	2.62	2.62	5.11	3.25
$k = 2$			17.39	11.22	14.43	25.07	29.05	21.94
$k = 3$			18.84	26.89	37.09	12.65	14.38	35.30
$k = 4$				24.77	17.37	11.36		

Table 54: Cluster delay dispersion values – Back – Φ = 180° – env 1

9.4. CENTROID ANGLE-OF-ARRIVAL

9.4.1   ISOLATED ANTENNA

$\bar{\bar{\phi}}_k$ (°)	d_{off} = 1m	d_{off} = 2m	d_{off} = 3m	d_{off} = 4m	d_{off} = 5m	d_{off} = 6m	d_{off} = 7m	d_{off} = 8m
$k = 1$	-3.7	-1.4	-0.2	-1.0	-0.9	3.8	3.0	1.8
$k = 2$	181.2	190.6	172.1	184.0	181.8	180.0	180.8	181.7
$k = 3$		68.4	64.9	322.5	-26.0			16.8
$k = 4$				54.0	47.9			

Table 55 : Centroid AoA – Isolated antenna – env 1

9.4.2   RX ON THE TORSO

$\bar{\bar{\phi}}_k$ (°)	d_{off} = 1m	d_{off} = 2m	d_{off} = 3m	d_{off} = 4m	d_{off} = 5m	d_{off} = 6m	d_{off} = 7m	d_{off} = 8m
$k = 1$	-2.0	-1.0	-0.4	-0.9	-0.7	-0.3	1.2	-0.3
$k = 2$	57.2	52.6	-36.4	25.6	43.4	4.3	3.7	7.2
$k = 3$			48.8	335.1	-5.7	25.9	22.6	331.7

$k = 4$				55.0				21.9

Table 56: Centroid AoA– Torso – Φ = 0° – env 1

$\bar{\bar{\phi}}_k$ (°)	d_{off} $= 1m$	d_{off} $= 2m$	d_{off} $= 3m$	d_{off} $= 4m$	d_{off} $= 5m$	d_{off} $= 6m$	d_{off} $= 7m$	d_{off} $= 8m$
$k = 1$	-5.1	-3.4	-1.8	0.5	0.1	-0.2	0.0	4.3
$k = 2$	81.2	67.1	65.5	46.1	48.0	42.7	41.9	34.8
$k = 3$	73.4	32.6	39.6	54.2	20.4	13.0	12.7	45.3

Table 57: Centroid AoA– Torso – Φ = 45° – env 1

$\bar{\bar{\phi}}_k$ (°)	d_{off} $= 1m$	d_{off} $= 2m$	d_{off} $= 3m$	d_{off} $= 4m$	d_{off} $= 5m$	d_{off} $= 6m$	d_{off} $= 7m$	d_{off} $= 8m$
$k = 1$	-11.0	-4.8	-3.0	37.8	-1.0	-0.9	0.1	0.3
$k = 2$	88.2	79.3	890.1	88.9	71.1	79.8	85.6	78.9
$k = 3$	84.1	64.5	66.9	60.7	107.2	75.2	102.9	132.0
$k = 4$	76.8	86.3		122.2	44.6	44.0	65.2	69.6
$k = 5$		100.9					47.3	55.2

Table 58: Centroid AoA– Torso – Φ = 90° – env 1

$\bar{\bar{\phi}}_k$ (°)	d_{off} $= 1m$	d_{off} $= 2m$	d_{off} $= 3m$	d_{off} $= 4m$	d_{off} $= 5m$	d_{off} $= 6m$	d_{off} $= 7m$	d_{off} $= 8m$
$k = 1$	77.2	64.8	113.1	48.9	91.6	175.1	175.6	164.0
$k = 2$	96.5	162.0	151.3	141.1	162.0	128.7	160.5	162.8
$k = 3$	182.0	183.7	172.3	169.6	174.5	27.0	8.5	
$k = 4$	122.2	88.1		270.0	180.9	120.0	159.5	
$k = 5$	-1.3	-0.9		142.4	1.8	168.6	102.2	
$k = 6$	177.8				142.5	89.5	138.1	
$k = 7$						174.0		

Table 59: Centroid AoA– Torso – Φ = 135° – env 1

$\bar{\bar{\phi}}_k$ (°)	d_{off} $= 1m$	d_{off} $= 2m$	d_{off} $= 3m$	d_{off} $= 4m$	d_{off} $= 5m$	d_{off} $= 6m$	d_{off} $= 7m$	d_{off} $= 8m$
$k = 1$	183.3	177.4	184.0	179.2	185.0	181.0	176.2	179.5
$k = 2$	192.9	180.1	177.0	175.2	180.7	183.9	184.4	179.7
$k = 3$	176.3	-2.6	34.6	-1.4	40.4	-38.4	0.2	5.5
$k = 4$	1.8	178.1	180.3	181.5	179.6	180.2	179.0	181.8
$k = 5$	196.4	192.5		185.5		182.6	114.0	
$k = 6$	163.2	82.1		146.8			-137.6	
$k = 7$							181.5	
$k = 8$							183.7	

Table 60: Centroid AoA– Torso – Φ = 180° – env 1

9.4.3   Rx on the Shoulder

$\bar{\bar{\phi}}_k$ (°)	d_{off} = 1m	d_{off} = 2m	d_{off} = 3m	d_{off} = 4m	d_{off} = 5m	d_{off} = 6m	d_{off} = 7m	d_{off} = 8m
$k = 1$	351.1	-4.1	-2.3	-3.2	-1.2	-0.7	-0.9	-2.5
$k = 2$	76.2	67.9	62.2	123.5	79.3	61.6	76.1	77.3
$k = 3$				59.0	32.6		37.8	33.2
$k = 4$				41.0	47.9			
$k = 5$					136.4			

Table 61: Centroid AoA– Shoulder – Φ = 0° – env 1

$\bar{\bar{\phi}}_k$ (°)	d_{off} = 1m	d_{off} = 2m	d_{off} = 3m	d_{off} = 4m	d_{off} = 5m	d_{off} = 6m	d_{off} = 7m	d_{off} = 8m
$k = 1$	-8.2	67.0	16.8	-1.8	-1.2	-0.9	0.4	-0.5
$k = 2$	89.0	167.9	164.3	167.7	166.5	145.8	175.3	162.0
$k = 3$	74.0	79.5	128.3	140.5	120.5	160.7	76.0	164.5
$k = 4$	143.7	178.5		79.2	48.6	64.3	161.7	64.7
$k = 5$	166.7	-1.7			170.9			
$k = 6$		142.7						

Table 62: Centroid AoA– Shoulder – Φ = 45° – env 1

$\bar{\bar{\phi}}_k$ (°)	d_{off} = 1m	d_{off} = 2m	d_{off} = 3m	d_{off} = 4m	d_{off} = 5m	d_{off} = 6m	d_{off} = 7m	d_{off} = 8m
$k = 1$	285.0	183.6	39.9	37.8	34.3	71.6	178.2	175.1
$k = 2$	180.3	181.4	174.2	170.1	176.2	177.1	176.7	181.7
$k = 3$	94.8	88.8	176.9	183.1	179.8	180.7	18.2	18.3
$k = 4$	184.2	17.1	181.5	173.0	189.2	210.0	187.1	149.7
$k = 5$	171.9	181.8		195.1	126.7	162.4	186.5	198.6
$k = 6$	86.0			119.8	181.7	179.5	72.4	206.9
$k = 7$	354.3				135.0	5.6		186.0
$k = 8$	189.3					179.3		
$k = 9$						183.8		

Table 63: Centroid AoA– Shoulder – Φ = 90° – env 1

$\bar{\bar{\phi}}_k$ (°)	d_{off} = 1m	d_{off} = 2m	d_{off} = 3m	d_{off} = 4m	d_{off} = 5m	d_{off} = 6m	d_{off} = 7m	d_{off} = 8m
$k = 1$	3.8	-19.7	-4.9	-8.2	-43.8	-16.9	0.9	192.0
$k = 2$	188.3	187.2	181.8	193.8	194.9	190.1	189.0	195.3
$k = 3$	198.7	-143.7	205.9	180.6	198.7	190.4	194.1	-12.2
$k = 4$	-86.9		201.4	191.2		190.9	291.1	191.9
$k = 5$	283.7		200.9	260.4				

	$d_{off}=1m$	$d_{off}=2m$	$d_{off}=3m$	$d_{off}=4m$	$d_{off}=5m$	$d_{off}=6m$	$d_{off}=7m$	$d_{off}=8m$
$k=6$				217.9				

Table 64: Centroid AoA– Shoulder – $\Phi = 135°$ – env 1

$\bar{\bar{\phi}}_k$ (°)	$d_{off}=1m$	$d_{off}=2m$	$d_{off}=3m$	$d_{off}=4m$	$d_{off}=5m$	$d_{off}=6m$	$d_{off}=7m$	$d_{off}=8m$
$k=1$	5.0	3.0	2.6	2.0	0.5	1.2	-1.6	-2.5
$k=2$	281.9	205.3	185.2	195.6	185.8	-84.5	284.8	-55.2
$k=3$		310.1	286.7	322.1	315.7	309.0	-66.2	194.4
$k=4$		292.0	216.4	269.5	-89.4	185.0	193.8	
$k=5$			309.2		-85.2			

Table 65: Centroid AoA– Shoulder – $\Phi = 180°$ – env 1

9.4.4 Rx on the Back

$\bar{\bar{\phi}}_k$ (°)	$d_{off}=1m$	$d_{off}=2m$	$d_{off}=3m$	$d_{off}=4m$	$d_{off}=5m$	$d_{off}=6m$	$d_{off}=7m$	$d_{off}=8m$
$k=1$	173.0	182.9	174.1	179.2	177.8	179.3	178.6	178.8
$k=2$	180.8	186.0	181.9	174.5	177.1	184.6	178.9	180.7
$k=3$	-0.9	185.3	178.7	356.1	0.8	-1.6	-1.1	-0.3
$k=4$	175.0		0.3	140.1	182.2	182.1		193.9
$k=5$	186.9			183.2	177.5			181.4
$k=6$				185.7	184.7			169.3
$k=7$					192.0			196.6
$k=8$					183.4			183.2

Table 66: Centroid AoA– Back – $\Phi = 0°$ – env 1

$\bar{\bar{\phi}}_k$ (°)	$d_{off}=1m$	$d_{off}=2m$	$d_{off}=3m$	$d_{off}=4m$	$d_{off}=5m$	$d_{off}=6m$	$d_{off}=7m$	$d_{off}=8m$
$k=1$	-74.4	-89.1	-51.7	-123.1	182.6	184.9	192.3	186.6
$k=2$	193.8	195.8	211.7	208.3	194.4	193.2	189.9	186.7
$k=3$	203.5	198.3	205.7	-121.2	357.3	2.1	-7.9	-50.3
$k=4$	-96.7	1.6	192.0	-33.1	-115.2	260.3	197.8	289.5
$k=5$		190.6		190.1	196.4	269.5	275.6	191.2
$k=6$		195.9		-172.8.	-83.1	187.9		212.2
$k=7$					187.7	193.8		224.9
$k=8$								195.6

Table 67: Centroid AoA– Back – $\Phi = 45°$ – env 1

$\bar{\bar{\phi}}_k$ (°)	$d_{off}=1m$	$d_{off}=2m$	$d_{off}=3m$	$d_{off}=4m$	$d_{off}=5m$	$d_{off}=6m$	$d_{off}=7m$	$d_{off}=8m$

$k = 1$	3.4	1.3	0.3	-27.1	-22.1	-10.1	-21.2	-27.5
$k = 2$	276.1	275.1	-127.8	258.7	270.5	271.6	-74.0	282.1
$k = 3$	-80.4	-66.3	250.3	283.2	245.4	286.3	-66.4	274.6
$k = 4$	287.8		-62.5		290.5	262.3	225.9	
$k = 5$			-55.3					

Table 68: Centroid AoA– Back – Φ = 90° – env 1

$\bar{\bar{\phi}}_k$ (°)	d_{off} = 1m	d_{off} = 2m	d_{off} = 3m	d_{off} = 4m	d_{off} = 5m	d_{off} = 6m	d_{off} = 7m	d_{off} = 8m
$k = 1$	-0.1	0.0	0.4	0.4	-0.1	0.7	0.5	-2.1
$k = 2$	287.5	-62.4	-50.0	-36.4	293.0	-53.4	-56.2	-19.8
$k = 3$				310.6	-20.3	320.7	-10.9	-48.9
$k = 4$					317.3		-33.0	

Table 69: Centroid AoA– Back – Φ = 135° – env 1

$\bar{\bar{\phi}}_k$ (°)	d_{off} = 1m	d_{off} = 2m	d_{off} = 3m	d_{off} = 4m	d_{off} = 5m	d_{off} = 6m	d_{off} = 7m	d_{off} = 8m
$k = 1$	-2.8	-1.3	-1.0	-0.8	-1.3	0.1	1.8	-0.4
$k = 2$			-37.7	50.8	9.6	6.4	5.4	-20.6
$k = 3$			39.3	21.5	-10.3	325.3	329.6	24.0
$k = 4$				339.8	43.0	30.1		

Table 70: Centroid AoA– Back – Φ = 180° – env 1

9.5. CLUSTER ANGULAR SPREAD

9.5.1 ISOLATED ANTENNA

ϕ_{rms} (°)	d_{off} = 1m	d_{off} = 2m	d_{off} = 3m	d_{off} = 4m	d_{off} = 5m	d_{off} = 6m	d_{off} = 7m	d_{off} = 8m
$k = 1$	7.6	0.6	3.1	1.1	1.6	14.5	9.0	5.1
$k = 2$	50.6	14.4	16.5	11.8	15.8	7.0	19.9	7.6
$k = 3$		10.8	4.6	10.1	15.1			16.9
$k = 4$		6.1		6.4	10.7			

Table 71: Cluster angular dispersion values – Isolated antenna – env 1

9.5.2 RX ON TORSO

ϕ_{rms} (°)	d_{off} = 1m	d_{off} = 2m	d_{off} = 3m	d_{off} = 4m	d_{off} = 5m	d_{off} = 6m	d_{off} = 7m	d_{off} = 8m
$k = 1$	2.4	0.8	1.3	0.5	2.2	4.6	2.8	0.8
$k = 2$	15.0	11.8	5.8	7.3	6.9	15.9	17.9	14.3
$k = 3$			8.5	7.5	14.3	12.3	15.5	11.6

$k = 4$			3.5				6.6

Table 72: Cluster angular dispersion values – Torso – Φ = 0° – env 1

ϕ_{rms} (°)	d_{off} = 1m	d_{off} = 2m	d_{off} = 3m	d_{off} = 4m	d_{off} = 5m	d_{off} = 6m	d_{off} = 7m	d_{off} = 8m
$k = 1$	1.1	1.6	1.3	5.2	1.9	2.1	0.7	10.2
$k = 2$	7.0	6.1	4.9	17.5	6.0	21.6	13.8	26.7
$k = 3$	7.3	3.5	6.8	8.5	12.0	11.4	11.2	17.2

Table 73: Cluster angular dispersion values – Torso – Φ = 45° – env 1

ϕ_{rms} (°)	d_{off} = 1m	d_{off} = 2m	d_{off} = 3m	d_{off} = 4m	d_{off} = 5m	d_{off} = 6m	d_{off} = 7m	d_{off} = 8m
$k = 1$	4.8	0.4	1.0	22.9	0.9	1.0	1.9	3.8
$k = 2$	13.6	3.0	20.0	22.4	24.0	21.1	21.6	20.3
$k = 3$	14.4	11.0	8.7	8.2	19.6	6.8	17.0	7.1
$k = 4$	14.4	10.0		15.8	6.2	13.1	5.0	8.3
$k = 5$							11.9	15.7

Table 74: Cluster angular dispersion values – Torso – Φ = 90° – env 1

ϕ_{rms} (°)	d_{off} = 1m	d_{off} = 2m	d_{off} = 3m	d_{off} = 4m	d_{off} = 5m	d_{off} = 6m	d_{off} = 7m	d_{off} = 8m
$k = 1$	11.1	5.8	49.8	11.4	19.9	10.3	8.8	42.9
$k = 2$	11.1	15.7	21.6	21.6	24.6	33.3	27.5	24.0
$k = 3$	0.1	3.3	11.6	16.1	9.4	19.1	16.2	
$k = 4$	8.8	8.8		0.0	3.3	16.4	16.2	
$k = 5$	1.5	1.7		26.3	0.8	17.1	18.3	
$k = 6$	8.5				28.8	22.2	25.5	
$k = 7$						5.9		

Table 75: Cluster angular dispersion values – Torso – Φ = 135° – env 1

ϕ_{rms} (°)	d_{off} = 1m	d_{off} = 2m	d_{off} = 3m	d_{off} = 4m	d_{off} = 5m	d_{off} = 6m	d_{off} = 7m	d_{off} = 8m
$k = 1$	5.2	12.0	14.0	9.7	10.0	18.8	3.7	10.5
$k = 2$	6.3	7.6	14.2	11.9	7.9	15.6	18.0	15.5
$k = 3$	7.5	1.0	40.4	0.9	51.5	36.7	0.6	3.7
$k = 4$	0.7	7.9	19.5	7.7	8.4	12.5	10.3	14.1
$k = 5$	6.9	13.2		13.1		11.8	0.0	
$k = 6$	20.9	15.9		12.2			4.1	
$k = 7$							2.7	
$k = 8$							10.5	

Table 76: Cluster angular dispersion values – Torso – Φ = 180° – env 1

9.5.3   RX ON SHOULDER

ϕ_{rms} (°)	d_{off} = 1m	d_{off} = 2m	d_{off} = 3m	d_{off} = 4m	d_{off} = 5m	d_{off} = 6m	d_{off} = 7m	d_{off} = 8m
$k = 1$	2.2	1.0	3.3	3.5	1.6	3.8	1.0	4.1
$k = 2$	10.9	7.4	11.5	21.8	12.4	15.0	22.8	21.9
$k = 3$				5.6	14.4		6.3	12.0
$k = 4$				10.3	4.0			
$k = 5$					22.1			

Table 77: Cluster angular dispersion values – Shoulder – Φ = 0° – env 1

ϕ_{rms} (°)	d_{off} = 1m	d_{off} = 2m	d_{off} = 3m	d_{off} = 4m	d_{off} = 5m	d_{off} = 6m	d_{off} = 7m	d_{off} = 8m
$k = 1$	0.9	3.0	28.4	1.6	2.0	1.1	3.0	3.2
$k = 2$	8.8	12.5	23.1	16.4	27.0	29.6	13.7	21.9
$k = 3$	13.7	6.2	46.7	28.7	16.3	22.7	19.7	17.2
$k = 4$	30.2	0.9		29.5	16.9	17.3	10.9	15.4
$k = 5$	11.6	2.2			7.2			
$k = 6$		5.6						

Table 78: Cluster angular dispersion values – Shoulder – Φ = 45° – env 1

ϕ_{rms} (°)	d_{off} = 1m	d_{off} = 2m	d_{off} = 3m	d_{off} = 4m	d_{off} = 5m	d_{off} = 6m	d_{off} = 7m	d_{off} = 8m
$k = 1$	0.0	3.7	31.5	24.6	22.2	19.4	7.5	9.1
$k = 2$	7.6	10.7	26.0	24.0	7.1	8.9	14.2	13.2
$k = 3$	18.6	11.8	18.8	10.0	8.4	7.9	16.8	19.4
$k = 4$	8.8	30.5	25.5	23.4	15.6	0.0	12.6	6.3
$k = 5$	14.5	16.4		17.2	5.2	14.3	9.7	10.2
$k = 6$	27.8			10.8	5.5	6.3	21.9	8.9
$k = 7$	0.6				20.7	13.1		12.5
$k = 8$	11.4					3.7		
$k = 9$						8.1		

Table 79: Cluster angular dispersion values – Shoulder – Φ = 90° – env 1

ϕ_{rms} (°)	d_{off} = 1m	d_{off} = 2m	d_{off} = 3m	d_{off} = 4m	d_{off} = 5m	d_{off} = 6m	d_{off} = 7m	d_{off} = 8m
$k = 1$	0.4	33.3	17.2	19.2	39.3	29.9	1.7	18.9
$k = 2$	8.4	11.7	15.3	21.6	31.7	9.3	14.8	21.0
$k = 3$	17.9	26.4	11.6	13.6	28.7	12.0	17.4	21.8
$k = 4$	6.6		26.5	10.8		17.3	16.0	16.0
$k = 5$	4.3		32.5	20.7			15.5	
$k = 6$				15.8				

Table 80: Cluster angular dispersion values – Shoulder – Φ = 135° – env 1

ϕ_{rms} (°)	d_{off} = 1m	d_{off} = 2m	d_{off} = 3m	d_{off} = 4m	d_{off} = 5m	d_{off} = 6m	d_{off} = 7m	d_{off} = 8m
$k = 1$	0.4	0.1	0.6	0.6	1.0	1.8	9.1	8.3
$k = 2$	8.9	15.4	8.5	23.3	4.4	11.7	14.2	10.2
$k = 3$		4.7	9.4	8.6	9.7	13.5	8.9	19.7
$k = 4$		4.3	12.7	23.2	30.0	7.3	13.1	
$k = 5$			11.1		11.4			

Table 81: Cluster angular dispersion values – Shoulder – Φ = 180° – env 1

9.5.4   RX ON BACK

ϕ_{rms} (°)	d_{off} = 1m	d_{off} = 2m	d_{off} = 3m	d_{off} = 4m	d_{off} = 5m	d_{off} = 6m	d_{off} = 7m	d_{off} = 8m
$k = 1$	15.0	28.5	24.7	8.8	6.7	12.3	10.6	3.4
$k = 2$	8.2	29.1	10.1	16.4	13.1	18.0	22.0	12.8
$k = 3$	1.2	11.6	13.5	0.7	1.9	4.4	0.6	0.5
$k = 4$	5.4		0.7	5.3	8.8	7.9		7.8
$k = 5$	19.1			8.5	10.9			5.8
$k = 6$				12.9	4.4			13.9
$k = 7$					13.9			6.9
$k = 8$					10.4			8.3

Table 82: Cluster angular dispersion values – Back – Φ = 0° – env 1

ϕ_{rms} (°)	d_{off} = 1m	d_{off} = 2m	d_{off} = 3m	d_{off} = 4m	d_{off} = 5m	d_{off} = 6m	d_{off} = 7m	d_{off} = 8m
$k = 1$	13.5	22.8	36.5	26.4	7.2	13.3	13.8	10.6
$k = 2$	14.2	15.1	29.3	28.3	11.4	9.1	10.6	7.0
$k = 3$	13.3	16.5	18.1	17.0	1.5	1.4	14.9	25.3
$k = 4$	15.1	3.3	14.8	26.4	9.3	12.1	14.7	5.4
$k = 5$		10.7		10.4	14.2	16.7	25.3	11.5
$k = 6$		20.6		4.2	20.1	12.6		25.9
$k = 7$					9.0	15.0		9.2
$k = 8$								9.2

Table 83: Cluster angular dispersion values – Back – Φ = 45° – env 1

ϕ_{rms} (°)	d_{off} = 1m	d_{off} = 2m	d_{off} = 3m	d_{off} = 4m	d_{off} = 5m	d_{off} = 6m	d_{off} = 7m	d_{off} = 8m
$k = 1$	1.3	1.4	1.2	20.6	20.3	17.4	17.8	18.1
$k = 2$	6.3	28.1	13.4	21.3	25.4	28.3	13.5	25.6
$k = 3$	12.3	9.2	19.9	21.9	17.8	14.6	10.4	32.2

$k = 4$	6.8		11.1		12.8	33.7	20.3	
$k = 5$			8.1					

Table 84: Cluster angular dispersion values – Back – Φ = 90° – env 1

ϕ_{rms} (°)	d_{off} $= 1m$	d_{off} $= 2m$	d_{off} $= 3m$	d_{off} $= 4m$	d_{off} $= 5m$	d_{off} $= 6m$	d_{off} $= 7m$	d_{off} $= 8m$
$k = 1$	0.5	0.6	0.5	1.8	0.6	2.3	0.5	5.9
$k = 2$	8.1	11.7	8.8	18.4	5.9	19.1	7.8	19.5
$k = 3$				9.3	13.5	5.2	7.9	12.5
$k = 4$				7.2		6.3		

Table 85: Cluster angular dispersion values – Back – Φ = 135° – env 1

ϕ_{rms} (°)	d_{off} $= 1m$	d_{off} $= 2m$	d_{off} $= 3m$	d_{off} $= 4m$	d_{off} $= 5m$	d_{off} $= 6m$	d_{off} $= 7m$	d_{off} $= 8m$
$k = 1$	2.8	4.8	1.2	0.8	3.4	0.6	4.0	1.3
$k = 2$			3.9	2.9	4.7	19.3	12.9	6.1
$k = 3$			11.3	4.8	13.5	9.6	7.2	10.4
$k = 4$				6.6	5.0	7.3		

Table 86: Cluster angular dispersion values – Back – Φ = 180° – env 1